2013-09-13

Nanopore Structure Analysis of Geological and Catalytic Materials

Aquino Carvelli, Samuel David

UNIVERSITY OF CALGARY

Nanopore Structure Analysis of Geological and Catalytic Materials

by

Samuel David Aquino Carvelli

A THESIS

SUBMITTED TO THE FACULTY OF GRADUATE STUDIES

IN PARTIAL FULFILMENT OF THE REQUIREMENTS FOR THE

DEGREE OF MASTER OF SCIENCE

DEPARTMENT OF GEOSCIENCE

CALGARY, ALBERTA

SEPTEMBER, 2013

Abstract

The study of nanoporous materials is important due to their many applications, including gas sorption/storage and catalysis. In this thesis, two classes of materials have been studied: a hydrocracking catalyst (nickel (Ni)-containing zeolite, Ni/H-ZSM), prepared using two different methods, and naturally-occurring tight gas/shale core plugs from several North American reservoirs. The Ni/H-ZSM catalyst was used for the hydrocracking of toluene, while the tight gas/shale samples are from reservoirs with enormous potential for natural gas production. Because the storage and flow properties of both of these materials relate primarily to pores at the nanometer scale, these topics are connected through the multiplicity of powerful characterization techniques that have been employed, including high resolution imaging, gas sorption, and computational methods (e.g., DFT). It has been found that the two methods of Ni incorporation of the Ni/H-ZSM samples, which are catalytically similar, differ in the Ni nanoparticle size and distribution within the pores. For the tight-gas/shale reservoir samples, characteristic pore shapes and distributions have been identified, and comparisons between routine and non-routine characterizing methods were performed. Elemental compositions with depth in powdered samples were explored and their implications for distribution of organic and inorganic matter explored.

Acknowledgements

I would first like to gratefully acknowledge Drs. Viola Birss and Christopher Clarkson for their very valuable guidance and assistance at all stages of my thesis project, for the many useful discussions, and overall, for giving me the opportunity to work with and learn from them and their research groups. I would also like to express my sincere gratitude to Dr. Hebert Molero for his help during the development of this thesis, Dr. Gerardo Vitale for helping me with the preparation and characterization of the catalysts, Dr. Josefina Perez Scott, for sharing her knowledge in catalysis, and Dr. Pedro Pereira for his support and the use of some of his facilities. As well, I am very grateful for the financial support that I received from the Natural Sciences and Engineering Research Council of Canada (NSERC) and Nova Chemicals, the samples received from Encana for this research, and for the facilities and technical assistance that I had access to in the Departments of Chemistry, Geosciences, and Chemical and Petroleum Engineering, as well as the Microscopy and Imaging Facility. This includes the Department of Chemistry glassblowing shop and both Chemical and Engineering Stores. Thanks are also extended to Cathy Hubble, the Administrative Assistant in the Department of Geosciences, for her help in many ways.

Special thanks also to everyone who helped with important discussions on my research, supported me in difficulties, and others who made this experience so enjoyable. This includes Dr. Dustin Banham, Dr. Hany El-Sayed, Dr. Scott Paulson, Dr. Carlos Scott, Dr. Felicia Feng, Diane Lespinasse, Nisael Solano, Lisa DeLeebeeck, Eumir Hernandez, Oscar Contreras, and Miriam Fort. Included are also other members of the groups of Dr Viola Birss, Dr Christopher Clarkson, and Dr Pedro Pereira, who always were willing to help with the small issues.

Finally, I would like to thank those who, even though they were not physically nearby, encouraged me just by believing in me. This includes my mom and dad (Maria and Ricardo), my sister (Rimarsa), two of my friends for life (Eleazar and Luis Alfredo), and other close family and friends.

Dedication

To all my family and friends.

Table of Contents

List of Tables

List of Figures and Illustrations

List of Symbols, Abbreviations and Nomenclature

Symbol	Definition
°C	Degrees Celsius
µm	Micrometer
Å	Angstrom
a.u.	Adimensional units (dimensionless)
ads	Adsorption
AES	Auger Electron Spectroscopy
Ar	Argon
BET	Brunauer–Emmett–Teller method
BJH	Barrett-Joyner-Halenda method
BSE	Back-Scattered Electron Microscopy
BTX	Benzene, Toluene, and the three Xylene isomers
C	Carbon
C-C	Carbon-Carbon single bonded
C-OH	Carbon bounded to an OH
C=O	Carbon bounded to Oxygen
C2	Ethane
C4	Butane
cc/min	Cubic centimeter
cm^{-1}	Inverse of centimeter
$cm^3/gÅ$	Cubic centimeter per unit of mass (gram) per unit of length (Å)
CO_2	Carbon dioxide
CO_3	Carbonate
Cu	Cupper
D-A	Dubinin-Astakhov
D-R	Dubinin-Radushkevich
des	Desorption
deg	Angular degrees
deg/min	Angular degrees per unit of time (minutes)
DFT	Density Functional Theory
DRIFTS	Diffuse Reflectance Infra-red Fourier Transform Spectroscopy
EDS	Energy-dispersive X-ray spectroscopy
eV	Unit of energy, electron-volts
FCC	Fluid Catalytic Cracking
h	Hour
H-ZSM-5	Acid form of zeolite ZSM-5
H_2	Hydrogen
H_2O	Water
K	Unit of temperature, Kelvin
Kr	Krypton

m^2/g	Square meters per unit of mass (gram)
m^2/g cat	Square meters per unit of mass of catalyst (gram)
md	Milidarcy
min	Minute
MPa	Megapascal
N_2	Nitrogen
nd	Nanodarcy
Ni	Nickel
Ni/H-ZSM-5	Nickel supported on acid zeolite ZSM-5
NiO	Nickel oxide
nm	Nanometer
nm/min	Nanometer per unit of time (minute)
O-C=O	Carbon bounded to two oxygen atoms
P	Pressure
P/P^0	Partial pressure
Pd	Palladium
Pd/H-ZSM-5	Palladium supported on acid zeolite ZSM-5
pygas	Pyrolysis gasoline
SANS/USANS	Small-angle neutron scattering/ Ultra Small Angle Neutron Scattering
sccm	Standard Cubic Centimeters per unit of time (Minute)
SEM	Scanning Electron Microscopy
Shale B	Barnett Shale
Shale D	Duvernay Shale
Shale H	Haynesville Shale
Shale M	Marcellus Shale
Shale P	Muskwa-Cordova Shale
Shale R	Milk River Shale
Shale U	Muskwa Shale
Shale W	Woodford Shale
Si-(OH)-Al	Bronsted acid site on the zeolite H-ZSM-5
SS	Solid State
SSX	Solid State, H-ZSM-5 zeolite having X wt. % of Ni
SX	Tight gas sample, X is the number of the sample. X = 1, 2, 3 … 10
TCD	Thermal conductivity detector
TEM	Transmission Electron Microscopy
Tcf	Trillion cubic feet
Torr	Unit of pressure (1 Torr = 133.322368 Pa)
TPR	Thermal Programmed Reduction
V_m	Volume of gas adsorbed
Watt	Unit of power (1 watt = 1 J/s)
WI	Incipient wetness impregnation
WIX	Incipient wetness impregnation, H-ZSM-5 zeolite

	having X wt. % of Ni
WSHV	Weight hourly space velocity, mass flow
XPS	X-ray Photo-electron Spectroscopy
XRD	X-ray Diffraction
ZSM-5	Zeolite type ZSM-5, (Zeolite Socony Mobil – 5)

Chapter One: **Introduction**

1.1 Ni-containing H-ZSM-5 (zeolite) catalysts

In the literature, the incorporation of Ni on support materials, such as silica, alumina or zeolites, is well known for the preparation of catalysts, and zeolite-supported Ni has been used in a range of catalytic reactions, including hydrogenation, isomerization, oxidation, and hydrocracking (Badrinarayanan et al., 1981; Arcoya et al., 1990; Kumar et al., 1997; Masalska, 2005; Yuan et al., 2006; Lee et al., 2007; Vosmerikov et al., 2009; Molero et al. 2009; Vitale et al., 2013). However, the activity, selectivity, and stability of these supported Ni catalysts depend on the method of Ni incorporation used (Vitale et al., 2013). To better understand the effect of the preparation parameters on the catalyst properties, the dispersion, distribution, and states of the metal or metal oxide must therefore be determined.

1.1.1 Zeolites

Zeolites are known to naturally occur in nature in the form of faujasite, mordenite, and offretite and today are often used as catalysts. Even so, the use of naturally occurring zeolites in catalysis is limited, since they contain impurities that vary from one deposit to another, and thus they do not have controlled catalytic properties. Therefore, a synthetic form of faujasite was used for the first time in a refinery for the fluid catalytic cracking of heavy oil in the middle of the 20th century, resulting in several billion dollars of revenue per year to the refinery industry (Weitkamp, 2000; Naber et al., 1979).

Smith (1963) defined a zeolite as an alumino-silicate material, having a structure with cavities occupied by ions and water molecules, both of which have good mobility, allowing ion

exchange and reversible dehydration. The formula that represents the zeolite chemical composition is presented in the following equation:

$$A_{y/m}^{m+}\left[(SiO_2)_x \cdot (AlO_2^-)_y\right] \cdot nH_2O \quad (1.1)$$

where A is the cation with a charge m, (x+y) is the number of octahedra per unit cell, and x:y is the silicon:aluminum atomic ratio (Weitkamp, 2000).

The historical development of zeolites is based on their physico-chemical properties, namely adsorption, ion exchange, reactivity, and catalysis. While there have been many studies of zeolites and their applications, several of these are highlighted here. For example, waste water purification by using the NaP1 zeolite was studied by Alvarez-Ayuzo et al. (2003). They found that the synthetic zeolite NaP1, which is similar to clinoptilolite, showed preferential sorption of contaminant metals, such as Cr, Ni, Zn, Cu, and Cd. These contaminants, produced by various industrial sectors, sorbed ten times more in the synthetic form than did the natural zeolite, with the process being pH dependent.

Synthetic zeolites are widely used in the petrochemical industry as catalysts. For instance, Zeolite Y has been employed for decades in fluid catalytic cracking (FCC) (Giannetto et al. 2000). Scherzer (1991), in a very extended study, designed FCC catalysts based on zeolite Y and also considered feedstock type, reactor design, process conditions, product demand, environmental factors, and cost effectiveness. The zeolite performance was related to zeolite properties, including the silicon content, the matrix, and the manufacturing process.

Gasoline upgrading with ethanol has been carried out using a modified beta-zeolite (Kiatkittipong et al., 2011). Beta-zeolite was originally described by Mobil Oil Co. in its patent (Wadlinger et al., 1967); however, Kiarkittipong et al. modified the zeolite using ion exchange of

Co and Mg. While a lower surface area resulted, a higher ethanol conversion (> 25 – 30%) was achieved than when only beta zeolite was used.

Tukur et al. (2011) compared the isomerization and disproportionation of m-xylene using four zeolites, including ZSM-5, mordenite, SSZ-33, and TNU-9. From the catalytic reaction, three important factors were determined. The focus of this research was to obtain the best catalysts based on the following four parameters: the overall conversion, the p-xyline:o-xylene ratio (P:O), the isomerization:disproportionation ratio (I:D), and the apparent reaction activation energy (EAA). Tukur et al. found that the sequence of extent of conversion, from best to worst, was SSZ-33 > TNU-9 > mordenite > ZSM-5, for the P:O and I:D ratios, the sequence was ZSM-5 > TNU-9 > SSZ-33 > mordenite; and for the EAA values, the order was ZSM-5 > TNU-9 > mordenite > SSZ-33.

The detergent industry also uses Na-A zeolites in the preparation with ecologic purposes (zeolite Na-A has a silicon:aluminium ratio of 1 and therefore, its activity to ion exchange is extremely high). In fine chemistry (the generic technical term for the synthesis of intermediaries and fine products for pharmaceutical purposes), zeolites are also employed, including molecular sieves based on phosphates (AlPO4-, SAPO-, MeAPO, MeSAPO) (Giannetto et al., 2000). These molecular sieves have frameworks based on Al and P, and are also called zeotypes because they contain elements other than Si and Al (Martin-Lugueno et al., 1995).

Also, zeolites offer numerous advantages to catalytic reactions compared to liquid catalysts, including the fact that corrosion of metallic containers does not occur, there are no waste or disposal problems, high thermo-stability, and it is also quite straightforward to carry out a continuous process (fix bed reactors), etc. (Perot et al., 1990).

In this thesis, the catalysts studied were prepared by using a synthetic zeolite, Type ZSM-5. This zeolite is built from a pentasil unit having a high silicon:aluminum ratio, between 15 and infinity (Figure 1.1) (Weitkamp, 2000; Gianetto et al. 2000). For the zeolite used here, the silicon:aluminum ratio was determined to be 20 (Molero et al., 2009). The ZSM-5 zeolite contains a characteristic intercepting system of ten-membered ring pore, one straight and other sinusoidal. Therefore, this zeolite has gained importance for heterogeneous catalytic reactions in the petrochemical industry for several reactions, such as the synthesis of ethylbenzene, the isomerization of xylenes, and the disproportionation of toluene (Weitkamp, 2000).

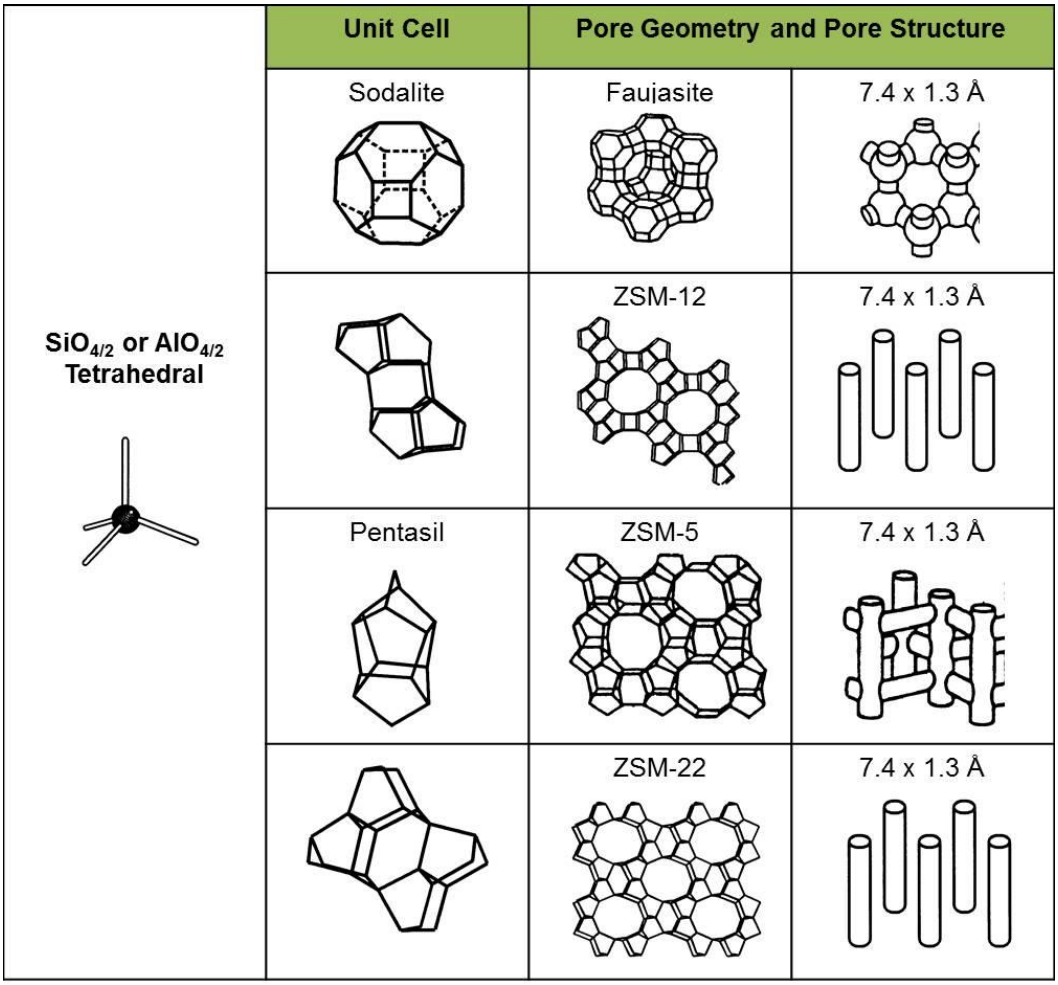

Figure 1.1 Structure of four selected zeolites, from top to bottom: Faujasite or zeolite X, Y; ZSM-12, ZSM-5, and ZSM-22; numbers in the last column represent the dimensions of the pores (Adapted from Weitkamp, 2000).

1.1.2 Metal-zeolite catalysts

1.1.2.1 Reactions and materials investigated

Ni, dispersed on ZSM-5 zeolite surfaces, has been used for several decades to catalyze numerous reactions of hydrocarbons (Section 1.1.1.1). However, these catalysts have not yet been examined for the hydrocracking of a probe molecule, such as toluene, to generate short paraffins,

other than as part of our own work (Molero et al., 2009). However, there is some related literature available, focussed on the catalysis of other types of reactions.

For example, low Ni loadings (0.1 wt. %), introduced on H-ZSM-5 using the solid state ion exchange (SS) process, have been examined by Balkrishnan et al. (1982) for the conversion of methanol to light olefins (ethylene, propylene, and butenes), giving a comparison with other additives, such as P, B, and Mo. Balkrishnan extended the work from earlier efforts, where only P was used for the same reaction (Vedrine et al. (1982). Balkrishnan et al. (1982) showed that the best performance in terms of conversion, besides the H-ZSM-5 itself, i.e., 100 %, was demonstrated by catalysts containing P, giving a 98% conversion, followed by Ni (77 %) and B (64 %). However, the best selectivity towards small hydrocarbons was obtained with the catalyst containing Ni, followed by the catalyst containing B, then P, and finally the support alone. Although a mechanism for this catalytic reaction was not offered, they suggested that the high performance was due to the crystallinity of the catalysts and their good acid properties, as determined by XRD and TPD in NH_3, respectively.

Hoang et al. (1994) studied the effect of pH during the synthesis of Ni/H-ZSM-5 catalysts, tested in the conversion of n-hexane. Hoang D. L. et al. (1994) claimed that there were several studies on Ni/H-ZSM-5 at that time (two decades ago) (Sung D. et al., 1991; Arcoya A. et al., 1990; Wichterlova B. et al., 1989; and Satyanarayana C. V. V. et al., 1990). However, these studies did not involve a full characterization of the Ni-based catalysts. The methodology employed by Hoang et al (1994) was wet impregnation of 0.5 or 2.0 wt. % Ni nitrate at pH 4.8 or pH 1.8. Finally, it was concluded from the use of various experimental techniques (CO-IR spectroscopy, TPD-Ammonia, and H_2 chemisorption) that there were significant variances among the catalysts. The two main conclusions were that it was not easy to reduce the Ni^{2+}

species at temperatures below 800 C when a low Ni content and low pH were employed, as the Ni ions then strongly interact with the support, and secondly, that Ni is formed in large clusters at the outer surface of the support when large amounts of Ni and a higher pH was used.

Lugstein A et al. (1999) studied the hydroisomerization and cracking of n-octane and C_8 isomers, using Ni-containing zeolites (ZSM-5, beta zeolite, and mordenite). They used a high Ni content (> 8 wt. %) catalyst as an alternative to Pt, since Pt was claimed by Paal Z. (1988) to be able to catalyze the cracking of all types of hydrocarbons. Ni was incorporated by dissolving $NiCl_2$ in an ammonia solution, as reported by Sauvage E. et al. (1995), by using the wet impregnation technique. Lugstein A. et al. concluded that Ni/H-ZSM-5 was the best catalyst for this reaction, not only in terms of conversion but also due to its selectivity towards smaller molecules ($C_3 – C_5$). One of the main advantages of using the Ni/H-ZSM-5 catalysts over those involving alternative zeolitic supports (e.g., beta zeolite and mordenite) is the pore size of ZSM-5 (5.6 Å), compared to the kinetic diameter of n-octane (4.3 Å) and its high adsorption capacity.

More recently, Gonzalez H. et al. (2004) studied the activity and selectivity of various metals (Ni, Mo, and Pt), supported on H-ZSM-5-Al_2O_3, for the hydroconversion of hydrotreated FCC gasoline, with the goal being octane enhancement. The preparation of the H-ZSM- 5-Al_2O_3 support consisted of incorporating 10 wt. % H-ZSM-5 into the alumina matrix. The metals were introduced using wet impregnation, with a loading ranging from 0.3 to 9 wt. % metal. Catalysts containing 2 and 3 wt. % Pt or Ni showed the highest selectivity toward heptane, while catalysts containing high Mo loadings demonstrated partial blockage of the zeolitic pores, resulting in diffusion restrictions. Additionally, Gonzalez et al. found that, even though the balance of the metal and acid function of the catalyst changed the product distribution (Lugstein A. et al., 1997), this was not the case when the Ni loadings were increased in the catalysts. This was due

to the textural and acidic properties of the catalysts, which were in both cases influenced by the Ni content. With more Ni content in the catalyst, the less acidity, less surface area, and smaller pore volume resulted. Also, the hydrogenating capacity of the catalysts was not significantly affected by the Ni loading, contrary to what was reported previously (Gonzalez et al., 2001).

1.1.2.2 Methods of Metal Incorporation into Nanoporous Supports

A number of different methodologies of metal incorporation into nanoporous supports have been presented in the literature. For example, radiolytic synthesis was used by Ramnani S. P. et al. (2008) for synthesizing SiO_2 supported Ag nanoparticles, comparing the results with the wet impregnation method for the catalytic decomposition of N_2O. Catalysts containing 5 wt. % Ag were characterized by low pressure N_2 adsorption and XRD, obtaining similar specific surface areas (337 m^2/g for the support and 220 m^2/g for the catalysts) but a difference in the Ag nanoparticle size, 8 nm and 10 nm, for the radiolytic and impregnation methods, respectively. Also, an increase in the conversion and selectivity towards N_2 was obtained for the catalyst prepared by the radiolytic method.

Exchange impregnation was employed by Melo L. et al (2008) for the preparation of Pt and Pd on MFI type [Ga]-ZSM-5 (galosilicate) catalysts. 1.0 wt. % Pt or Pd catalysts were prepared using identical methods for testing of the conversion of acetone to methyl-isobutyl-ketone (MIBK). Low pressure adsorption methods, ICP, XPS, and TEM were the main techniques used to characterize the catalysts. Although the specific surface area of the Pt catalyst decreased more than did the Pd catalyst, the dispersion was higher, and the Pt and Pd particles had roughly the same size, 1.3 and 1.2 nm, respectively. Lastly, both catalysts gave 100 % conversion in the catalytic reaction. However, the selectivity to MIBK was 91 % for the catalyst

containing Pd, while it 2as 28% for the Pt-based catalysts. As Melo et al. (2008) explained, for these types of catalytic reactions, it is known that the reactivity order is Pt > Ni > Pd (Le Page J. F. et al., 1967). Therefore, they attributed the poor performance of the Pt catalyst to its oxidation state (Pt^{2+}) and the interaction of the metal with the support ($Pt^{+\delta}$), as they observed by XPS.

Incipient wet impregnation was used by Okal J. et al. (2009) for the synthesis of Ru on gamma-Al_2O_3, aiming at the oxidation of iso- and n-butane. Catalysts having 3.5, 4.6, and 10.8 wt. % Ru were characterized by XRD, H_2 chemisorption, and TEM, obtaining the best dispersion and smallest particle size for the catalyst containing 4.6 wt. % Ru, followed 10.8% and 3.5%, respectively. In the catalytic reaction, the 4.6 wt. % Ru catalyst showed the best performance. Also, Okal J. et al. (2009) claimed that washing time and calcination conditions significantly affects the performance of these catalysts in several ways.

Microwave-assisted-polyol synthesis (Mediavilla M. et al., 2010) is another technique that has been gaining importance over the last few years. As an example, microwave-assisted-pyrol was used to synthesize 1 wt. % Pt/H-ZSM-5 catalysts that were then tested for their activity towards the toluene hydrogenation reaction (Mediavilla et al., 2010). A range of Si:Al ratios were studied in this work (22, 71, and 96), with the best catalytic activity obtained from catalysts having a 22:1 Si:Al ratio. The microwave assisted method was carried out in order to obtain Pt nanoparticles that were then incorporated by wet impregnation into the supports. Mediavilla M. et al. (2010) concluded that this method is fast and efficient for the synthesis of these types of catalysts. However, this approach has been implemented only at laboratory scale at this time.

1.1.3 Hydrocracking

In refineries, pyrolysis gasoline (pygas), a by-product of the production of ethylene and propylene, has a low monetary value in the present fuel market, and is expected to decline more in the future as a result of new environmental restrictions (Molero et al. 2009). High concentrations of aromatics, at around 60–70% of benzene, toluene, and xylenes (BTX), generate the low monetary value of pygas. However, there is still a high demand for ethylene and propylene (currently obtained from naphtha) (Raichle et al., 2001; Chang, 2000; Weirauch, 2000). High quality feedstock for the steam-cracker is obtained from the hydrocracking of pygas; therefore, the selectivity improves when the feed is light naphtha and is even better when small paraffins (C2–C4) are used. Thus, the hydrocracking of olefins has gained significant interest in the last decades in order to produce high quality synthetic steam-cracker feed for the production of ethylene and propylene (Weitkamp et al., 1996; Weitkamp et al., 2001; Raichle et al., 2001; Ringelhan et al., 2004).

These chemicals are in high demand. About 80 % of the ethylene consumed in the U.S., Western Europe and Japan is used for production of basic inorganic chemicals, such as synthetic dyes and pigments, organic chemicals such as plastics and resins, as well as pharmaceuticals, soaps, paints, and agricultural chemicals (McCoy et al., 2006). In fact, the most important applications of propylene is the production of polypropylene, which a wide range of applications, such as the manufacturing of films, packaging, caps, closures, and individual parts for the electrical and automobile industry (Cerenasa, 2013).

Hydrocracking catalysts proposed in the literature are typically composed of noble metals (Pd and Pt), supported on a support having a high surface concentration of acid sites. Therefore, an Association of Weitkamp J., Linde group, Veba Oil, and Sud-Chemie developed the

commercial catalysts used in hydrocracking the reaction that take place in a one-step process (Weitkamp et al., 1996), which is a benefit for the reaction, even though noble metals are very pricy. However, Weitkamp being one of the most well-known promoters in heterogeneous catalysts for the petrochemical industry has always used costly metals in the catalysts proposed such as: isomerization and hydrocracking of C16 n-alkanes (1983) and naphthenes (1984), alkylation of isobutene (1987) and regeneration of the catalysts (2005), and ring opening of cis-declain (2011). Whereas, Ni has also showed good activity in other hydrogenation processes (Freel et al., 1968; Rode et al., 1997; Tanaka et al., 1999; Zaera et al., 1999; Chang et al., 2003; Saadi et al., 2006; Ren et al., 2007).

Molero et al., 2009, tested a series of Ni-based catalysts supported on the acid form of the ZSM-5 zeolite (H-ZSM-5) for its ability to hydrocrack toluene, since Ni is much cheaper than noble metals and can be used for hydrogenation and other related processes and reactions (Freel et al., 1968; Rode et al., 1997; Tanaka et al., 1999; Zaera et al., 1999; Chang et al., 2003; Saadi et al., 2006; Ren et al., 2007). The Ni/H-ZSM-5 catalysts were prepared by using two methods, incipient wetness impregnation and solid state ion exchange, obtaining competitive results, especially compared to commercial noble metal containing catalysts. However, these Ni-based catalysts have not been fully characterized as yet and the distribution and environment of the metal phase is still unknown.

A mechanism for the hydrocracking of toluene was presented by Molero et al., (2009). They claimed that the metal (Ni) hydrogenates the unsaturated molecule (toluene), generating the saturated molecule (methylcyclohexane). The metal phase must be located in an appropriate acidic environment, allowing the acid sites to crack the saturated molecules into smaller molecules. This reaction may keep occurring until methane is the only final product. However,

varying the Ni loading and the reaction conditions have been the only methods available to improve the performance of these catalysts towards the production of the desirable small paraffins (C2-C4).

1.2 Naturally occurring Tight Gas/Shale Core Plugs

Tight gas and shale are a class of resources called gas unconventional gas resources, which also include coal bed methane and hydrates. Unconventional reservoirs cannot produce natural gas in economic volumes unless they are stimulated by hydraulic fracture treatment, a horizontal wellbore, or multilateral wellbores (Holditch, 2006).

Unconventional gas reservoirs are characterized by rocks with low permeability, in the micro-Darcy (tight gas) and nano-Darcy (shales) range (Figure 1.2). Research has shown that there is a large amount of natural gas in the world (Rogner,1997), with estimates of original gas in place for unconventional reservoirs being of over 32,560 Tcf globally and 8,228 Tcf in North America (Table 1.1).

The matrix pore structure of tight gas and shale gas reservoir has an important influence on hydrocarbon storage and transport; however, characterization of this pore structure is challenging. Smaller pores are usually associated with organic matter and clays, with the pores being in the meso- (> 2 nm and < 50 nm) and micro- (< 2 nm) range, limiting the number of techniques that can be used to characterize them. However, macropores (> 50 nm) are also part of the pore size distribution.

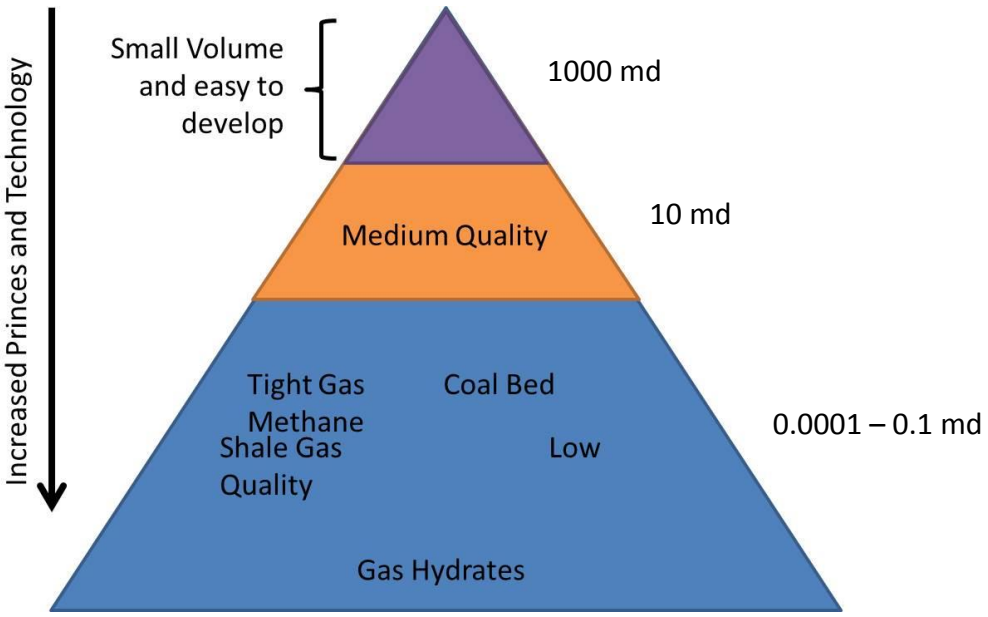

Figure 1.2 Resource triangle for natural gas. (Adapted from Holditch, 2010).

A range of characterization techniques has been used in the literature in order to determine pore size distribution in unconventional reservoirs, including high-pressure mercury intrusion (Comisky et al. 2007), X-ray photoelectron spectroscopy (Kelemen et al., 2007), low-pressure adsorption methods (Bustin et al. 2008), nuclear magnetic resonance (Kelemen et al., 2007; Sondergeld et al. 2010a,b), ion beam milling combined with SEM imaging (Sondergeld et al. 2010a), and recently, small-angle and ultra-small angle neutron scattering (Clarkson et al. 2012b). No single technique can characterize the full pore size spectrum (as seen in Figure 1.3), therefore a combination of reliable and non-destructive techniques are needed to characterize the pore structure of unconventional reservoirs. Routine methods are techniques that have been employed for several, while non-routine methods involve recent technologies, such as the DFT model for interpretation of isotherms.

Table 1.1 Distribution of natural gas in unconventional reservoirs (Modified from Holdicht, 2010).

Region	Coalbed Methane (Tcf)	Shale Gas (Tcf)	Tight Gas (Tcf)	Total (Tcf)
North America	3,017	3,842	1,371	**8,228**
Latin America	39	2,117	1,293	**3,448**
Western Europe	157	510	353	**1,019**
Central and Eastern Europe	118	39	78	**235**
Former Soviet Union	3,957	627	901	**5,485**
Middle East and North Africa	0	2,548	823	**3,370**
Sub-Saharan Africa	39	274	784	**1,097**
Centrally planned Asia and China	1,215	3,528	353	**5,094**
Pacific (Organization for Economic Cooperation and Development)	470	2.313	705	**3,489**
Other Asia Pacific	0	314	549	**862**
South Asia	39	0	196	**235**
World	**9,051**	**16,112**	**7,406**	**32,560**

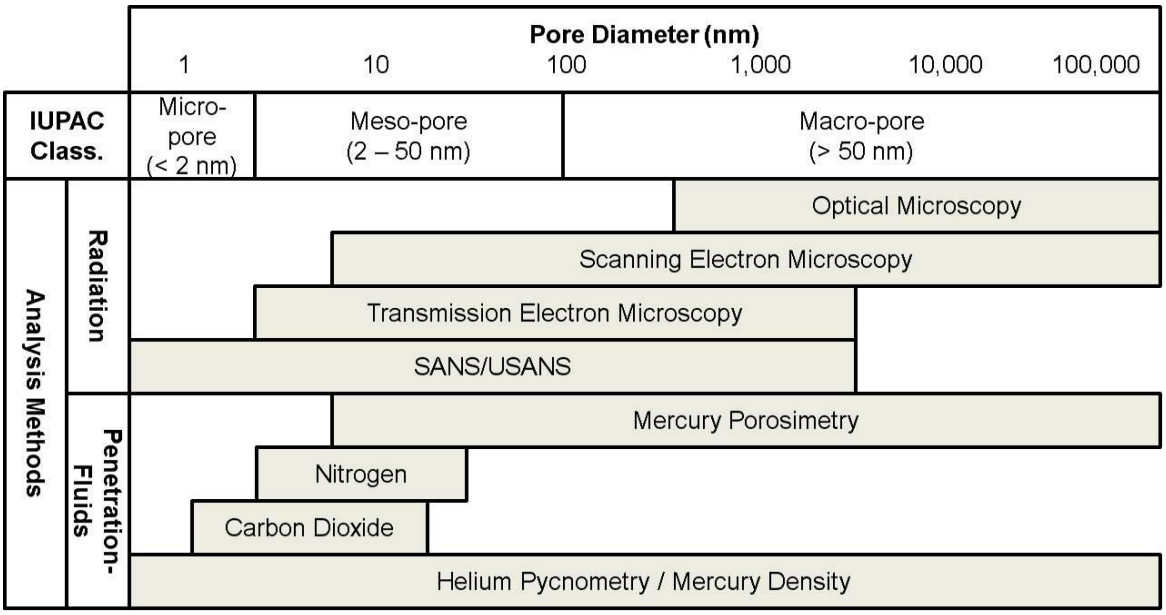

Figure 1.3 Methods used to determine porosity and pore size distributions in unconventional gas reservoirs. (Modified from Clarkson et al., 2012a).

1.2.1 Shale Gas and Tight Gas

Shale gas is found in fine-grained reservoirs in which the gas is self-sourced and some of the gas is stored in the sorbed state and free (compressed) gas, with sorbed gas predominantly stored in the organic fraction (Bustin et al., 2008). Some of the shale gas characteristics are:

- Very low permeability: 0.01 md - 1 nd,
- Low matrix porosity: 3 – 9 %,
- Variable total organic carbon (TOC) content,
- Free-(compressed) gas and sorbed-gas storage,
- Variable mineralogical composition with high clay content.

"Tight gas", on the other hand, lacks a formal definition, and usage of the term varies considerably. Some authors (Law et al., 2002) have defined tight gas as low permeability (tight)

reservoirs, with a permeability of less than 0.1 md. Thus, tight gas is the term used to identify natural gas that is dispersed in low porosity silt or sand. Some of the tight gas characteristics are:

- Low matrix permeability: 1 md – 0.01 md,
- Low matrix porosity: 3 – 9 %,
- Free-(compressed) gas stored (primarily),
- Containing clastic rocks (sand, silt) or carbonates,
- Natural fractures are present,
- Variable mineralogical composition.

1.3 Integrating Synthetic and Naturally Occurring Samples to Study

This thesis involves the characterization of two quite different types of porous materials, a set of synthetic zeolite-based catalysts (Ni/H-ZSM-5), and several tight gas and shale samples from North American unconventional reservoirs. Although these materials have different origins and usage, they both have a range of pore sizes, including nanopores, requiring specialized techniques to determine the size and distribution of the pores as well as other species contained within the pores or on the material surfaces. The techniques employed to examine the zeolite materials were secondary electron microscopy, X-ray diffraction, temperature programmed reduction, diffuse reflectance infrared Fourier transform spectroscopy, and low pressure gas adsorption, considered to be relatively conventional methods for this purpose; however, the grade of detail given in this study was beyond a common characterization while using these techniques since more resolution were employed in order to establish supporting results for terminal conclusions. In comparison, the techniques of Auger electron spectroscopy (AES), X-ray photo-electron spectroscopy (XPS), and low pressure gas adsorption were used to

characterize the tight gas and shale samples, which have not previously been integrated for characterization of these materials. XPS and AES are considered non-routine in their application to shales and tight gas samples.

1.4 Objectives

The main objective of this thesis was to characterize both synthetic and naturally occurring nanoporous materials by using a range of conventional and non-conventional characterization techniques.

Specifically, the focus of the thesis in the area of Ni-containing H-ZSM-5 catalysts is:

- To determine the nature and environment of the NiO particles in the H-ZSM-5 support.
- To establish the distribution of the NiO particles by comparing two different methods of Ni incorporation into the zeolite support.
- To observe changes in the structure of the support after incorporation of the metal.

For the naturally occurring tight gas/shale core samples, the goals are:

- To compare results obtained from non-routine and routine characterization techniques.
- To identify the chemical composition by using surface analysis techniques and establish a correlation with bulk analysis techniques.
- To determine the nature of the pore structure of the samples by using low-pressure adsorption methods.

1.5 Organization of the Thesis

This thesis is divided into five chapters. Chapter One provides an introduction to the overall research topic, a brief literature review of the two projects individually, and the goals of the thesis. Chapter Two provides detailed background information on the characterization techniques employed in this work. The results and discussion are presented in Chapters Three and Four, which focus on Ni-containing H-ZSM-5 catalysts (Chapter Three) and the naturally occurring tight gas/shale core plugs (Chapter Four) projects, respectively; each chapter including the relevant experimental methods, results, and discussion. Lastly, Chapter Five provides the overall conclusions of this research and suggestions for future work.

Note that the majority of the characterization work carried out in Chapter Three was directed towards Ni/H-ZSM-5 catalysts still in the NiO (nickel oxide) form, while Ni is in the metallic phase (reduced to Ni^0 by H_2) during the catalytic reaction. However, Ni/H-ZSM-5, and not NiO/H-ZSM-5, was used to describe the catalysts under study throughout this work, consistent with the nomenclature commonly used in the literature for these types of catalysts.

Chapter Two: **Theory of the Characterization Techniques**

In this chapter, the fundamental theory behind some of the characterization techniques used in this study to analyse both the zeolite-based catalysts and the tight gas/shale core plugs is presented. This chapter includes a brief summary of the equations, features, and applications of X-ray Photoelectron Spectroscopy (XPS), Auger Electron Spectroscopy (AES), Scanning Electron Microscopy (SEM), and Thermally Programmed Reduction (TPR).

2.1 X-ray Photo-electron Spectroscopy (XPS)

This technique is based on the photoelectric effect, discovered by A. Einstein in 1905 (for which he received the Nobel Prize in Physics in 1920). XPS involves bombarding the sample with X-ray photons with an energy range between 0.2 and 2 keV, generating an effect called photoionization. Due to the energy obtained from this effect, atoms from the surface of the sample release photoelectrons in order to relax from the high energy levels. The kinetic energy of these photoelectrons is measured with a detector; data are collected, analyzed, and associated with their previous binding energies. The binding energy is related to the properties of the atomic bonds; from this information, it is possible to obtain the chemical composition of the samples without destroying them (non-destructive) (Verna, 2007) (see Figure 2.1).

The photoelectron binding energies can be calculated using the equation of conservation of energy (2.1):

$$\boldsymbol{h\nu = E_K + E_B + E_W} \tag{2.1}$$

where $\boldsymbol{h}$ is Planck's constant, $\boldsymbol{\nu}$ is the frequency of the X-ray photons, $\boldsymbol{E_K}$ is the photoelectron kinetic energy, $\boldsymbol{E_B}$ is the binding energy of the photoelectron, and $\boldsymbol{E_W}$ is the work function

required for a photoelectron to leave the material. Each element and their different states have specific binding energies. These binding energies are well known and tabulated in the literature.

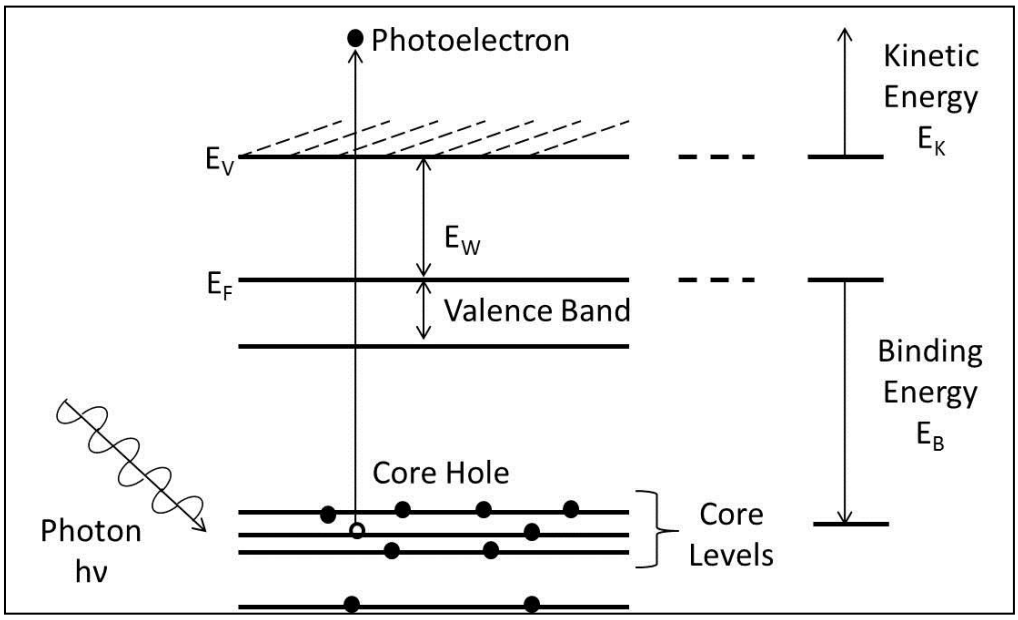

Figure 2.1 Scheme of the ejection of a photoelectron due to the impinging of a photon (adapted from Verna, 2007).

Figure 2.2 shows a schematic diagram of the XPS instrument. As seen, an ultra-high vacuum is needed ($< 10^{-8}$ Torr), the X-rays interact with the sample, and the photoelectrons emitted are captured by a retarding field lens before they enter a hemispherical analyzer that adjusts the magnetic field to filter the photoelectron according their kinetic energies. Just the photoelectrons that have the right kinetic energy are able to exit the analyzer and interact with the electron detector.

Some of the features that XPS offers include that the information is collected from a depth of 2 – 20 atomic layers (surface analysis) depending on the sample, element being analyzed (not H_2 or He), chemical species, compositional depth profiling, the methods can be non-destructive, and samples can be solids and liquids. Also, it is important to note that the X-

ray has to be monochromatic in order to determine the atomic concentration. For example, the binding energies for different carbon bonds, C-C, C-OH, C=O, O=C-O, and CO_3 (carbonate), are 284.6, 286.3, 287.5, 289.0, and 290.9 ± 0.1eV, respectively (Kelement et al., 2007). Figure 2.3 shows the XPS curve fitting of a spectrum collected from a tight gas/shale core plug from Western Canada; from this result, a distribution of the carbon species can be obtained, as seen in Figure 2.4.

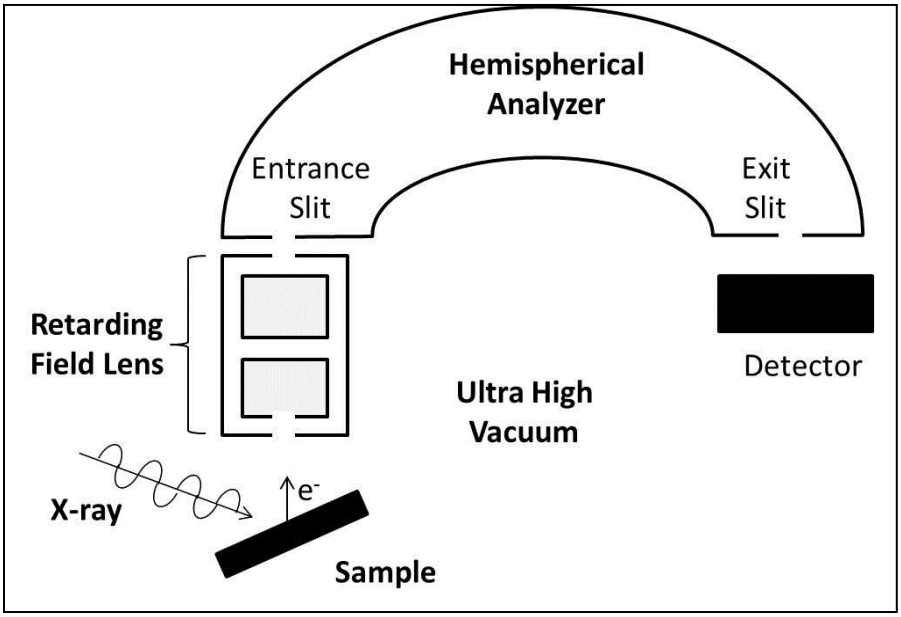

Figure 2.2 Simplified diagram of an XPS (adapted from Verna, 2007).

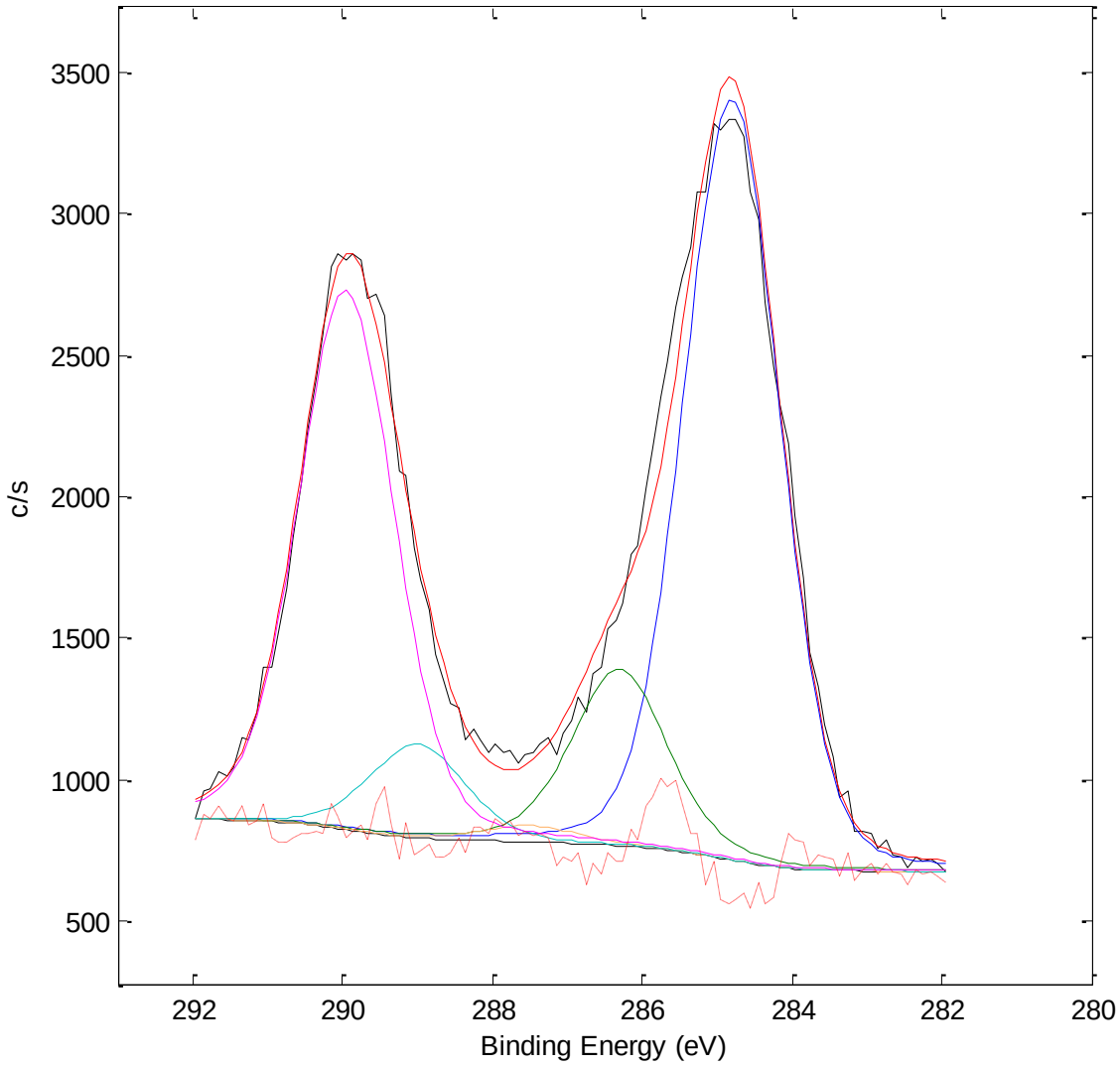

Figure 2.3 XPS curve fitting of C signal of a geological core plug sample from Western Canada. Lines are: XPS spectrum collected (black), C-C bond at 284.6 eV (blue), C-OH bond at 286.3 (green), C=O bond at 287.5 eV (yellow, not seen as it is too low), O=C-O bond at 289.0 eV (light blue), CO_3 at 290.9 eV (pink), the fitting curve (red), and the deviation of the fitting (dotted red).

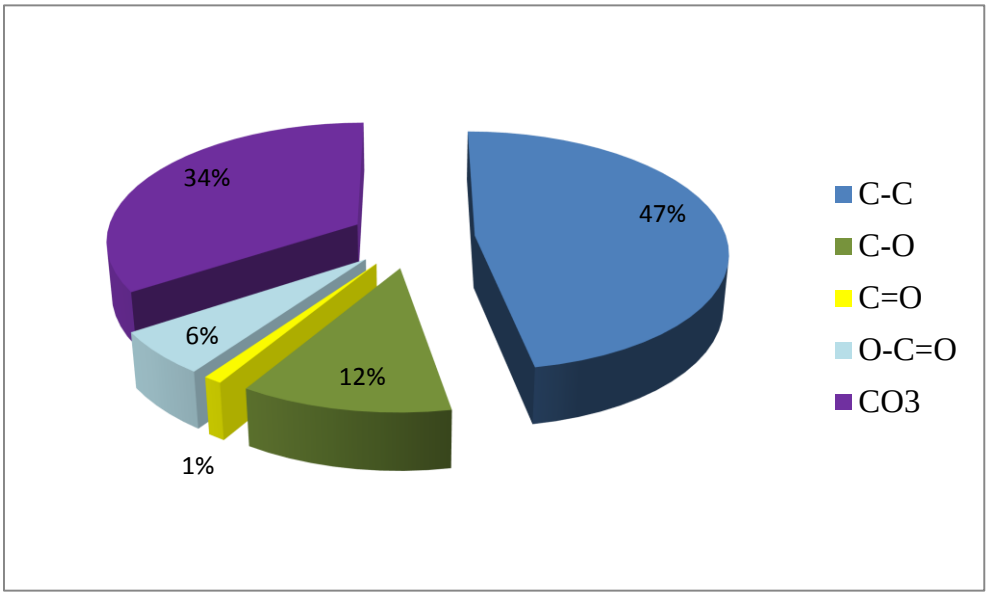

Figure 2.4 Percentage distribution of the C species that are present in the surface of the same geological sample shown in Figure 2.3.

2.2 Auger Electron Spectroscopy (AES)

AES is a surface characterization technique that obtains information from a depth into a surface of < 10 Å. This technique involves an incident electron beam that bombards the solid sample, exciting electrons within atoms near the surface of the sample, and then determining the elemental composition of material surfaces.

AES, which is based on the Auger electron effect, involves *ionization*, *relaxation* and *emission* of an electron after the sample is bombarded with an electron beam (as seen in Figure 2.5) and can be explained as follows (Vij D. R. 2006):

- A core-electron (1st electron) from the atom is removed by a high-energy incident electron, producing a vacancy in the K shell (*ionization*).

- The *relaxation* of the ionized atom occurs immediately after ionization, when another electron (2nd electron) from the L_2 level fills the hole that the 1st electron left in the K shell.
- Finally, another electron (3rd electron) is ejected (e*mission*) from the L_3 level in order to compensate for the excess energy of the exited state; this 3rd electron is called the Auger electron.

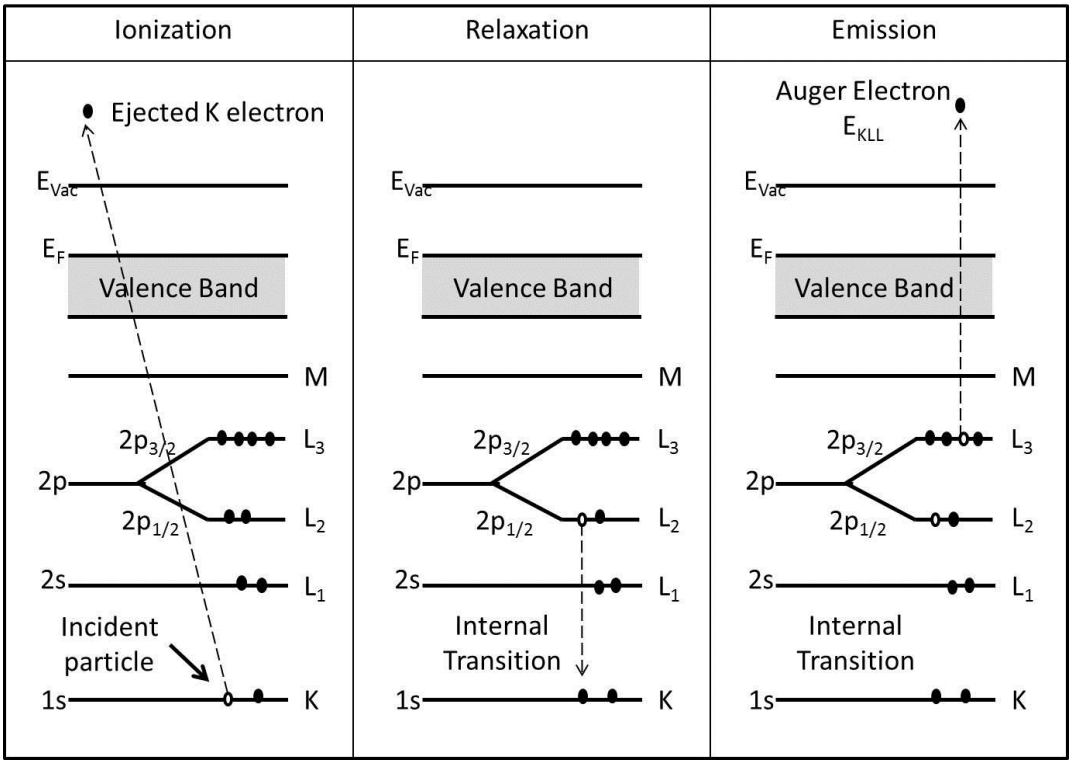

Figure 2.5 Scheme of the Auger Electron Process (adapted from Vij, 2006).

AES involves measuring the kinetic energy of the Auger electron, which is characteristic of every element present in the sample, as tabulated in AES handbooks. This kinetic energy is calculated from the following equation:

$$\boldsymbol{E_{Ae} \sim E_{e1} - E_{e2} - E_{Ael} - \phi_A} \qquad (2.2)$$

where E_{Ae} is the kinetic energy of the Auger electron detected, E_{e1} is the energy level of the first ejected electron, E_{e1} is the energy level from which the second electron falls, E_{Ael} is the energy

level from which the Auger electron is ejected, and ϕ_A is the work function of the detector, which is usually in the range of 4 eV.

Figure 2.6 Schematic representation of an AES (adapted from Vij, 2006).Figure 2.6 illustrates a schematic representation of the AES instrument, showing an electron gun (located at the centre of the apparatus) bombarding the sample stage (centre-left), a sputter ion gun for depth profile analyses (bottom-left), and analysis cylinders located into a magnetic shield and connected to a sweep supply that varies to detect the auger electron with a specific energy. This combination of devices filters the Auger electrons that are to be analyzed, while the electron detector (centre-right) is connected to the data acquisition computer (top-right).

AES is a non-destructive technique and the detection limit is around 0.1 atomic percent. It is performed in ultra-high vacuum ($< 10^{-8}$ Torr) and, similar to XPS, it is a surface technique employed to semi-quantitatively determine the chemical composition at surfaces. Typically, the AES apparatus, such as the one used for this work, contains an SEM detector, offering the ability to map a surface. It also contains an ion gun that sputters the sample surface and allows depth profiling. Mapping is very useful for elemental distribution determination, while depth profiling is employed for films, layers and coated samples to determine the film thickness.

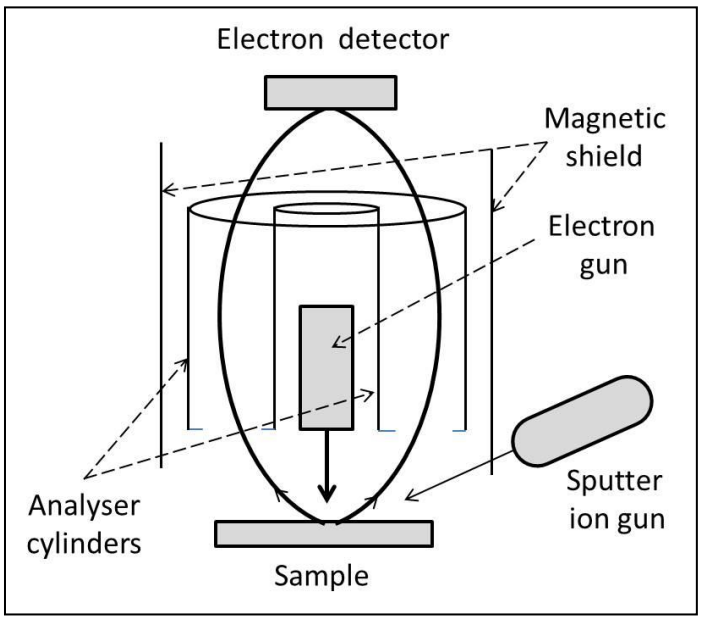

Figure 2.6 Schematic representation of an AES (adapted from Vij, 2006).

2.3 Scanning Electron Microscopy (SEM)

This type of microscopy is very useful for the study of materials, due to its high resolution for imaging (from the "nano" regime, < 1 nm – 100 nm, up to the micrometer level and beyond). In SEM, electrons are used for imaging, as their wavelength is significantly shorter than visible light (optical microscopy), giving information about particle and crystal sizes, morphology of crystals, clusters, crystalline structures by electron diffraction, and cavity dimensions, among others (Giannetto et al., 2000). In this work, scanning electron microscopy (SEM) has been used in the catalysts and the tight gas samples offering good images and quick sample preparation, similar results have been showed elsewhere (Curtis et al., 2011).

SEM works by the interaction of the incident electrons with the energy levels of the atoms of the sample, making them reach higher levels of energy. This energy difference, from the base state to the excited state, is then released in different ways, which can be detected. Many

effects occur while using SEM and involve secondary electrons (SEM), X-ray photons (EDS), Auger electrons (AES), and other effects (see Figure 2.7) that are discussed elsewhere (Williams et al., 2009). If the incident electron beam is dispersed from the sample in another direction, it takes the name of back-scattered electron microscopy (BSE). All of these physical effects can be detected and each one carries different and valuable information about the sample. A brief summary of what can be obtained using SEM is presented Table 2.1.

Table 2.1 Information obtained from different detectors used in SEM.

Technique	Information
SEM	Morphological information
EDS	Semi-quantification of chemical composition
AES	Chemical composition (Explained in more detail in previous Section)
BSE	Distribution of the elemental compounds present in the sample

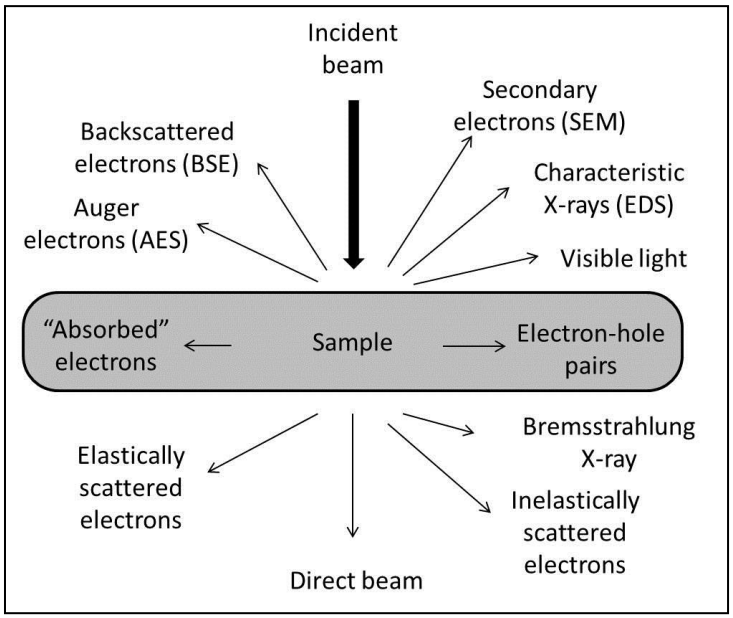

Figure 2.7 Different species and energies that are generated when a high energy electron beam interacts with a sample (adapted from Williams et al., 2009).

2.4 Temperature Programmed Reduction (TPR)

Temperature programmed reduction is a very sensitive technique that has no dependence on the properties of the materials studied other than the species that could be reduced. The reaction between metal oxide (MO) and hydrogen to form metal (M) and water vapour can be represented by the general equation showed below (2.3) (Hurst et al., 1982).

$$\boldsymbol{MO_{(s)} + H_{2(g)} \rightarrow M_{(s)} + H_2O} \quad (2.3)$$

There are models for reduction mechanisms for different oxides, better discussed elsewhere (Hurst et al. 1982). The first two models are related to bulk oxides: nucleation and contracting spheres. Nucleation model basically consist of when the reaction start when the oxide comes into contact with H_2 and is form a nuclei of the solid product. Thus, oxygen ions are removed from the metal surface to the interface metal/gas and a rearrangement of the lattice is achieved; this effect is increased by the growth of the initial nuclei and the formation of new ones (see Figure 2.8a). The contracting spheres model considers a rapidly nucleation resulting in a total coverage of the grain with a thin layer of the product. The reaction interface decreases as the reaction consumes the grain (see Figure 2.8b).

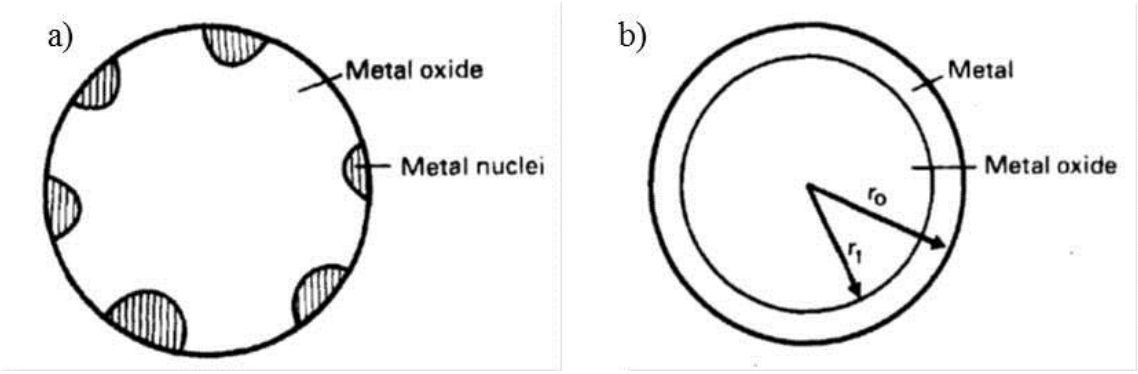

Figure 2.8 Metal oxide reduction by (a) nucleation and (b) contracting spheres mechanism. (Adapted from Hurst et al. 1982).

On the other hand, compared with the unsupported oxides, metal oxides supported on inert carriers such as γ-alumina or silica, may exhibit different reduction behaviours. Reduction may depend on the oxide-support interaction, if it exists. Supported metal oxides might be well distributed on the surface of the support or occur as islands of oxide. Islands of metal oxides may be expected to reduce in a similar manner to unsupported oxide therefore the same models can be used to express the reduction mechanism. However, metal atoms and crystallites are known to be mobile on the surface of supported metal oxides (Ruchenstein et al., 1973). Thus, if the reduction of a homogeneously supported metal oxide is performed with the reduction of individual or groups of metal ions under proper conditions, the surface diffusion that form metal crystallites may keep occurring to finally form particles of the reduced phase. However, the reduction processes may also be obstructed by metal-support interactions reducing the movement of metal atoms (Hurst et al., 1982).

Experimentally, TPR consists of monitoring the reduction reaction while linearly increasing the temperature with time. The instrumentation is relatively simple; as is shown in Figure 2.9, the reactor is charged with the certain amount of oxide sample, the reactor is heated by a control at a constant ramp, a thermal conductivity detector (TCD) measures the H_2 contained in the gas mixture (usually 5-10% H_2 in Ar) before and after the reaction. Finally, the apparatus plots a profile of H_2 consumption as a function of temperature. However, different reduction profiles may be obtained by varying the conditions (sample mass, heating ramp, concentration of H_2 in the carrier gas, and the gas flow); therefore, Malet and Caballero (Malet et al. 1988) established reasonable criteria under the conditions in order to obtain reliable profiles (better shown in Section 3.2.3.4)

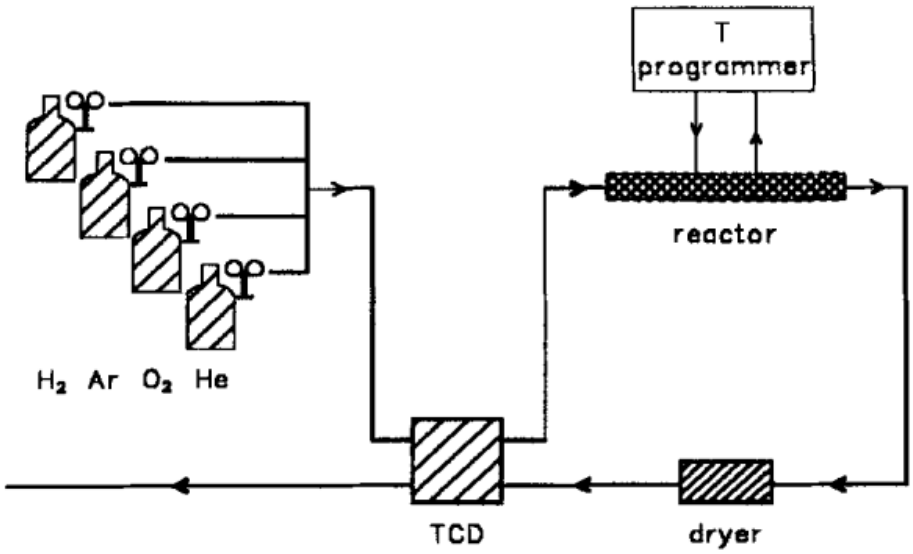

Figure 2.9 Simply scheme of a TPR experimental setup. (Adapted from Niemantsverdriet, 2000).

2.5 Gas Sorption Theory and Methods of Obtaining Information form the Isotherms

Historically, a theoretical basis for the interpretation of surface area measurements of microporous structures was established using coal and polymers. The amount of N_2 adsorbed was found to increase with increasing temperature in the temperature range of 77-180 K. Hence, it was concluded that sorption equilibrium was not reached at temperatures of 77 K (Maggs, 1952). It was shown by measuring gas adsorption on molecular sieves that N_2 diffusion is restricted when the pore diameter is smaller than approximately 0.5 nm; this critical diameter is very close to the molecular diameters of N_2 (0.3 nm) and CO_2 (0.28 nm) (Lamond et al., 1964). Moreover, if the adsorption at 77 K was carried out under equilibrium conditions, it would require more than 6 weeks to reach equilibrium. These results were coincident with results obtained at 90 K, and with results for the CO_2 surface area measured at 273 K, confirming that

the low surface areas measured with N_2 are due to the slow diffusion of N_2 into micropores (Rodriguez-Reinoso et al., 1982). Thus, N_2 is not a suitable adsorbate for materials having pores smaller than 0.5 nm, and CO_2 was recognized as a good alternative (De Jonge et al., 1996), primarily because of the higher experimental temperatures that can be applied, usually 273 K. Furthermore, the difference between N_2 and CO_2 adsorption measurements can be used to provide information regarding the pore structure of adsorbents (Garrido et al., 1987).

In physical adsorption, an inert gas is adsorbed on the outer surface of a material and on the surface of its pores, which allows for the determination of the sample surface area. Therefore, adsorption of N_2 (at 77 K) generates an adsorption isotherm. In specific cases, like for zeolites or activated carbons, the use of Ar (at 87 K) or CO_2 (at 273 or 298 K) adsorption is preferred over N_2 adsorption in order to more accurately probe the micropores. Samples with low surface area can be characterized by Kr gas adsorption. In those cases, only a portion of the isotherm can be measured, but this still provides high accuracy results. The formation of a monolayer of gas molecules (CO_2) on the surface is used to determine the specific surface area, while capillary condensation (N_2) can be used to determine the presence of pores, as well as the pore size distribution (Webb et al., 1997).

More specifically, physical gas sorption on solids is favoured with decreasing temperature and with increasing pressure. This process is exothermic and involves mass and energy transfer as well as phase change. The experiment is based on establishing an *isotherm*, including adsorption and/or desorption. The procedure consists of observing how much gas (adsorptive) $\boldsymbol{V_m}$ (in molar quantities) occurs on a clean surface of a solid (adsorbent) at constant temperature $\boldsymbol{T}$ as a function of pressure $\boldsymbol{P}$. Pressure is measured as relative pressure $\boldsymbol{P/P°}$, where $\boldsymbol{P°}$ is the saturation pressure of the gas at the temperature of the experiment and is defined as the

pressure at which a liquid boils. The graph of V_m vs $P/P°$ obtained for adsorption and/or desorption is what is called an isotherm (Webb et al., 1997).

From the shape of the isotherms, much information about the structure of the adsorbent is obtained. There are six types of isotherm that describe the adsorptive-adsorbent interaction (Sing et al., 1985) (Figure 2.10):

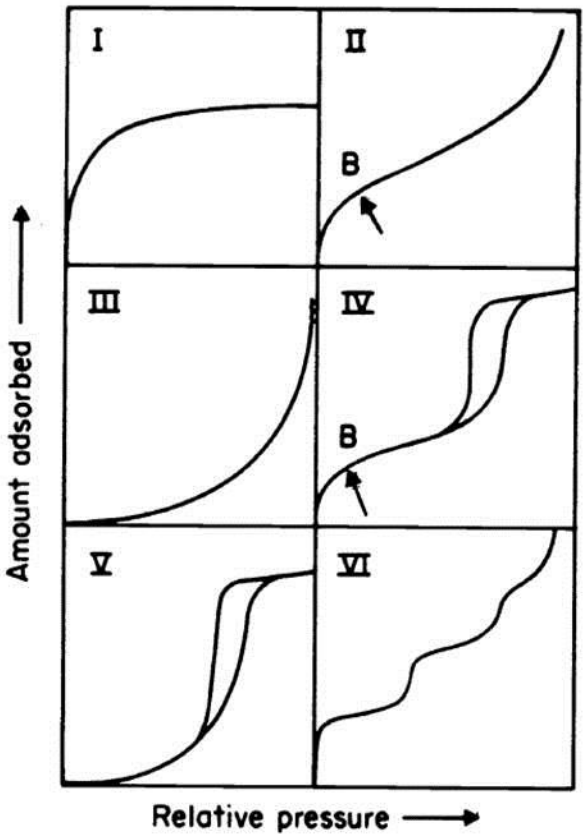

Figure 2.10 The six basic physisorption isotherms type (adapted from Sing, 1985).

- **Type I**, also called Langmuir type, indicates that the absorbent contains very small pores located in the micropore range (< 2 nm) and a small external surface area; some materials that present this type of isotherm are activated carbons, zeolites, and porous oxides.

- **Type II** is indicative of non-porous or macroporous (> 50 nm) material, representing a free multilayer adsorption. The inflexion point (B) is suggestive of full coverage of the surface with a monolayer.
- **Type III**, not showing the point B, is characteristic of conditions were the adsorptive has more affinity for one another than for the surface of the adsorbent. This type of isotherm is very uncommon, but there are some materials for which this isotherm may be obtained, i.e. N_2 on polyethylene.
- **Type IV** is very characteristic for materials having meso-porosity (> 2 nm and < 50 nm) and is characterized by a hysteresis loop formed between the adsorption and desorption branches. The hysteresis is related to the capillary condensation occurring in these pores. As there are various types of hysteresis loops, there is a sub-classification for isotherm type IV (explained below).
- **Type V** is very rare, and is related to type III were adsorptive-adsorbent interaction is weak; however, it shows some pores in the meso- range.
- **Type VI** indicates an adsorbent with a fully uniform surface (very uncommon). The steps and step height in the isotherm indicate the formation of multilayers and the monolayer capacity for each adsorbed layer, respectively. This case is seen for Ar or Kr on carbon black at 77 K.

A more detailed description of type I and IV isotherms is presented as these are the types of isotherms obtained in this work for the catalytic and geological materials, respectively:

- A microporous material isotherm (type I) shows a steep increase at low pressure due to the high adsorption capacity of the micropores. Later, a nearly horizontal section is observed, which is due to the adsorption on the external surface and in some pores larger than micropores. A saturation limit is approached at higher pressures.

- Type IV isotherms occur when adsorptive molecules close to the pore walls start experiencing attractive forces which leads to gas condensation. The condensation effect starts at low relative pressure relative the other isotherm types.

The appearance of a hysteresis loop is due to gas evaporation at lower relative pressure during desorption. With adsorption, condensation starts from the wall to the center of the pore causing a decrease in diameter. With desorption evaporation starts from a liquid surface, which is in a produced at a smaller radius than the empty pore while the adsorption generating a lag between the adsorption and desorption branches (hysteresis) until the pore is empty. The hysteresis usually closes at relative pressure higher than 0.35 P/P°).

Pore shape of mesoporous materials can be determined according to the classification of the physisorption isotherms and the hysteresis loops shape of isotherms (Fig. 2.11). A short description of the types of hysteresis loops is presented (Sing et al. 1985):

- **Type H1:** consisting of almost two vertical lines for the adsorption and desorption branch, is often obtained from materials consisting of agglomerations or compacts. Typically, the pore shape is spherical with a regular array. Hence, a narrow pore size distribution is obtained from this type of isotherm.
- **Type H2:** often obtained from porous adsorbents such as inorganic oxide gels and porous glasses; this type of isotherm hysteresis is indicative of "ink bottle" pores.
- **Type H3:** does not show a plateau at any relative pressure, often occurring for aggregates. The interpreted pore shape is plate-like or slit-shaped pores.
- **Type H4:** is often associated with narrow slit-shaped pores. The type I isotherm occurring at low relative pressures confirms the existence of micropores in the material.

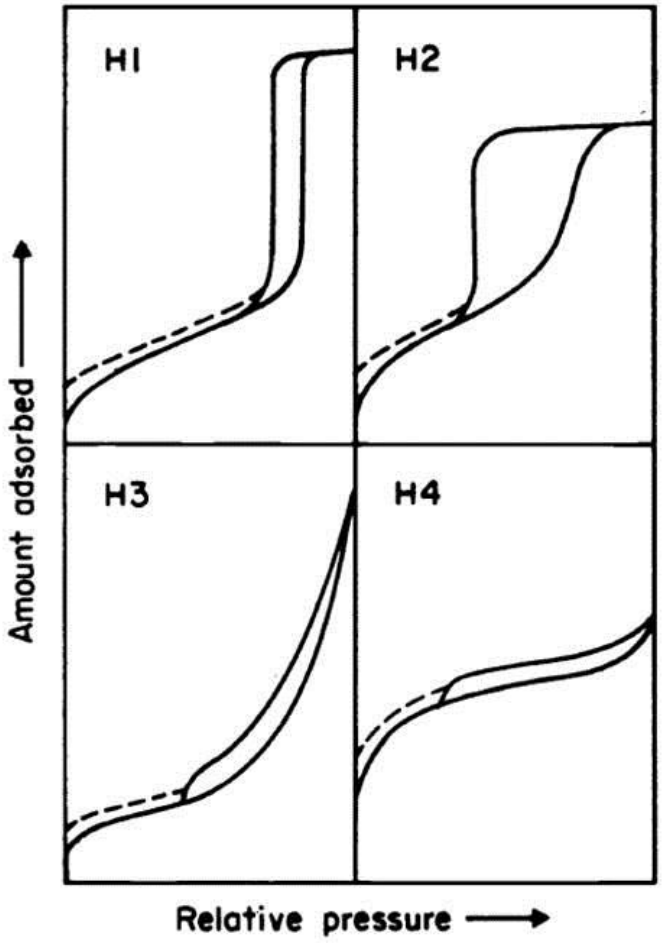

Figure 2.11 Types of hysteresis loops (adapted from Sing, 1985).

2.5.1 Langmuir Theory

This model better applies to chemisorption than physisorption; it assumes just monolayer coverage on the solid (Webb et al. 1997). The Langmuir equation (2.4) is presented below.

$$V_a = \frac{V_m bP}{1+bP} \tag{2.4}$$

where V_a is the quantity of gas adsorbed at pressure P, V_m is the quantity of gas required to cover the solid with a monolayer, and b is an empirical constant. The linear form of this equation (2.5) is used inthe software to analyze the experimental results.

$$\frac{P}{V_a} = \frac{1}{V_m b} + \frac{P}{V_m} \tag{2.5}$$

When this equation is plotted as P/V_a vs P, the slope and the Y-intercept gives the values for V_m and b. Thus, specific surface area S can be also calculated with equation (2.6):

$$S = \frac{V_m \sigma N_A}{m V_0} \tag{2.6}$$

where σ is the is the area occupied by a single molecule of the adsorptive, N_A the Avogadro number, m the mass of the adsorbent, and V_0 the molar volume of the gas.

2.5.2 BET Theory

BET Theory was developed by, Brunauer, Emmett, and Teller (BET); this theory is a generalization of the Langmuir theory for multilayer adsorption. The equation for this model (2.7) is given below:

$$V_a = \frac{V_m C P}{(P - P_0)\left[1 + (C-1)\frac{P}{P_0}\right]} \tag{2.7}$$

where C is a constant, and other variables have been previously defined in Section 2.5.1. The linear form of this equation can be obtained as seen in (2.8):

$$\frac{P}{V_a(P_0 - P)} = \frac{1}{V_m C} + \frac{C-1}{V_m C}\left(\frac{P}{P_0}\right) \tag{2.8}$$

By plotting $\frac{P}{V_a(P_0-P)}$ vs $\left(\frac{P}{P_0}\right)$, V_m and C are obtained from the slope and Y-intercept of the curve; consequently, specific surface area can also be calculated using (2.6) (Webb et al., 1997).

2.5.3 Methods for Mesoporous Materials

The range of the mesopores (> 2 nm and < 50 nm) is where the absorbent is filled with condensed adsorbate at lower pressures than the saturated vapour pressure of the adsorptive. The Kelvin equation (2.9) relates the pore size of the solid with critical condensation pressure. Refinements of the equation are made in order to avoid pore curvatures to modify the pore size obtained.

$$ln\left(\frac{P_*}{P_0}\right) = -\left(\frac{2\gamma v\cos(\theta)}{RTr_m}\right) \quad (2.9)$$

where P^* is the critical condensation pressure, γ the liquid surface tension, v the molar volume of the condensed adsorptive, θ the contact angle (θ = 0 deg for N_2), and r_m the radius of the curvature of meniscus. Taking in account other consideration explained elsewhere (Webb et al., 1997), the Kelvin equation can be written as follows:

$$ln\left(\frac{P_*}{P_0}\right) = -\left(\frac{2\gamma v}{RT(r-t)}\right) \quad 2.10)$$

where r is the pore radius and t the thickness of the condensed adsorbate. In order to solve this equation, computational models have been developed, including BJH and DFT.

In order to calculate the pore size distribution, the best option is to use Kelvin equation with the desorption branch of the isotherm since it starts from a filled pore. However, the adsorption branch can be also used for this calculation (Webb et al., 1997).

2.5.3.1 Barrett, Joyner, and Halenda (BJH)

This model was developed by Barrett, Joyner, and Halenda (Barrett et al. 1951). For each decrease in relative pressure, the thickness of the layer that is remaining on the surface of the solid is calculated. The initial modeling was performed assuming a straight cylindrical shaped pore ($\boldsymbol{volume = \pi r^2 L}$ and $\boldsymbol{area = 2\pi rL}$); however, the model has also been developed for slit-shape and spherical pores (Webb et al., 1997).

2.5.3.2 Density Functional Theory (DFT)

DFT is a practical alternative to Molecular Dynamic or Monte Carlo simulation. DFT reduces the calculation time of the computer yet provides an accurate description of inhomogeneous systems. DFT is based on Helmholtz free energy and is written in its general form as:

$$\boldsymbol{W[\rho(r)] = F[\rho(r)] + \int dr\rho(r)(V(r) - \mu)} \quad (2.11)$$

where $\boldsymbol{\rho(r)}$ is the equilibrium density (at 3-space coordinate $\boldsymbol{r}$), $\boldsymbol{V(r)}$ the potential acting on a molecule located at $\boldsymbol{r}$, and $\boldsymbol{\mu}$ the chemical potential. DFT is mathematically expressed for a single component adsorptive as:

$$\boldsymbol{Q(p) = \int dadbdc \dots q(p, a, b, c, \dots) f(a, b, c, \dots)} \quad (2.12)$$

where $\boldsymbol{Q(p)}$ is the total quantity adsorbed per unit of weigh at pressure $\boldsymbol{p}$; $\boldsymbol{a, b, c}$, ... the set of distribution properties, $\boldsymbol{f(a, b, c, \dots)}$ is the distribution function of the properties, and $\boldsymbol{q(p, a, b, c, \dots)}$ is the function describing the isotherm of the material with fixed properties $\boldsymbol{a, b, c}$, ...

At his point, different fixed properties, such as porosity and energy, can be calculated by modifying (2.12); thus, a distribution of that property is obtained; i.e. porosity in (2.13) is compacted to:

$$\boldsymbol{Q(p) = \int dH q(p,H) f(H)} \tag{2.13}$$

where $\boldsymbol{q(p,H)}$ is the quantity adsorbed per unit area at pressure $\boldsymbol{p}$ in a pore of size $\boldsymbol{H}$, and $\boldsymbol{f(H)}$ is the total area of pores of size $\boldsymbol{H}$ in the solid. Integration of $\boldsymbol{H}$ will generate the pore size distribution of the sample (Webb et al., 1997).

2.5.4 Methods for Micropores

The following methods are developed for the description of micropores (< 2 nm). It is difficult to model pores that are themselves just a little more than a gas molecule wide; therefore, the models of molecules adsorbing and forming layers on wall or large pores are no longer valid.

2.5.4.1 Dubinin-Radushkevich (D-R)

This is a semi-empirical equation that applies to the volume filling of carbons. This theory uses adsorption potential A:

$$\boldsymbol{A = RTln\left(\frac{P_0}{P}\right) = -\Delta G} \tag{2.14}$$

where $\boldsymbol{R}$ is the universal gas constant, $\boldsymbol{T}$ the absolute temperature, $\boldsymbol{\frac{P_0}{P}}$ the reciprocal relative pressure, and $\boldsymbol{\Delta G}$ the change of the Gibbs free energy. The equation for the model is expressed as:

$$\boldsymbol{W = W_0 e^{-\left(\frac{A}{\beta E_0}\right)^2}} \tag{2.15}$$

where $\boldsymbol{W}$ is the quantity absorbed at relative pressure $\frac{\boldsymbol{P}}{\boldsymbol{P_0}}$ and temperature $\boldsymbol{T}$, $\boldsymbol{W_0}$ the limiting micropore volume, $\boldsymbol{E_0}$ the characteristic energy of adsorption for the vapour, and $\boldsymbol{\beta}$ the affinity coefficient. Combining (2.14) and (2.15), we obtain a linear equation:

$$\boldsymbol{ln(W) = ln(W_0) - \left(\frac{RT}{\beta E_0}\right)^2 \left(ln^2\left(\frac{P}{P_0}\right)\right)} \tag{2.16}$$

Plotting $\boldsymbol{ln(W)}$ vs $\boldsymbol{ln^2\left(\frac{P}{P_0}\right)}$, a straight line is obtained having a slope value of $\boldsymbol{\left(\frac{RT}{\beta E_0}\right)^2}$ and Y-intercept $\boldsymbol{ln(W_0)}$. Note that $\boldsymbol{W_0}$ is a gas volume; it needs to be transformed to liquid volume in order to obtain the approximate value of the total micro-porosity (Webb et al., 1997).

2.5.4.2 Dubinin-Astakhov (D-A)

This model is more general than D-R. Starting with the same fundamentals, the exponent in this model is now variable to improve fitting of experimental data. The equation then is modified as follows:

$$\boldsymbol{ln(W) = ln(W_0) - \left(\frac{RT}{\beta E_0}\right)^n \left(ln^2\left(\frac{P}{P_0}\right)\right)} \tag{2.17}$$

where $\boldsymbol{n}$ can take values of 3, 1, and of-ten near 2 (Webb et al., 1997).

Chapter Three: **Nanoporous Ni-Incorporated Zeolite Catalysts**

In this chapter, the results obtained, using a range of techniques to characterize the synthetic nanoporous material studied in this work, are presented, and a comparison is made with earlier literature studies. Previous work has shown that Ni-loaded zeolites are highly catalytic for the hydrocracking of toluene (Molero et al., 2009), and two methods (Solid State Ion Exchange (SS) and Incipient Wetness Impregnation (WI)) were used to load the Ni onto the microporous zeolite support. The main goal of this work is to determine where the Ni is located, what the characteristics of these Ni deposits are, and what the differences are in terms of the environment and properties of the Ni on the zeolite, deposited using the SS and WI methods .

3.1 SS vs. WI Catalytic Activity Towards Toluene

This study, supported primarily by Nova Chemicals Co., originally involved a comparison of novel Ni-containing H-ZSM-5 catalysts, developed at the University of Calgary (Molero et al., 2009), with commercial Pd/H-ZSM-5 catalysts for the hydrocracking of aromatics. Commercial catalysts containing noble metals, such as Pd on H-ZSM-5, offer a high density of active sites as well as selectivity towards small paraffins obtained from feedstocks, e.g., benzene, toluene and xylenes (BTX). The hydrocracking reaction gains importance when py-gas (low value olefin) is hydrocracked into small paraffins (C2 - C4), which are high quality feedstocks used for the steam-cracker reaction for the production of ethylene and propylene (Raichle et al., 2001; Chang, 2000; Weirauch, 2000).

Ni-supported ZSM-5 catalysts are currently being developed to replace Pd, as Ni is significantly lower in cost and is known to be active in hydrogenation and several other related

processes and reactions (Freel et al., 1968; Rode et al., 1997; Tanaka et al., 1999; Zaera et al., 1999; Chang et al., 2003; Saadi et al., 2006; Ren et al., 2007). Our earlier results (Table 3.1) showed comparable activity of the Ni- and Pd-based catalysts (Molero et al., 2009). However, how and where Ni is distributed in the < 1 nm sized pores of the H-ZSM-5 zeolite and the nature of the metal-zeolite support interactions have not yet been clarified.

Previously in our group, catalysts have been prepared by using two well-known methods, Solid State Ion Exchange (SS) and Incipient Wetness Impregnation (WI). The biggest difference between them is that the WI method can be readily used at the industrial scale (Molero et al., 2009). The SS method, developed in 1973 (Rabo et al., 1973; Clearfield et al., 1973), has been reported more recently in the literature as a "highly efficient procedure", which involves mechanical mixing of the metal salt and the solid zeolitic support, apparently offering a higher degree of exchange compared with the WI method (Kucherov et al., 1994; Karge, 1997; Kinger et al. 2000). On the other hand, WI is limited by the formation of hydrated shells around the exchangeable metal ion (Barrer, 1979); hydration occurs when the Ni salt is dissolved in water dissociating the ions and interacting with the solvent (Harvey et al., 1963). Therefore, WI requires calcination after impregnation of the metal phase in order to allow the cations to migrate onto the support surface and into the pores. Further, repeated impregnation is sometimes required to achieve higher exchange levels and thus better metal dispersion (Kinger et al., 2000).

Table 3.1 shows the selectivity of the catalysts developed in our group (Ni-based) during the hydrocracking of toluene, producing small paraffins, compared to the commercial Pd-based catalysts (Hernandez, 2012). Note that, for the WI prepared catalyst, the reaction was run at two different temperatures. The temperature employed by Hernandez (2012) to investigate the deactivation of the catalyst was 370 °C, while 400 °C is the conventional operating temperature.

Table 3.1 % Selectivity of the Ni (1 wt. %)-H-ZSM-5 catalysts, prepared by the SS and WI methods and compared to the commercial Pd-based catalysts for the hydrocracking of toluene. 370 °C and 400 °C indicate the temperature at which the catalytic reaction was run at a WSHV of 2.60 h^{-1}, H_2 flow of 128 sccm, and a total H_2 pressure of 6 MPa (Hernandez, 2012).

Product % (+/- 0.5 %)	Commercial (370 °C)	WI (370 °C)	WI (400 °C)	SS (400 °C)
Toluene	1	0	0	0
Methylcyclohexane	4	3	0	0
Benzene	3	2	0	0
Pentane	2	4	1	2
Butane	**---**	**---**	**9**	**12**
Iso-butane	**46**	**38**	**13**	**17**
Propane	**41**	**43**	**49**	**50**
Ethane	**2**	**6**	**20**	**13**
Methane	1	4	8	6

The first observation for the Ni-based catalysts is that 100% conversion of the toluene hydrocracking reaction was obtained for both Ni-incorporation methods and at both temperatures (Molero et al., 2009). The second observation is that, for the WI and SS catalysts, 91% and 92% of the products are C2-C4 alkanes, respectively; these are the desirable products of this reaction (as explained above). Another plus of the Ni-based catalysts is that the aromatic rings are being fully cracked, since no methylcyclohexane or benzene was produced. However, note that methane, which is a product of little value, is produced in yields that increase up to 8% for the WI catalyst and 6% for the SS catalyst.

Table 3.2 shows the selectivity (towards small paraffins) of the Ni-based WI catalysts, with varying Ni contents (0.5, 1, 1.3, 2, and 5 wt. %), during the hydrocracking of toluene. As seen, 100% conversion was obtained (Hernandez, 2012) from the catalysts containing 1 wt. % Ni or higher loadings. The largest amount of the C2-C4 paraffins is obtained from the 1 wt. % Ni on the H-ZSM-5 (91%) material, while the other catalysts show C2-C4 paraffins with yields of 72%, 38%, 38%, and 17% with 1.3, 0.5, 2, and 5 wt. % Ni on H-ZSM-5, respectively. Finally, the quantity of methane produced by these catalysts increases as the Ni content increases. The appearance of benzene and xylene for the 0.5 wt. % Ni on the H-ZSM-5 catalyst is due to the disproportionation of toluene (Molero et al., 2009). As seen in Table 3.1 and Table 3.2, there are only minor differences in the catalytic reaction (yield and selectivity) for these catalysts, whether employing the SS or WI methods for their synthesis. However, at a larger scale (industrial level), these differences could become significant.

Thus, several key questions remain. The first is to understand where the Ni component is located and what the local environment is, both as a function of Ni loading, while a second is to determine if there are any differences in these characteristics for the SS vs. WI catalysts, especially considering the rather different synthetic methods used to produce them. To achieve these goals, a wide range of techniques was employed to establish the morphology, crystalline structure, reducibility, pore volume, and specific surface area of these nanomaterials. The methods used in this work include X-ray Diffraction, temperature programmed reduction, diffuse reflectance infra-red Fourier transform spectroscopy, and low pressure gas sorption analysis (N_2 and CO_2), all aimed at determining where the Ni is located (for example, whether it is present as Ni nanoparticles on the surface of the pore walls of the zeolite or is embedded chemically in the

catalyst surface, and with what particle sizes) and how the Ni metal and the zeolite support are interacting.

Table 3.2 % Selectivity of the Ni-based catalysts, prepared by WI, towards the hydrocracking of toluene. Reaction was run at 400 °C, WSHV 0.93 h-1, H_2 flow of 128 sccm and a total H_2 pressure of 6 MPa (Hernandez, 2012).

Product % (+/- 0.5 %)	0.5 wt. % Ni on H-ZSM-5	1 wt. % Ni on H-ZSM-5	1.3 wt. % Ni on H-ZSM-5	2 wt. % Ni on H-ZSM-5	5 wt. % Ni on H-ZSM-5
Xylene	17	0	0	0	0
Toluene	31	0	0	0	0
Benzene	10	0	0	0	0
Pentane	0	0	0	0	0
Iso-Pentane	1	1	0	0	0
Butane	5	9	3	1	0
Iso-butane	6	13	10	2	0
Propane	19	49	37	13	2
Ethane	8	20	22	22	15
Methane	3	8	28	62	83

3.2 Materials and Methods

3.2.1 Support and Metal Phases

There are two key functional stages involved during hydrocracking reactions, the hydrogenation and the cracking stages. The catalysts used for these purposes in the present work contained two phases, a zeolitic support phase and Ni as the metal phase. The support phase must be capable of performing the catalytic reaction at as many sites as possible, also being a friendly support for

the metal. Thus, ZSM-5 zeolite was chosen as the support for this work, due to its large surface area (over 300 m^2/g) for catalytic reactions and a pore size (slightly elliptical shape 0.51 x 0.57 nm (Weitkamp, 2001)). Pentasil is the unit cell of ZSM-5 (see Figure 1.1), which contains intercepting ten-membered-ring pores (number of tetrahedra in the ring), with one type of pore being straight and the second being semi-sinusoidal (Weitkamp 2001). While the crystal structure of ZSM-5 is monoclinic (90 deg), it is orthorhombic (90.67 deg) when the template used to construct it has not been removed yet (van Koningsveld et al., 1990).

Both of the pore types in ZSM-5 are close in size to the kinetic diameter of toluene (5.8 Å), and thus toluene was selected as the feedstock for the catalytic reaction in this project (Molero et al., 2009). Toluene is more strongly adsorbed on ZSM-5 and diffuses more rapidly on the pore walls of ZSM-5 compared to benzene or ethyl-benzene (Malherbe R. R. et al., 2003; Xiao J. et al., 1992). Additionally, the acid form of this zeolite (H-ZSM-5) has a large number of Bronsted and Lewis acid sites, due to Al^{3+} in the framework and silanols as the morphological defects. Ni is known as a very good hydrogenation catalyst and competes with the performance of Pd and other transition metals.

3.2.2 Synthesis of the Catalysts

The materials employed for zeolite synthesis were a 40% LUDOX suspension in water (Aldrich), Ni (II) nitrate hexahydrate ($Ni(NO_3)_2.6H_2O$, Aldrich), ammonium acetate (minimum 98%, Aldrich), tetrapropylammonia hydroxide (40% w/w aq. soln., Alfa Aesar), sodium aluminate ($NaAlO_2.xH_2O$, Merck), and sodium hydroxide (97% purity, EDM chemicals), with distilled, deionized water used as the solvent.

The ZSM-5 zeolite was synthesized following an in-house method (Molero et al., 2009), consisting of mixing all of the materials together in a beaker with deionized water under stirring. LUDOX was the last material to be added dropwise in order to avoid the formation of a gel. Then, the solution was thermally treated in an auto-clave at 190 °C for 36 h in order to crystallize the ZSM-5 zeolite. The ZSM-5 zeolite was then washed with distilled water until a pH of 5 was obtained in the aqueous effluent.

The acid form of the zeolite was achieved by stirring the zeolite with 3 M ammonium acetate for 4 h at 60 ºC, washing with distilled water, and then drying at 80 °C overnight before calcination at 500 ºC for 4 h. Ni was then incorporated using two techniques, solid-state ion exchange (SS) or incipient wetness impregnation (WI), using Ni loadings from 0.5 to 3% wt. SS was achieved by calcination at 450 ºC for 12 h in air after mechanical mixing of the zeolite and the Ni nitrate salt. WI involved preparing a solution of Ni nitrate in water and then adding this solution to the zeolite one drop at the time until a slurry was formed during the mixing. These samples were then dried at 80 ºC for 8 h and calcined at 450 ºC for 12 h. Note that, for both of those Ni incorporation methods, the calcination temperature was set below the calcination temperature of the zeolite (450 ºC). This procedure was employed in order to avoid any changes in phase or structure of the support. Sample codes are presented in Table 3.3.

Table 3.3 Catalysts Sample Codification

Nickel Loading (wt. %)		**0.5**	**0.8**	**1.0**	**1.3**	**2.0**	**3.0**
Metal Incorporation Method	**SS**	SS0.5	SS0.8	SS1	SS1.3	SS2	SS3
	WI	WI0.5	WI0.8	WI1	WI1.3	WI2	WI3

3.2.3 Analytical Methods

3.2.3.1 Scanning Electron Microscopy (SEM)

Morphological structure and possible changes during the preparation steps were tracked by using a PHILLIPS SEM XL30 microscope, located at the Microscopy & Imaging Facility (MIF) at the University of Calgary in the Health Sciences Centre. The samples analyzed were the zeolite as-made, the zeolite in the acid form, and the Ni/zeolite catalysts as-made.

3.2.3.2 X-ray Diffraction (XRD)

XRD analysis of the Ni-zeolite catalysts was carried out using a RIGAKU ULTIMA III spectrometer, equipped with Cu K_α radiation (0.15418 nm) (Chemical and Petroleum Engineering Department at the University of Calgary). Experimental parameters employed were a 0.01 deg step size and 0.5 deg/min scan rate and Jade® (version 8.0) for the interpretation of the diffractograms.

Simulated XRD of the Ni-zeolite catalysts were obtained using Powder Cell 2.4. The lattice parameters of H-ZSM-5 were included in this software in order to obtain simulated diffractograms as close as possible to the real samples.

3.2.3.3 Temperature-Programmed Reduction (TPR)

For the Ni-zeolite catalysts, TPR was performed in a Quantachrome Chembet 3000 instrument (Department of Chemical and Petroleum Engineering at the University of Calgary), following recommended conditions from Malet & Caballero (1988). They concluded that there is a P value related to experimental parameters in the apparatus, and then the sample mass can be calculated using (3.1) in order to obtain better results. They claimed that having a P value below 20 K

ensures good results. In this study, P was set at 2 K to identify the catalysts having good quality TPR profiles. The heating ramp ($\boldsymbol{\beta}$) was 10 °K/min, the H_2 concentration ($\boldsymbol{C_0}$) was 10% in an Ar flow ($\boldsymbol{F}$) of 15cc/min, and the reducible species mass ($\boldsymbol{S_0}$) was 1 mg.

$$P = \frac{\beta S_0}{F C_0} \tag{3.1}$$

3.2.3.4 Diffuse Reflectance Infrared Fourier Transform Spectroscopy (DRIFTS)

In-situ DRIFTS was carried out in a Thermo Nicolet Avatar 360 FTIR Spectrometer using a high temperature cell in which samples were heated in steps to 80 ºC, 120 ºC, 200 ºC and 400 ºC, at 10 ºC/min ramp, in a flow N_2. A waiting time of 2 h was set for temperature stabilization; this was established as a criterion for the collection of the spectra and to avoid observing the infra-red water band. To work at higher temperatures, an in situ cell was used. As seen in Figure 3.1, this cell contained KBr windows transparent to IR light, allowing it to pass through to the sample and then be collected by the detector. The cell also contained a catalyst bed for the sample, a ceramic crucible where the heating wires are located, a gas inlet and outlet to create different gas atmospheres, and a metal base.

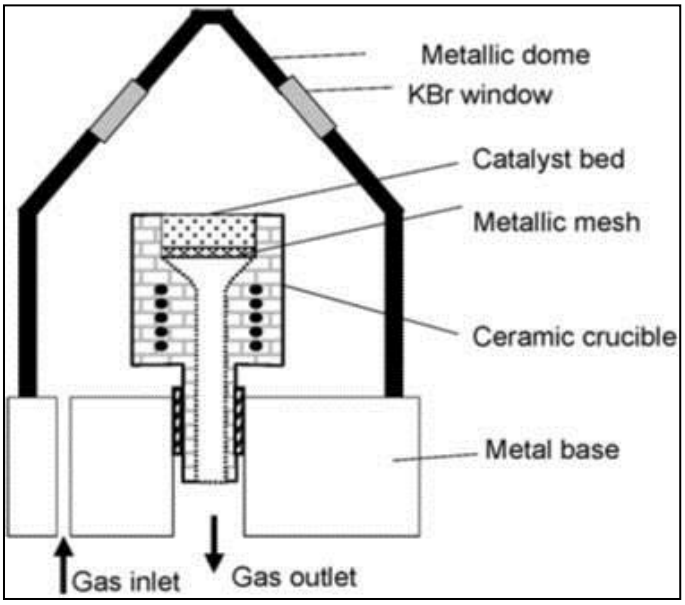

Figure 3.1 Schematic representation of a DRIFTS cell (Maunier, 2010).

3.2.3.5 Low Pressure N_2 and CO_2 Gas Sorption Analysis

Low pressure N_2 and CO_2 adsorption analyses were performed on a Micromeritics Tristar 3000 Analyzer (Department of Chemical and Petroleum Engineering at the University of Calgary), using DFT theory to obtain validation of a previous study (Molero et al., 2009). In this case, catalysts were degased at 150 ºC for 4 h. N_2 adsorption and desorption isotherms were collected at 77 K using BET and BJH methods. CO_2 adsorption isotherms were collected at 0 ºC, while the specific surface area was determined by using BET, Langmuir, and DFT methods.

3.3 Results and Discussion

3.3.1 Morphological Characteristics Determined by Secondary Electron Microscopy (SEM)

The acid form of the ZSM-5 zeolite, obtained following a method employed previously (Molero et al., 2009), showed reproducibility in its morphological structure. Here it is shown that the

method employed to incorporate the metal (Ni) does not seem to influence the morphology of the catalysts in any detectable way. Figure 3.2, Figure 3.3 and Figure 3.4 (SEM images of the zeolite H-ZSM-5, SS2 and WI3, respectively) show that catalysts prepared by the SS and WI methods look the same as H-ZSM-5, showing spheres between 5 and 7 μm in diameter. As seen in previous work in this project (Molero et al., 2009), the average zeolite particle size is ~ 7 μm when it was prepared using the following methodology (Section 3.2.2). However, it is known that different zeolite particle sizes and pore diameter can be obtained by varying the synthesis conditions, such as the temperature of synthesis, pH, and pressure; as other authors have reported (Selvin R. et al., 2008; Firoozi M. et al., 2009; Reddy J. K. et al, 2012). Higher magnification images (as seen in Figure 3.4b) were obtained in order to confirm that the morphological structure of the support did not change after Ni incorporation, even at the 100 nanometer scale, as was also observed at the highest Ni loadings of 5 – 30 wt. %.

Previous work in our group (Molero et al., 2009) also showed that the incorporation of low loadings of Ni in the H-ZSM-5 zeolite using both methods produces no obvious change in the zeolitic structure; this could be seen at a scale of 100,000 X using SEM. The same results were obtained for the catalysts studied in this work, regardless of the Ni incorporation method used. The primary morphology seen in these samples is spheres with sizes between 5 and 10 μm in diameter; these spheres appear to be an agglomeration of slabs, as seen in Figure 3.4b. Some particles have other geometrical shapes and larger crystals are also seen (Figure 3.3a), most probably being zeolitic particles that did not form the typical ZSM-5 particle shape during synthesis. However, the quantity of these more unusual types of crystals was typically less than 2%.

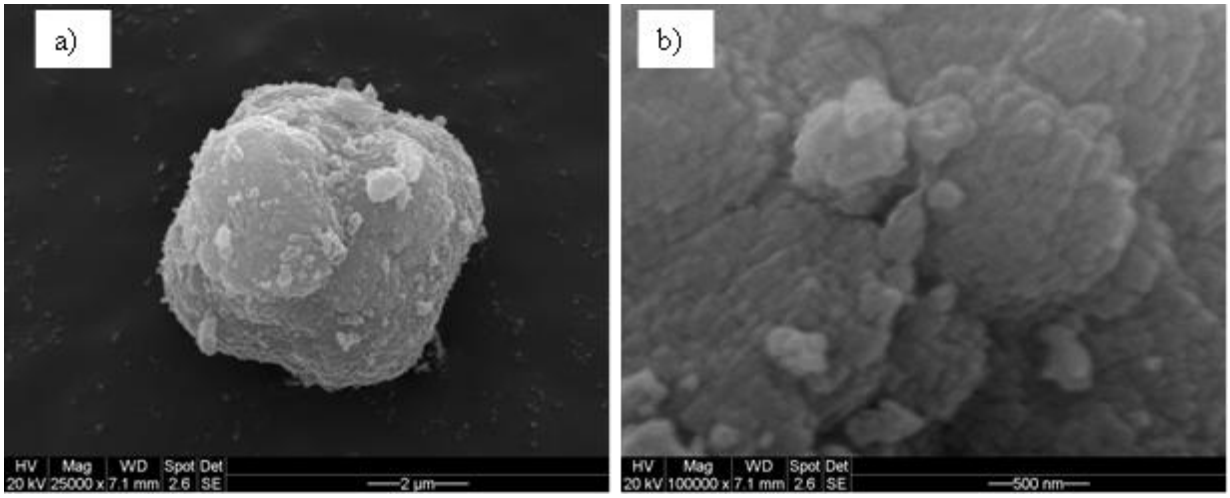

Figure 3.2 SEM images of H-ZSM-5 as made at two different magnifications: a) 25,000 X and b) 100,000 X.

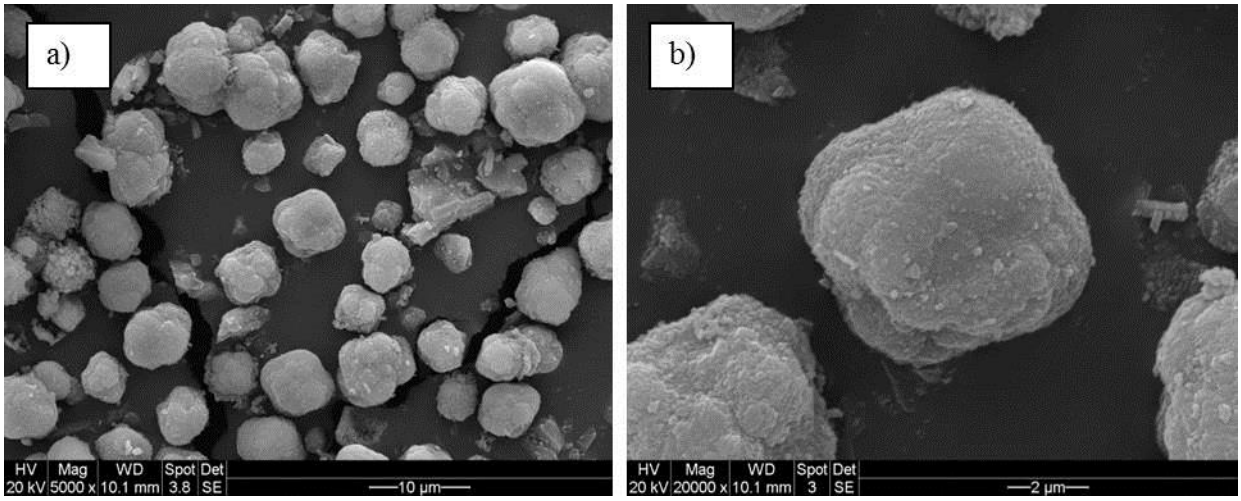

Figure 3.3 SEM images of WI3 catalyst at two different magnifications: a) 5,000 X and b) 20,000 X.

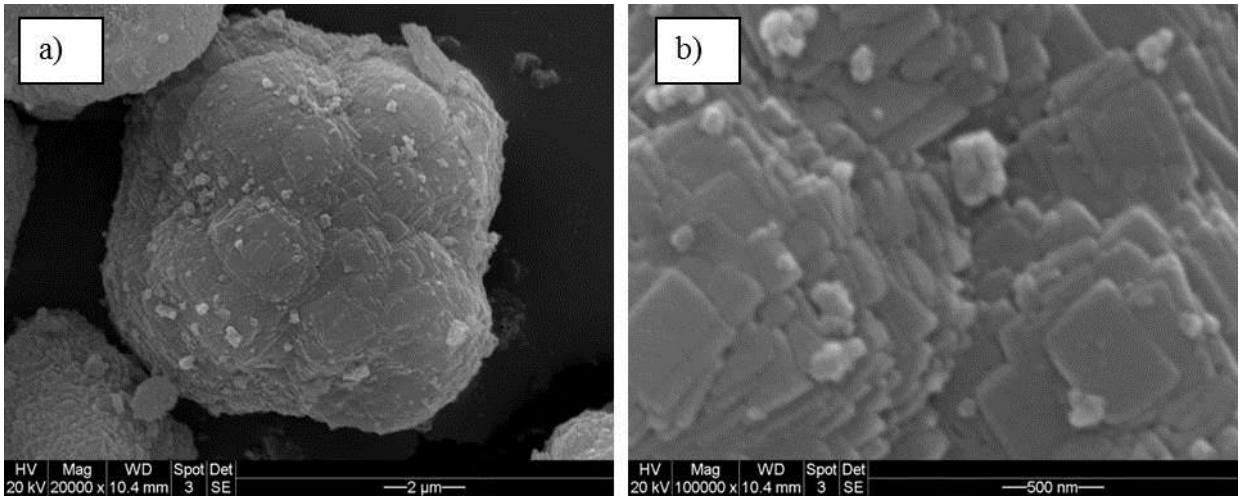

Figure 3.4 SEM images of SS2 catalyst at two different magnifications: a) 20,000 X and b) 100,000 X.

Energy-dispersive X-ray spectroscopy (EDS) was performed on these samples once they were in the microscope, obtaining the results shown in Table 3.4. Note that the nominal Ni content of the catalysts does not match the results obtained by EDS very closely, although the trends in the Ni content do match. EDS is an analytical technique that fails (similar to XRD) when the concentration of an element in a sample is < 2%.

Table 3.4 Quantification of Ni by EDS analysis.

Catalysts prepared by SS	Ni wt. % by EDS	Catalysts prepared by WI	Ni wt. % by EDS
SS0.5	0.3	WI0.5	0.3
SS0.8	0.3	WI0.8	0.6
SS1	0.5	WI1	0.8
SS1.3	1.1	WI1.3	1
SS2	1.6	WI2	1.9
SS3	3.4	WI3	2.9

3.3.2 X-ray Diffraction (XRD)

3.3.2.1 Fast XRD Experiments

XRD analysis was used to verify the crystal structure of the ZSM-5 zeolite and NiO after its incorporation into the zeolite using the two different Ni loading methods. Fast XRD experiments (step size and scan rate) are usually capable of giving good results (Molero et al., 2009). However, a less noisy spectrum with good peak intensities may be obtained by increasing the resolution of the diffractograms, which is achieved by lowering the speed of the scan parameters to "slow XRD experiments" conditions. The scan parameters include the step size and the scan rate, i.e., how much the goniometer is moving from scan to scan and how many degrees the goniometer moves per unit time, respectively. Additionally, XRD cannot detect particles smaller than a few nanometers in size. Therefore, this technique is more useful for detecting the presence of small agglomerations of NiO (> 10 nm) on the zeolite surface.

When fast XRD experiments were used (step size: 0.02 deg, scan rate: 2 deg/min), diffractograms of the Ni/H-ZSM-5 catalysts (SS and WI) did not show any significant differences, compared to the H-ZSM-5 support itself. However, as explained above, better resolution was obtained when slower scans (step size: 0.01 deg, scan rate: 0.5 deg/min) were employed, as was done with all of the catalysts studied in this work. The XRD patterns of the catalysts prepared by SS and WI are shown in Figure 3.5a and Figure 3.5b, respectively (note that, in both figures, the bottom pattern belongs to the H-ZSM-5 zeolite alone).

Additionally, XRD patterns of samples with a higher Ni content (10, 20 and 30 wt. %) were obtained (Figure 3.5c) in order to verify that the NiO XRD pattern is correct. The most intense peaks corresponding to NiO belong to the [111] and [200] crystal planes at 37.25 and 43.30 degrees, respectively (Tao et al., 2004). However, catalysts having a high Ni content showed NiO agglomeration, since a change in the color (from white to a darker grey) could easily be observed as the Ni content increased.

However, it was not possible to completely identify the peaks corresponding to NiO in the patterns obtained for the catalysts prepared by SS, since they are not seen clearly when the fast XRD experiments were used ([2,0,0] peak in Figure 3.5a). The Ni particles are thus either amorphous or very small (< 0.5 nm) and well dispersed in the SS materials so that XRD cannot detect them. In fact, it is quite likely that the SS catalysts contain only very small NiO particles, consistent with the results obtained by XRD simulations (Section 3.3.2.2).

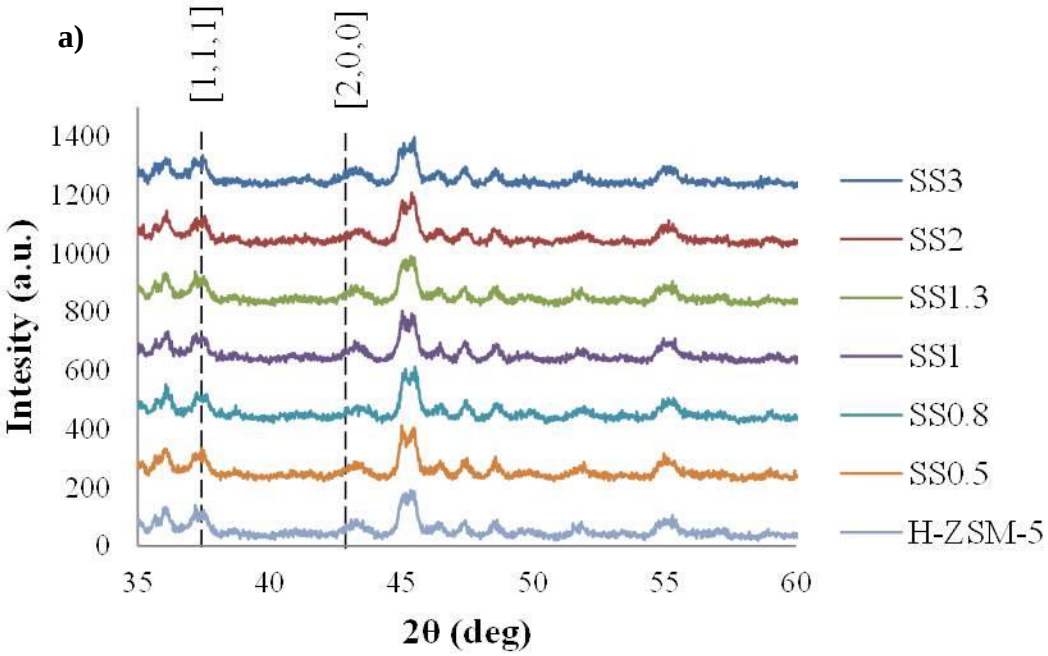
a)
[1,1,1]
[2,0,0]
Intesity (a.u.)
1400
1200
1000
800
600
400
200
0
35
40
45
50
55
60
2θ (deg)
SS3
SS2
SS1.3
SS1
SS0.8
SS0.5
H-ZSM-5

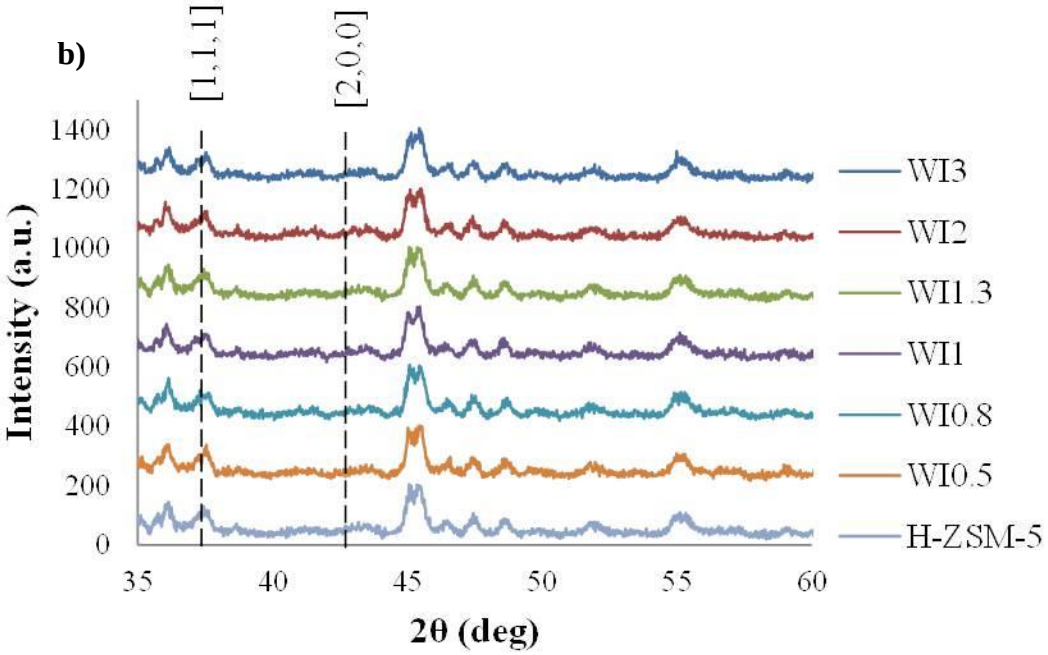
b)
[1,1,1]
[2,0,0]
Intensity (a.u.)
1400
1200
1000
800
600
400
200
0
35
40
45
50
55
60
2θ (deg)
WI3
WI2
WI1.3
WI1
WI0.8
WI0.5
H-ZSM-5

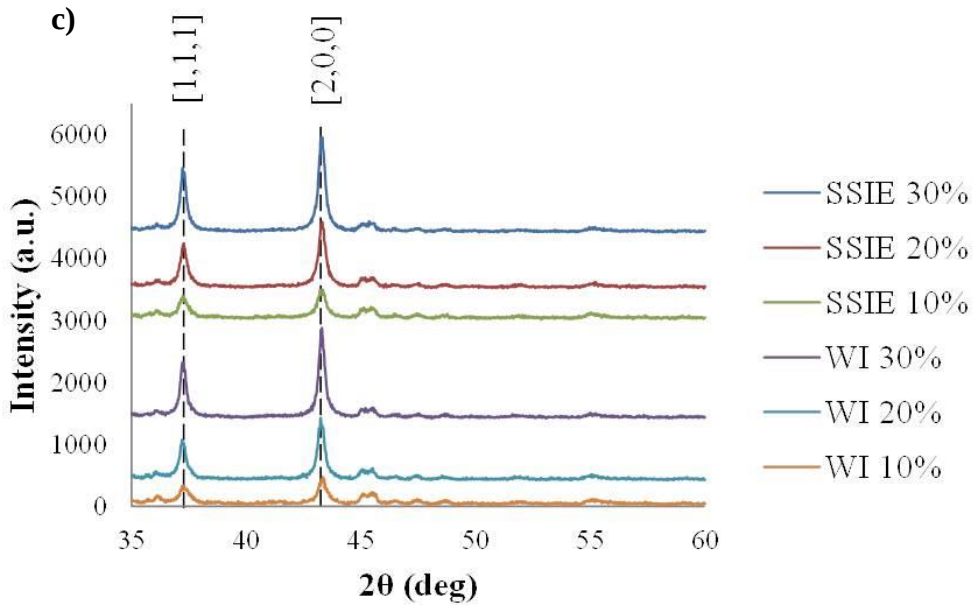

Figure 3.5 XRD patterns of: a) SS catalysts and H-ZSM-5, b) WI catalysts and H-ZSM-5 and c) SS and WI catalysts containing > 5 wt. %. NiO [111] and [200] planes are identified at 37.25 and 43.30 degrees, respectively. Scan parameters: step size: 0.01 deg, scan rate: 0.5 deg/min.

3.3.2.2 Slow XRD Experiments

Slow XRD experiments were performed using the following conditions: step size: 0.01 deg, scan rate: 0.5 deg/min, with clear differences seen in the XRD patterns. Figure 3.6a shows the superposition of the patterns of an as-made H-ZSM-5 and a SS2 catalyst. The main difference appears at 43.30 degrees, where the peak of the Ni [200] plane is located. The other peak at 37.25 degrees for the [111] plane is not well defined, due to the noise in the diffractogram. The same behaviour was observed for the WI2 catalyst (Figure 3.6b). However, note that a shift in

the peak is identified with a blue arrow in Figure 3.6b. This peak can also be associated with the [2,0,0] plane of NiO, due to the size of the crystal domain of the particle (Figure 3.8).

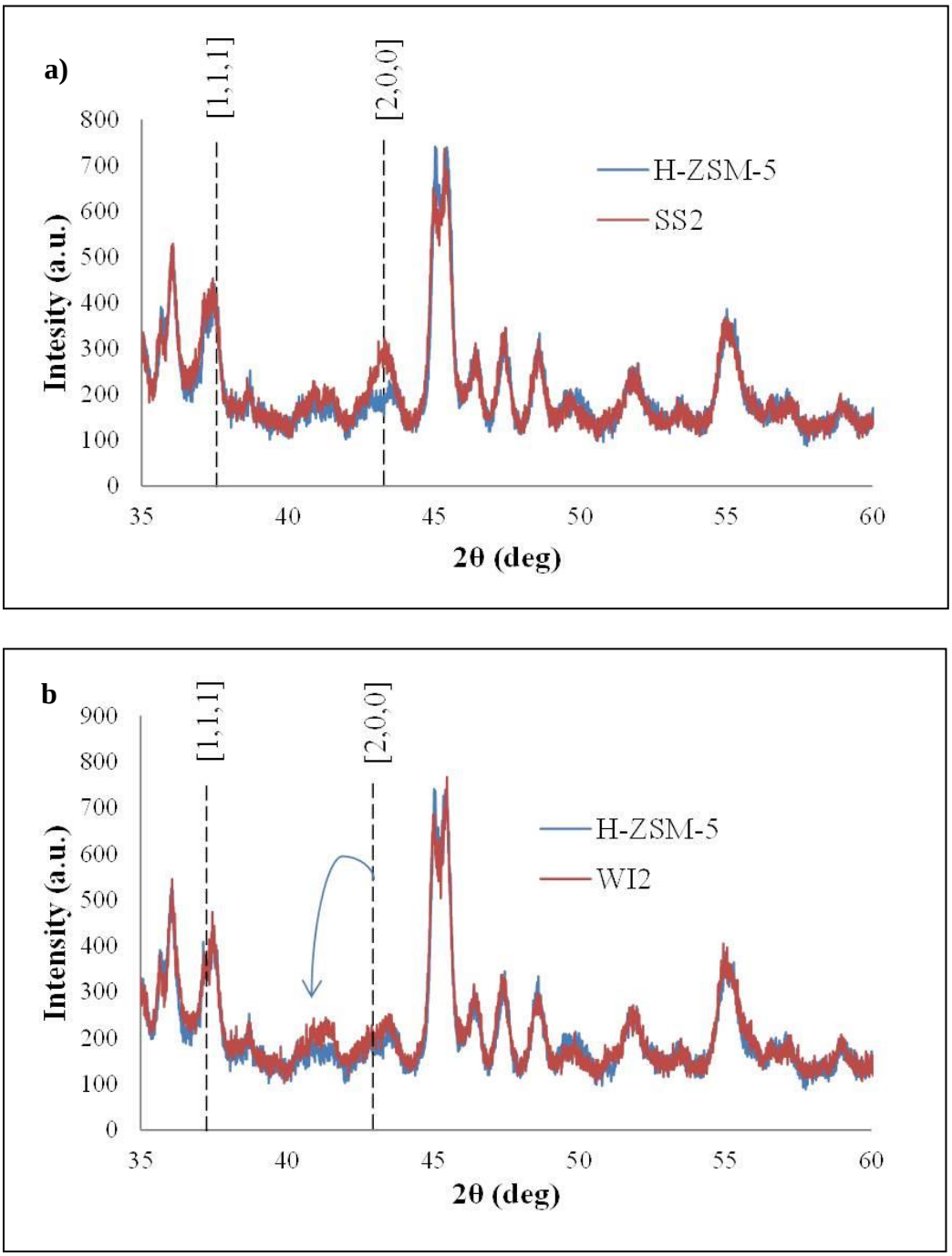

Figure 3.6 Comparison of XRD patterns of (a) H-ZSM-5 and SS2 catalyst and (b) H-ZSM-5 and WI2 catalyst.

Additionally, simulated XRD patterns were obtained in order to more accurately interpret the experimental XRD patterns obtained from the samples. The XRD simulation of the ZSM-5 zeolite pattern was obtained using the ZSM-5 zeolite lattice parameters and compared to the experimental results (Figure 3.7), showing good pattern overlap. However, it is seen that the relative intensity of some peaks in the diffractograms (i.e. 2θ = 36 and 45 deg) do not match the XRD simulation. This variation in the relative peak intensity is described by McCusker L. B. et al. (1999) as arising from several factors, including impurities in the sample, interference with the sample holder, or the presence of a second phase. In our case, we determined that this variation in the relative intensities is due to a systematic error generated by the user of the diffractometer while placing the sample into the holder.

As well, simulated XRD patterns for NiO were also obtained (Figure 3.8). Those diffractograms show two peaks, corresponding to the [111] and [200] crystal planes located at the positions described above (Section 3.3.2.1). The NiO peaks decreased in size when the crystal domain size was reduced, as expected from the Scherrer equation (3.2); this phenomenon is better explained elsewhere (Cullity et al., 2001). The peaks fully overlap when the crystal domain size was set at 1 nm. This indicates that the minimal crystal domain size that is detectable under these conditions is 2 nm.

$$\boldsymbol{\tau} = \frac{\boldsymbol{K\lambda}}{\boldsymbol{\beta cos(\theta)}} \tag{3.2}$$

where $\boldsymbol{\tau}$ is the mean size of the crystal domain, $\boldsymbol{K}$ the shape factor (usually 0.9), $\boldsymbol{\lambda}$ the X-ray wavelength, $\boldsymbol{\beta}$ the broadening at half of the maximum intensity (FWHM) of the peak, and $\boldsymbol{\theta}$ is the Bragg angle.

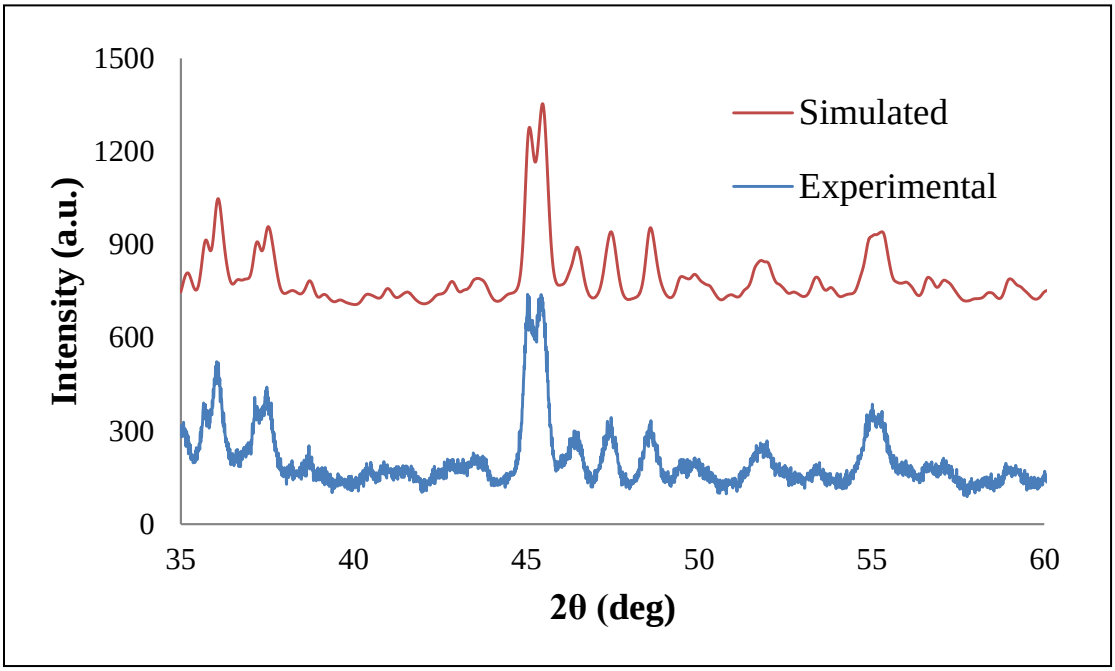

Figure 3.7 Comparison of experimental XRD patterns of H-ZSM-5 as made with the simulated patterns for ZSM-5.

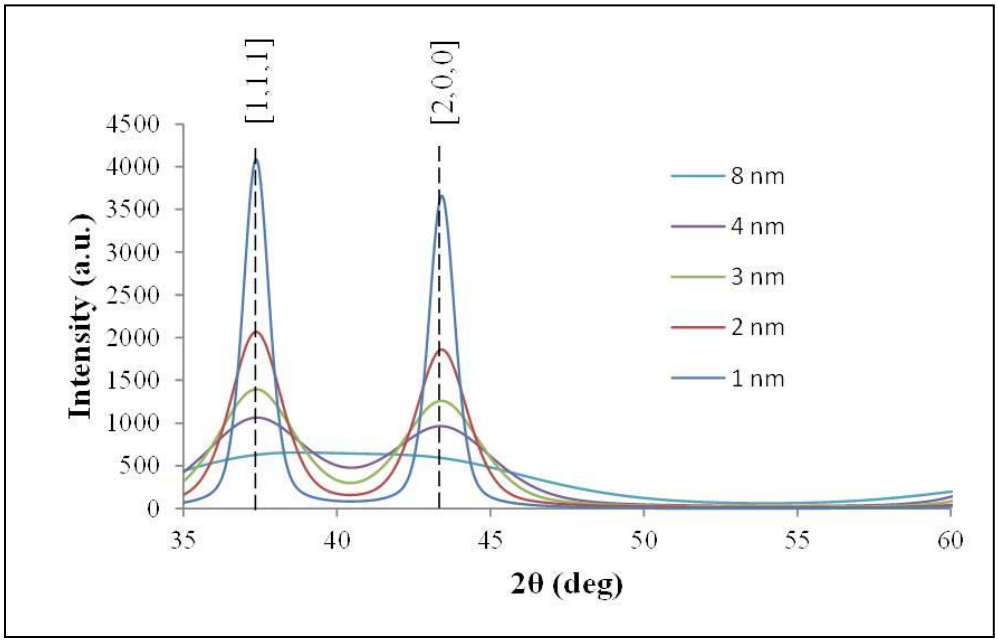

Figure 3.8 Simulated XRD patterns for NiO having different crystal domain sizes of 1-8 nm.

Also, simulated XRD diffractograms for ZSM-5 and ZSM-5 + NiO (using a crystal domain size of 8 nm for NiO) were plotted, as shown in Figure 3.9a. Note that, 2.5 % NiO + 97.5 % ZSM-5 in the simulations corresponds to 2% Ni/H-ZSM-5 in the real sample. Therefore, the ZSM-5 + NiO simulated XRD pattern gave a decent replica of the behaviour seen in the experiment. There is also a reasonable correspondence in the XRD pattern when a NiO crystal domain of 4 nm was used in the simulation (Figure 3.9b) when comparing with the W12 catalyst (Figure 3.6a). Note that the peak at 43.30 degrees is observed much more clearly in samples prepared by SS than by WI. This is correlated with the different crystal domain sizes of the NiO particles present in both catalysts, as predicted by equation (3.2).

Figure 3.10 shows the simulated XRD patterns for the ZSM-5 zeolite and the ZSM-5 + NiO catalyst with a crystal domain size of 1 nm, with very little difference seen between them. So far, the best approximation to the XRD patterns of samples prepared by SS is obtained by using a NiO crystal domain size of 8 nm, while for samples prepared by WI, the best approximation is when a 4 nm or smaller crystal domain size is used. Note that, while decreasing the NiO crystal domain size in the simulated XRD generates broadened NiO peaks, a shift in angles may appear, as was seen in Figure 3.6b. This shows that samples prepared by SS either contain NiO that is more crystalline than in WI, or that samples prepared by SS are less dispersed, generating NiO larger particles.

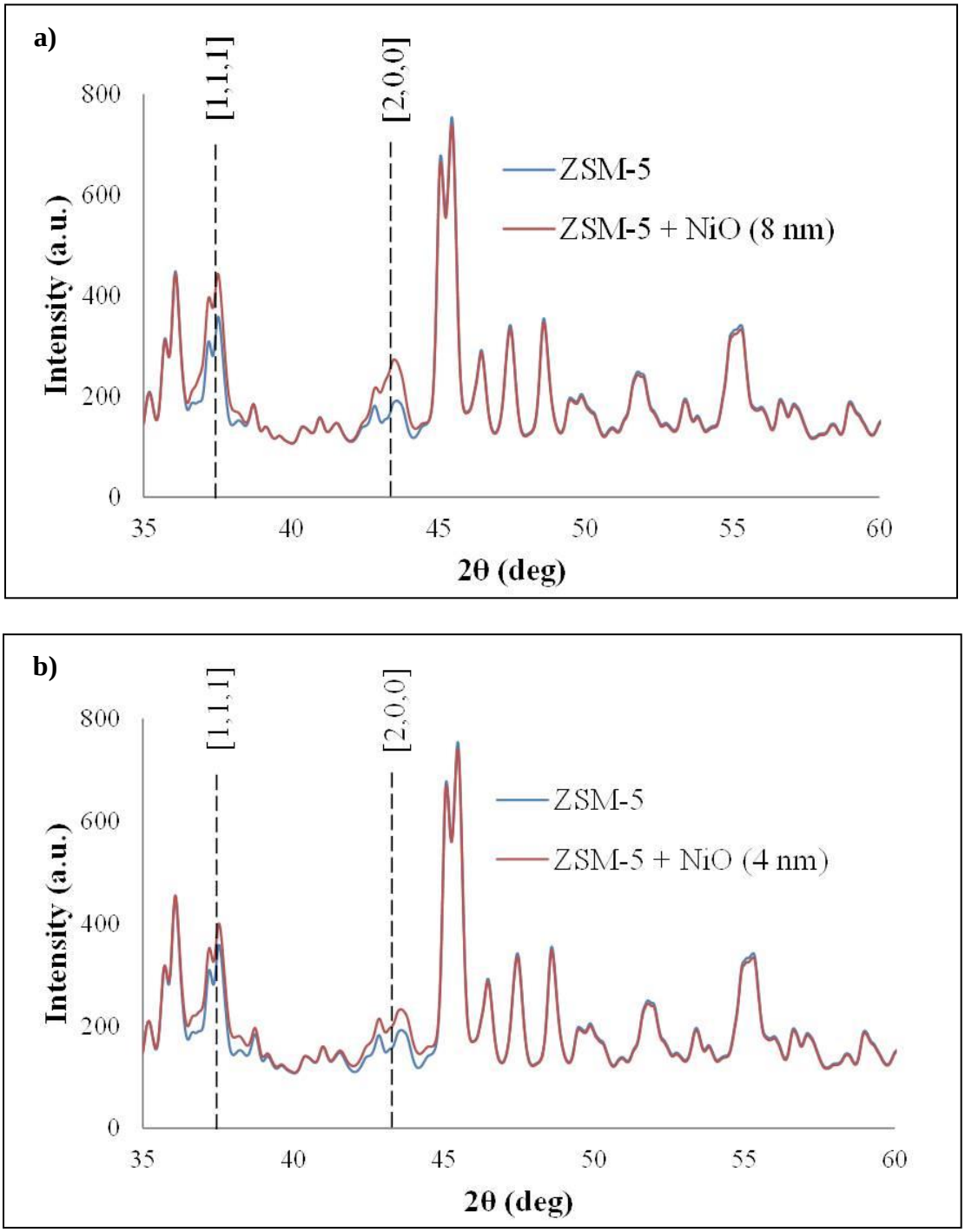

Figure 3.9 Comparison of simulated XRD patterns of ZSM-5 zeolite and (a) ZSM-5 + 2.5 % NiO (with a crystal domain size of 8 nm), and (b) ZSM-5 + 2.5 % NiO (with a crystal domain size of 4 nm).

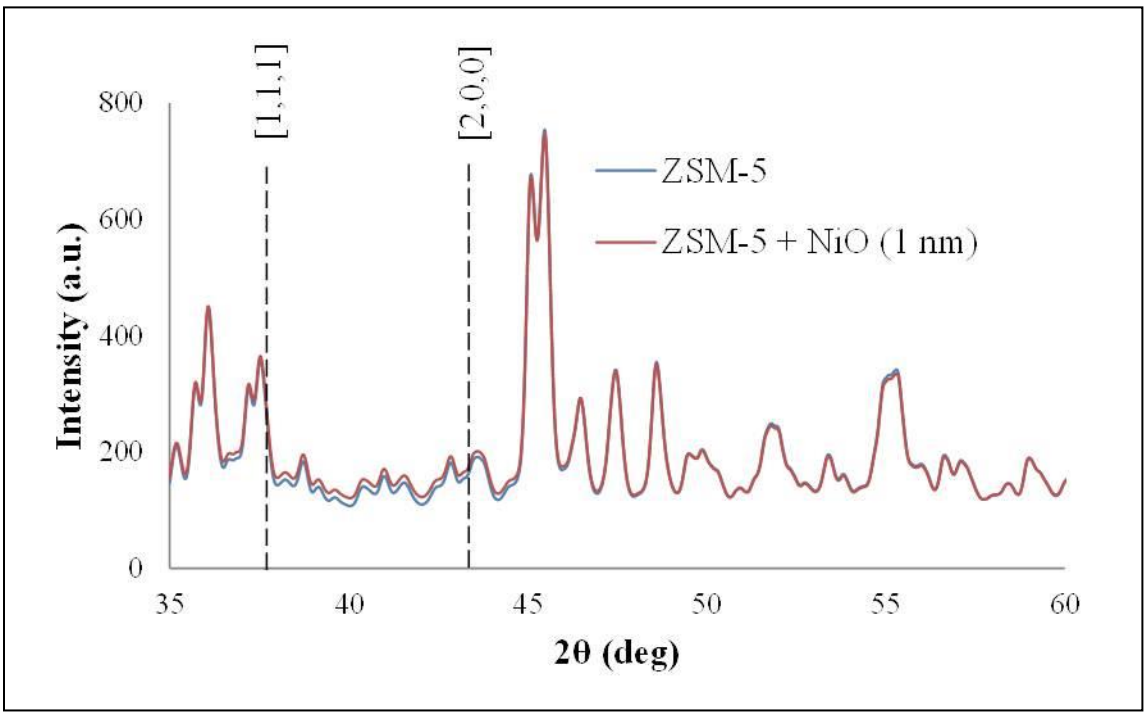

Figure 3.10 Comparison of simulated XRD pattern of ZSM-5 zeolite and ZSM-5 + 2.5 % NiO (with a crystal domain size of 1 nm).

Finally, Table 3.5 shows the crystal domain sizes for the different catalysts. For the catalysts prepared by SS, while increasing the Ni loading above 1.3 wt. %, the crystal domain size increased to higher values. This could be due to the formation of large NiO crystals on the support. However, as 0.5 wt. % of Ni was the least amount of Ni used in this work, a NiO peak could still be seen in the diffractogram. On the other hand, as it was not possible to see any differences in the XRD patters of the support compared to the WI Ni-loaded catalysts (WI0.5 and WI0.8), it can be concluded that WI has a better dispersion of the NiO particles Moreover, XRD showed smaller crystal domain sizes when 2 wt. %. Ni was present in the WI catalysts vs. the analogous SS catalysts. From these results, it can be concluded that the WI synthesis method result in better NiO dispersion than SS.

Table 3.5 Crystal domain sizes of the catalysts estimated from comparing to the simulations

Catalysts	Cristal domain size (nm)	Catalysts	Cristal domain size (nm)
SS0.5	4	WI0.5	Undetectable
SS0.8	4	WI0.8	Undetectable
SS1	4	WI1	4
SS1.3	4	WI1.3	4
SS2	8	WI2	4
SS3	10	WI3	8

3.3.3 Temperature Programed Reduction (TPR)

TPR spectra of some of the SS catalysts are shown in Figure 3.11. These profiles all reveal a common reduction temperature of 380 °C, which has been reported to reflect NiO reduction (Kubelcova et al., 1993). However, with increasing Ni loading, it is more difficult to reduce the catalyst, as seen by the decrease in the intensity of the peak at 380 °C and the appearance of a second peak at 500 °C (and perhaps a few other features at still higher temperatures), observed for catalysts with > 1% Ni content. However, the two peaks are the most prominent features present in the profiles. The presence of the second (and potentially several more) peaks at higher temperatures indicates that Ni is harder to reduce in these samples, suggested by some authors to indicate the presence of Ni-support interactions (Kubelkova et al., 1993; Hoang et al., 1994; Masalska, 2005; Maia et al., 2010; Vitale et al. 2013). This profile for SS2, with its two

prominent peaks (Figure 3.11), is common for all of the WI catalysts under study here (Figure 3.12), where a first peak appears at 380 °C and a second at 600 °C.

The appearance of other peaks at higher temperatures in the TPR profile for the catalysts prepared by SS and WI can be explained as follows:

- The NiO particles could have a strong interaction with the support (as discussed in Section 3.3.4). The sites of interaction on the zeolite surface could be octahedral Al Bronsted acid sites, or silanol groups (Vitale et al., 2013). Consequently, it would be more difficult to reduce these Ni particles vs. Ni in sites where no or only minor interactions with the support exist. Evidence for interactions between the NiO particles and the support will be shown using diffuse reflectance infra-red Fourier transform spectroscopy in Section 3.3.4.
- The NiO particles may be distributed in more than one size (discussed in Section 3.3.2.2). Thus, larger NiO particles could be blocking pore entrances, leaving smaller NiO particles trapped in the sealed pore. Therefore, more energy may be needed to perform the reduction of the NiO (see reduction mechanism in Section 2.4). These trapped NiO particles would then be more difficult to reduce, requiring a higher temperature. If this is the case, it is important to note that large particles blocking the pores would be present in only small quantities, because XRD did not detect any large NiO particles (Section 3.3.2.2). The presence of more than one size of NiO particles is confirmed in Section 3.3.5.1, using low pressure gas sorption methods.

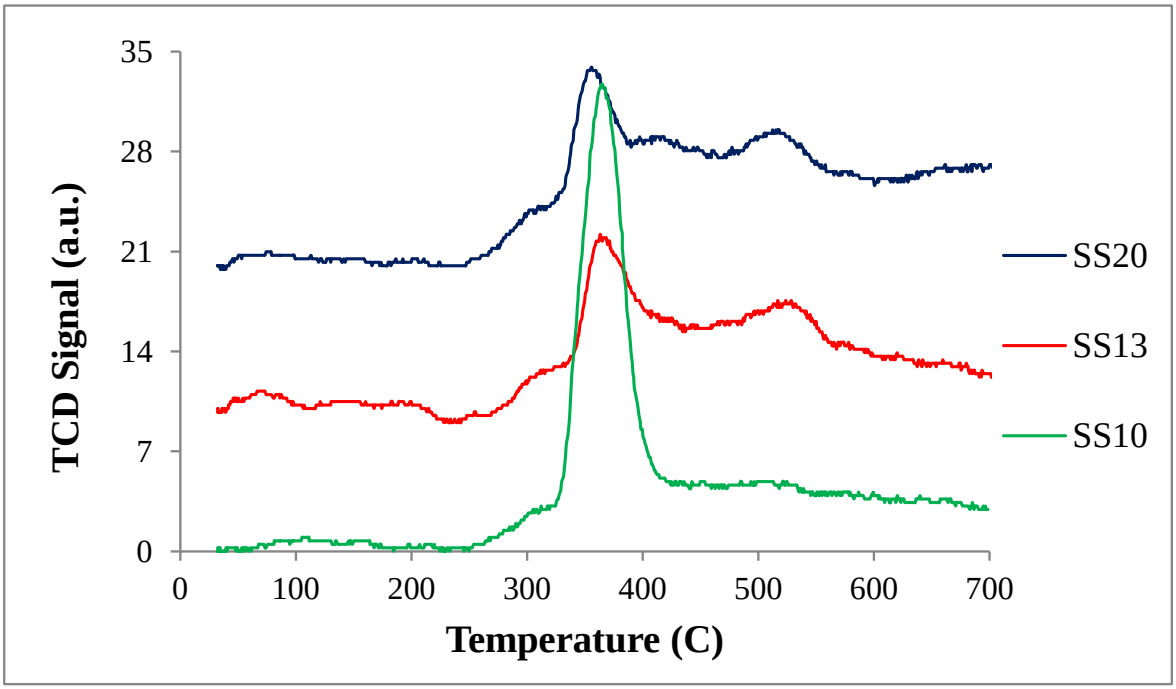

Figure 3.11 TPR profiles of Ni/H-ZSM-5 catalysts prepared by SS. Heating ramp: 10 °C/min, gas flow: 15 cc/min 10% H_2 in Ar, sample mass: 1 mg.

A comparison of the TPR profiles of the catalysts containing 1 wt. % Ni, prepared by the two metal incorporation methods, SS and WI, is shown in Figure 3.13. The main difference is that, for WI, the higher temperature peak moves to still higher temperatures with higher Ni loading. Thus, the conclusions reached from simulated XRD (Section 3.3.2.2) and TPR agree with the data obtained for catalysts prepared by SS, which contain larger NiO particles, compared to the catalysts prepared by WI.

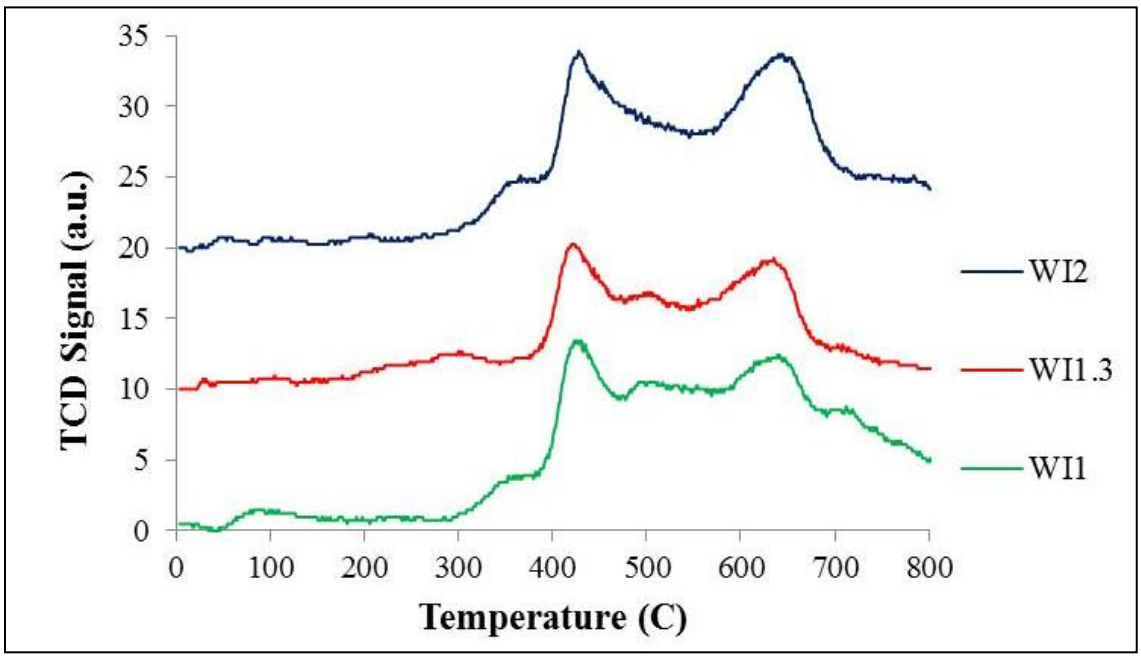

Figure 3.12 TPR profiles of Ni/H-ZSM-5 catalysts prepared by WI. Heating ramp: 10 °C/min, gas flow: 15 cc/min 10% H_2 in Ar, sample mass: 1 mg.

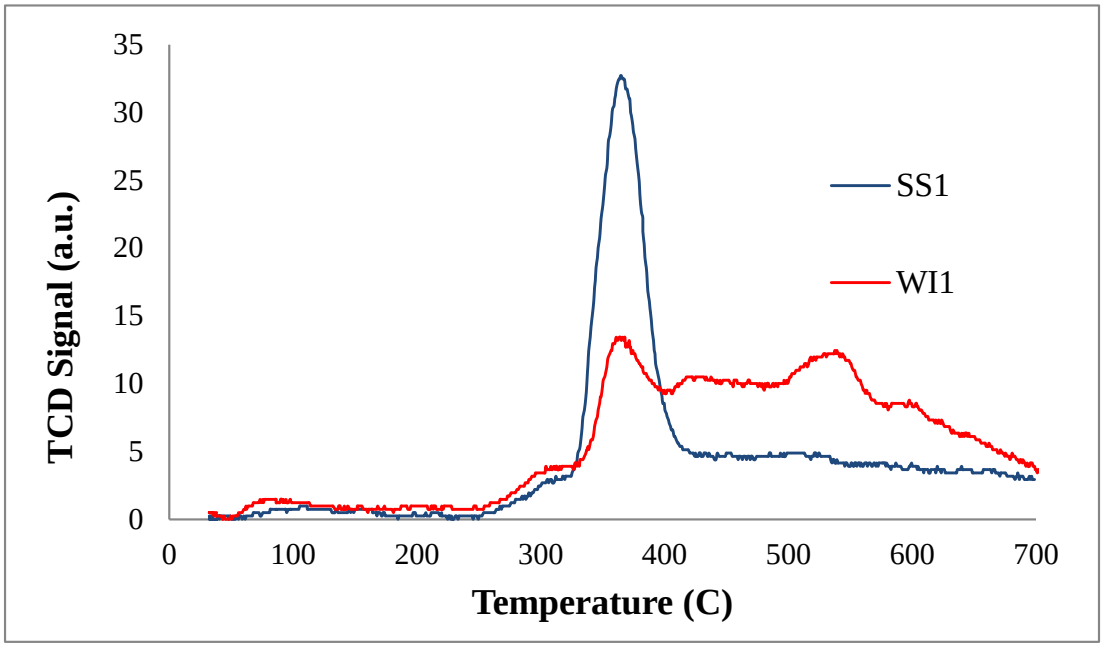

Figure 3.13 TPR profile for SS and WI Ni/H-ZSM-5 catalysts with 1 wt. % Ni. Heating ramp: 10 °C/min, gas flow: 15 cc/min 10% H_2 in Ar, sample mass: 1 mg.

Quantification of the area under the peak in Fig. 3.13 was done by using a calibration curve available with the TPR apparatus used in this study. As expected from the TPR profile shapes, a higher H_2 consumption was obtained than expected from this calculation, since the profiles for each catalyst are showing H_2 consumption at high temperatures (> 500 °C) when Ni is expected to already be in the reduced state. From this calibration curve, it was seen that the area under the peak is equivalent to ca. twice the H_2 that would be required to reduce all of the NiO present in the catalysts to Ni^0. In order to correct for this, a large number of samples would have to be be TPR-analyzed at constant temperatures; however, there was insufficient time available in this project to accomplish this.

3.3.4 Diffusive Reflectance Infrared Fourier Transform Spectroscopy (DRIFTS)

In-situ IR spectroscopy studies, with temperature variation, were performed on the support materials and all of the Ni-containing catalysts. The first experiment involved collecting a spectrum for each sample at RT within the *in-situ* cell (Section 3.2.3.4) under a flow of N_2. Samples were heated to 400 °C for 2 h, cooled to RT, and then another spectrum was collected. As expected, the water band reappeared, indicating that this is a reversible process in which water is adsorbed on the zeolite due to its silanols present on the surface (Mahmoud, 2006), even under a N_2 flow (99.99% purity). This reaffirms that the ZSM-5 zeolite adsorbs water easily from the atmosphere, as seen in previous studies (Kenigens et al., 1983).

In the IR spectra of ZSM-5 (Figure 3.14a), the bands at 3724 and 3612 cm-1 correspond to terminal silanols (Si-OH) and bridged (Si-(OH)-Al) groups, respectively. These bands are well defined when the zeolite is dehydrated. Under standard conditions, the IR water band is broad, appearing from 2200 to 3800 cm^{-1}, thus overlapping and obscuring the bands corresponding to the terminal silanols and the (Si-(OH)-Al) groups. Therefore, IR spectra were collected at

temperatures higher than RT in order to remove the water band, i.e., to 90, 200, and 400 °C for the zeolite (Figure 3.14a), and to 120, 200, and 400 °C for the SS1 (Figure 3.14b) and WI1 (Figure 3.14c) catalysts.

A decrease in the water band is observed at a temperature of 120 °C (Figure 3.14a and Figure 3.14b). As the temperature was increased to 400 °C, the spectra showed two bands, corresponding to the terminal silanol Si-OH (3745 cm^{-1}) and bridged Si-(OH)-Al groups at (3612 cm^{-1}). These two bands were observed for H-ZSM-5 and also for the catalysts prepared by SS and WI (Figure 3.14a-c).

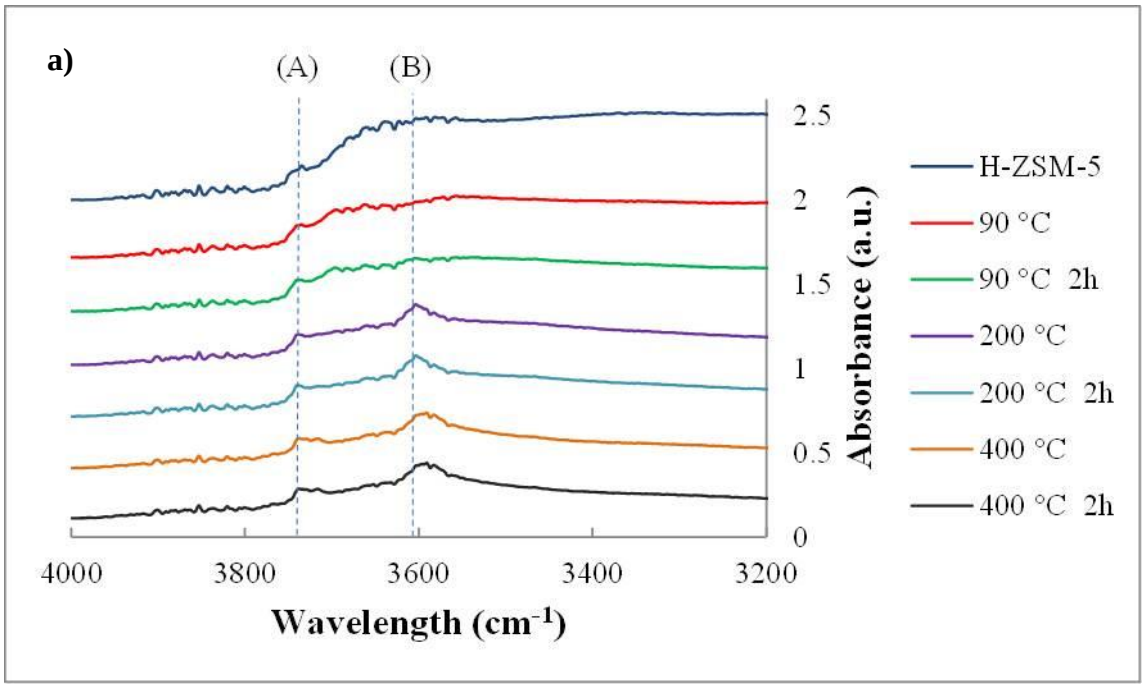

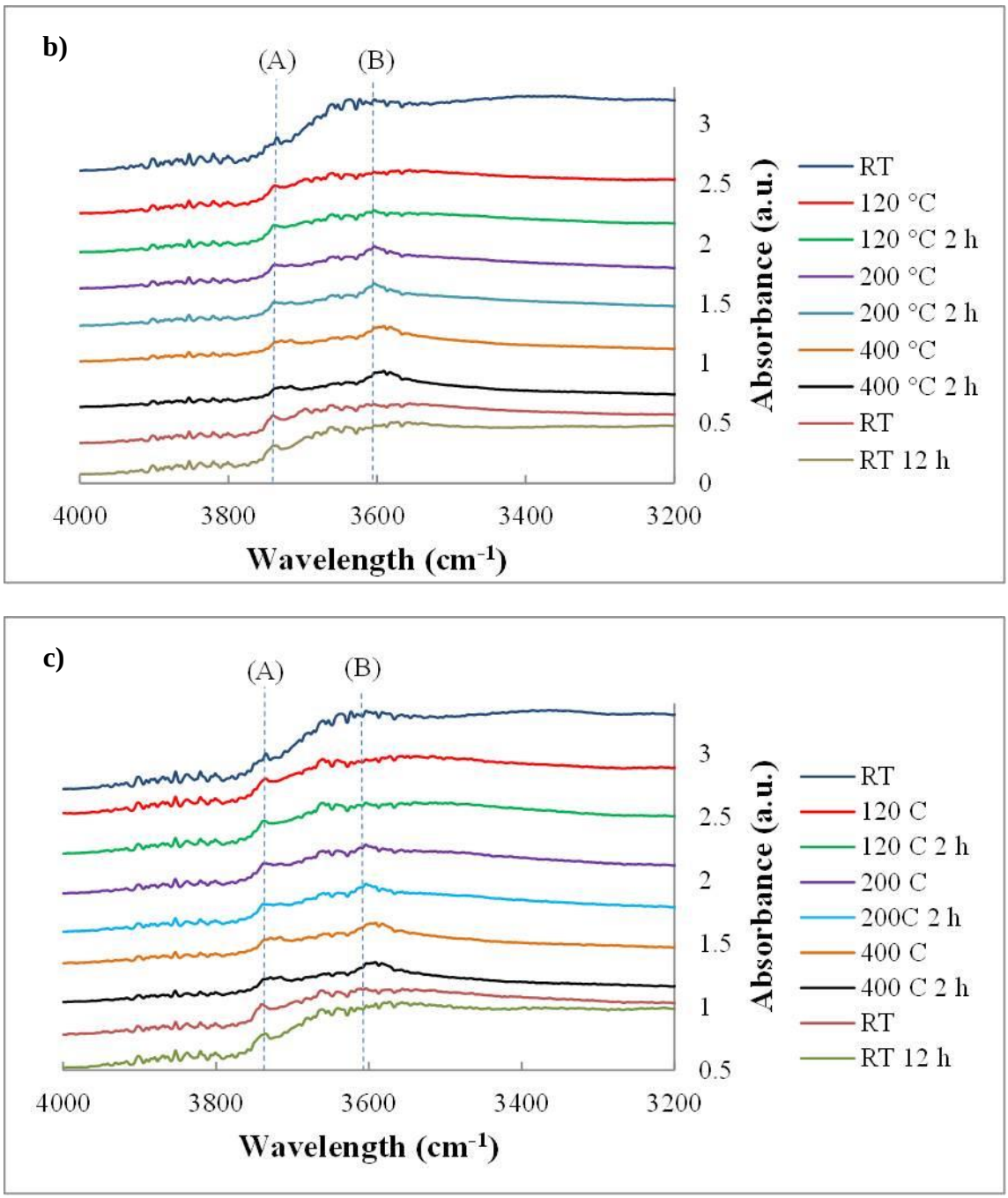

Figure 3.14 Temperature variation of *in-situ* IR spectra of a) H-ZSM-5, b) SS1, and c) WI1 catalyst. Vertical dashed lines identify the position of features corresponding to: (A) terminal silanols Si-OH at 3724 cm^{-1} and (B) bridged Si-(OH)-Al groups at 3612 cm^{-1}.

The IR spectra of the catalysts showed that the bands for the silanol groups decreased in size when the Ni loading was increased (see Figure 3.15) for both metal incorporation methods. The magnitude of the IR signal was estimated by integrating the area under the 3612 cm^{-1} band. This decrease could be due to interactions of Ni with the Bronsted acid site. Previous authors have observed a decrease of more than 50% in the acidic -OH band in the IR spectrum when 1% Pd was incorporated into H-ZSM-5 (Karge et al., 1992). However, a detailed explanation of this phenomenon or the relevant mechanism has not been reported as yet.

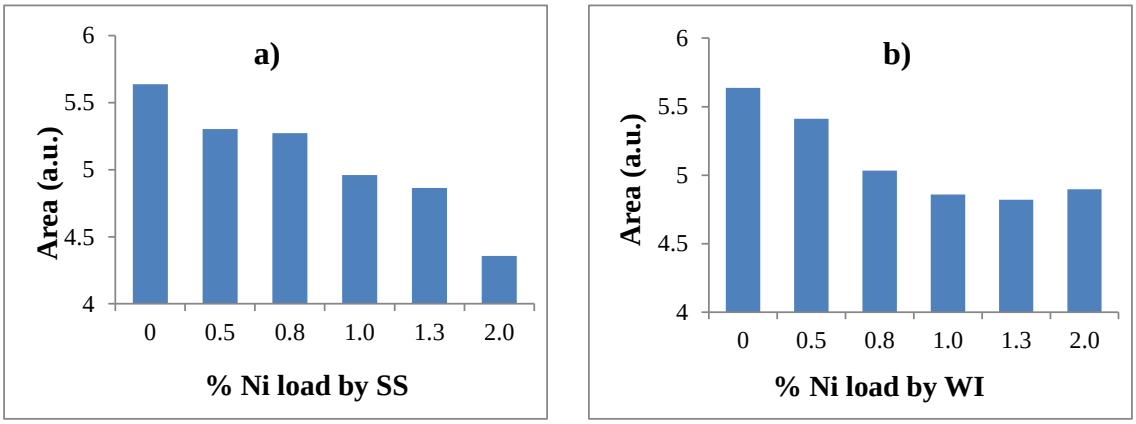

Figure 3.15 Integrated area under the IR band centered at 3590 cm-1 for SS and WI catalysts showed in Figure 3.14a and Figure 3.14b, respectively.

In our case, Ni seems to prefer the Si-(OH)-Al bridging site over any other site on the support surface. A reasonable mechanism for the Ni to be attached to the support is that, when Ni^{2+} bonds with the Si-(OH)-Al bridge, more NiO will attach to this already attached Ni, forming a particle. This behaviour is more likely to occur on siliceous aluminate supports than on the alumina-based supports (Molina et al., 1999). However, results presented by other authors (Poncelet et al., 2005) have presented a mechanism of how Ni interacts with an Al-based support and how it depends directly on the calcination temperature. In our case, Ni likely attaches to the

tetrahedral and octahedral Al sites of the support. Thus, Ni exhibits a range of reduction temperatures, i.e., around 380 and 500 °C for the SS and 380 and 600 °C for the WI catalysts (Section 3.3.3). This explanation matches other hypotheses given elsewhere, obtained from CO-IR spectroscopy and supported by H_2 chemisorption and XPS analysis (Poncelet et al., 2005).

3.3.5 Surface Area and Pore Size Distribution by Low Pressure Gas Sorption

3.3.5.1 Low Pressure N_2 Adsorption Analysis Using BET Method

The specific surface area of the support and the catalysts was obtained by BET, with the results for the H-ZSM-5 and the catalysts prepared by the SS and WI methods presented in Table 3.6. In order to remove impurities adsorbed on the samples, a pre-treatment was performed, consisting of heating the sample to 150 °C for periods of 4 - 6 h in an Ar atmosphere. The results (Table 3.6) show average values of 330 m^2/g for H-ZSM-5, while the specific surface area is 265 and 255 m^2/g for the SS3 and WI3 catalysts, respectively. Note that the specific surface area is another parameter that changes as the methodology employed for the zeolite synthesis was changed, as discussed previously in this chapter (Section 3.3.1).

Figure 3.16 shows the raw data for the H-ZSM-5 zeolite, with the hysteresis confirming a mesoporous structure. As low pressure N_2 adsorption methods cannot detect microporosity, the zeolite may also contain some micropores, since the shape of the curve at low pressures indicates Type I character, consistent with the presence of micropores. A complete isotherm is shown at the bottom right of Figure 3.16 in order to demonstrate that, at low partial pressures, the isotherm is a typical Type I, as seen by the almost vertical rise seen initially at very low pressures. In the remaining N_2 adsorption isotherm data shown in this chapter, the low pressure data are not included and only the hysteresis loop is shown.

Table 3.6 Specific Surface Area of H-ZSM-5, SS and WI catalysts.

Sample	Specific Surface Area (m^2/g) (BET)	Sample	Specific Surface Area (m^2/g) (BET)
H-ZSM-5	330	----	----
SS0.5	300	WI0.5	325
SS0.8	290	WI0.8	340
SS1	295	WI1	315
SS1.3	295	WI1.3	300
SS2	280	WI2	275
SS3	265	WI3	255

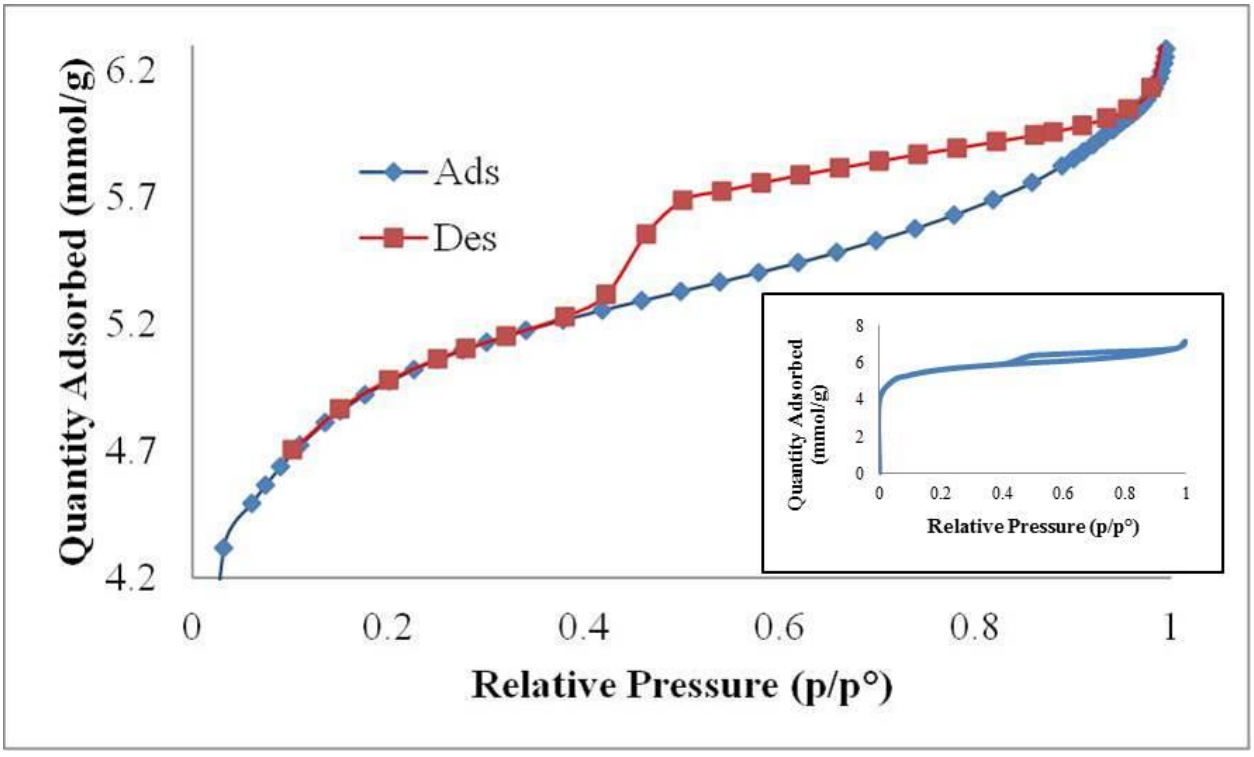

Figure 3.16 Low pressure N_2 adsorption/desorption isotherm of H-ZSM-5. Blue line: Adsorption branch and Red line: desorption branch.

Figure 3.17 shows the low pressure N_2 adsorption isotherm for the SS1 and WI1 catalysts. SS1 shows a lower adsorption capacity than does WI1, consistent with its higher surface area (Table 3.6). However, the hysteresis loop for the H-ZSM-5 zeolite and both catalysts, SS1 and WI1 (Figure 3.16 and Figure 3.17), begins and ends at more or less the same partial pressure and has the same shape, indicating a similar range of pore diameters and a similar pore geometry. The isotherm of the Ni-containing H-ZSM-5 (Figure 3.17) matches that of the H-ZSM-5 (Figure 3.16), indicating that the pore geometry does not change significantly after Ni incorporation; however, it changes the pore volume and specific surface area. These results lead to the conclusion that the pores between particles are getting larger when more Ni is incorporated into the support, increasing their volume and therefore reducing the specific surface area of the catalysts.

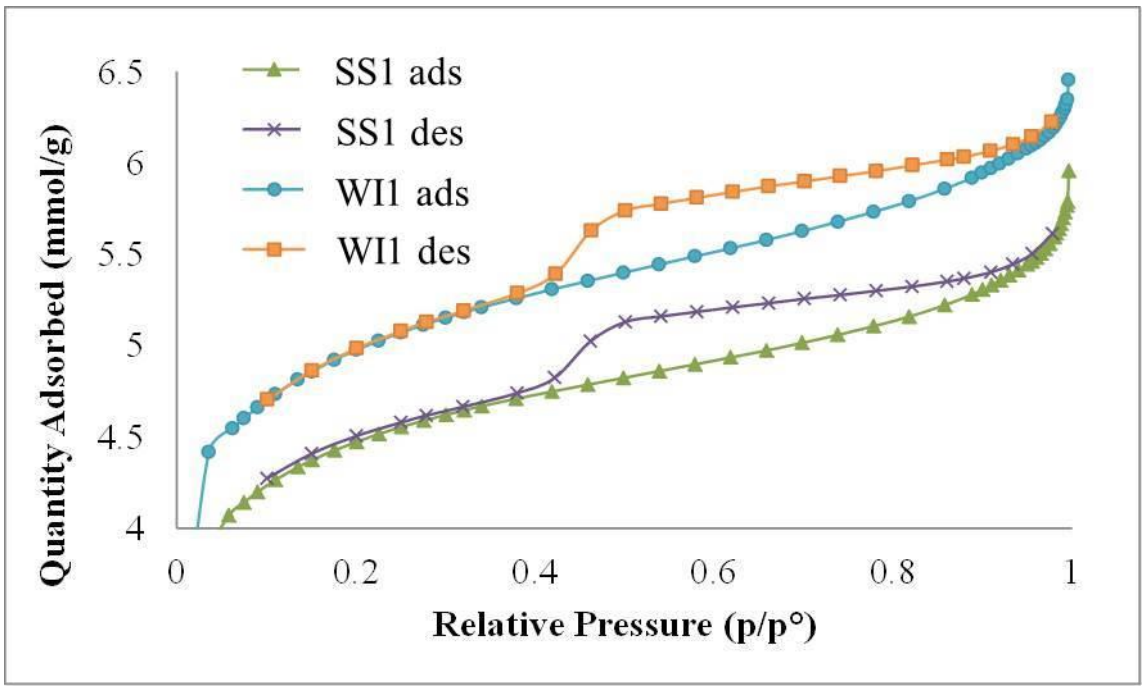

Figure 3.17 Low pressure N_2 adsorption/desorption isotherm of SS1 and WI1 catalysts. Blue dots: SS1 adsorption branch, orange squares: SS1 desorption branch, green triangles: WI adsorption branch, and purple x's: WI desorption branch.

This decrease in the specific surface area when the Ni content was increased (Table 3.6) was seen in previous studies in our group (Molero et al., 2009). The micropore surface area decrease can be attributed to NiO formation after the decomposition of the Ni salt. As a result, NiO may be blocking the micropores of the zeolite. Thus, these NiO particles may be < 0.7 nm in diameter, which is the approximate average size of the ZSM-5 zeolite pores. While these particles may block the channels and lower the surface area, they are not large enough or plentiful enough to be detected by XRD or SEM.

3.3.5.2 Low Pressure N_2 Adsorption Analysis Using BJH Theory

Figure 3.18a shows the pore size distribution of the H-ZSM-5 and the SS catalysts obtained by applying the BJH theory to the gas sorption data. This distribution verifies that the diameter of the pores is in the mesopore range (> 2 nm and < 60 nm), as shown in Table 3.7. The specific pore volume increased, from 0.069 cm^3/g for the H-ZSM-5 to 0.163 and 0.108 cm^3/g for the SS3 and WI3 catalysts, respectively. An increase in total pore volume is observed when the pores have larger diameters. Almost no pores in the macropore range (> 60 nm) are seen and when approaching the micropore range (< 2 nm), the plot starts increasing again (Figure 3.18a), suggesting that there is some pore volume in the micropore range. Notably, there is an increase in total pore volume (decrease in specific surface area) as more Ni is incorporated into the catalysts.

Table 3.7 Pore volume of H-ZSM-5, SS and WI catalysts.

Sample	**Pore Volume (cm^3/g) (BJH ads)**	**Sample**	**Pore Volume (cm^3/g) (BJH ads)**
H-ZSM-5	0.07	-----	------
SS0.5	0.09	WI0.5	0.08
SS0.8	0.08	WI0.8	0.09
SS1	0.10	WI1	0.09
SS1.3	0.11	WI1.3	0.10
SS2	0.11	WI2	0.10
SS3	0.16	WI3	0.11

The same behaviour is observed for the catalysts prepared by WI (Figure 3.18b). However, the total pore volume in the WI catalysts is smaller (0.005 – 0.008 $cm^3/gÅ$) than in the SS catalysts (0.007 – 0.012 $cm^3/gÅ$). At the same time, the zeolitic support has less pore volume

in the mesopore range (0.004 $cm^3/gÅ$). These results indicate the formation of multimodal particle sizes of NiO during Ni incorporation. This would be consistent with some pores being blocked by NiO particles, thus lowering the surface area of the support. This conclusion was discussed earlier (3.3.2.2) and in previous work (Molero et al., 2009).

Figure 3.19 shows the pore size distribution of the H-ZSM-5 support and the SS1 and WI1 catalysts, all obtained from the BJH analysis of the N_2 desorption branch. These pore size distributions are very similar to the ones obtained from the BJH adsorption model. While approaching the micropore range (< 2 nm), the pore volume begins to increase and, in the macropore range (> 60 nm), a plateau is seen. However, a prominent peak is also seen at 3.6 nm. This peak is given the label "artifact" in the BJH model (Janssen et al., 2002) and it is being widely discussed in the literature for several types of materials, such as zeolites (Janssen et al., 2002; Ravikovitch et al., 2001), coal (Clarkson et al., 1999), and tight gas (Clarkson et al. 2012). The "artifact" peak is seen only at low pressures and only during gas desorption. For materials having "ink-bottle" pore shapes with necks smaller than 4 nm, the N_2 that should have been released at a relative pressure of 0.45 P/P^0 is trapped and then released at lower relative pressures (Janssen et al., 2002). Thus, the BJH model considers the N_2 gas coming from these "ink-bottle" pores as originating from cylindrical pores with a smaller pore diameter, thus generating the artifact peak at 3.5 nm.

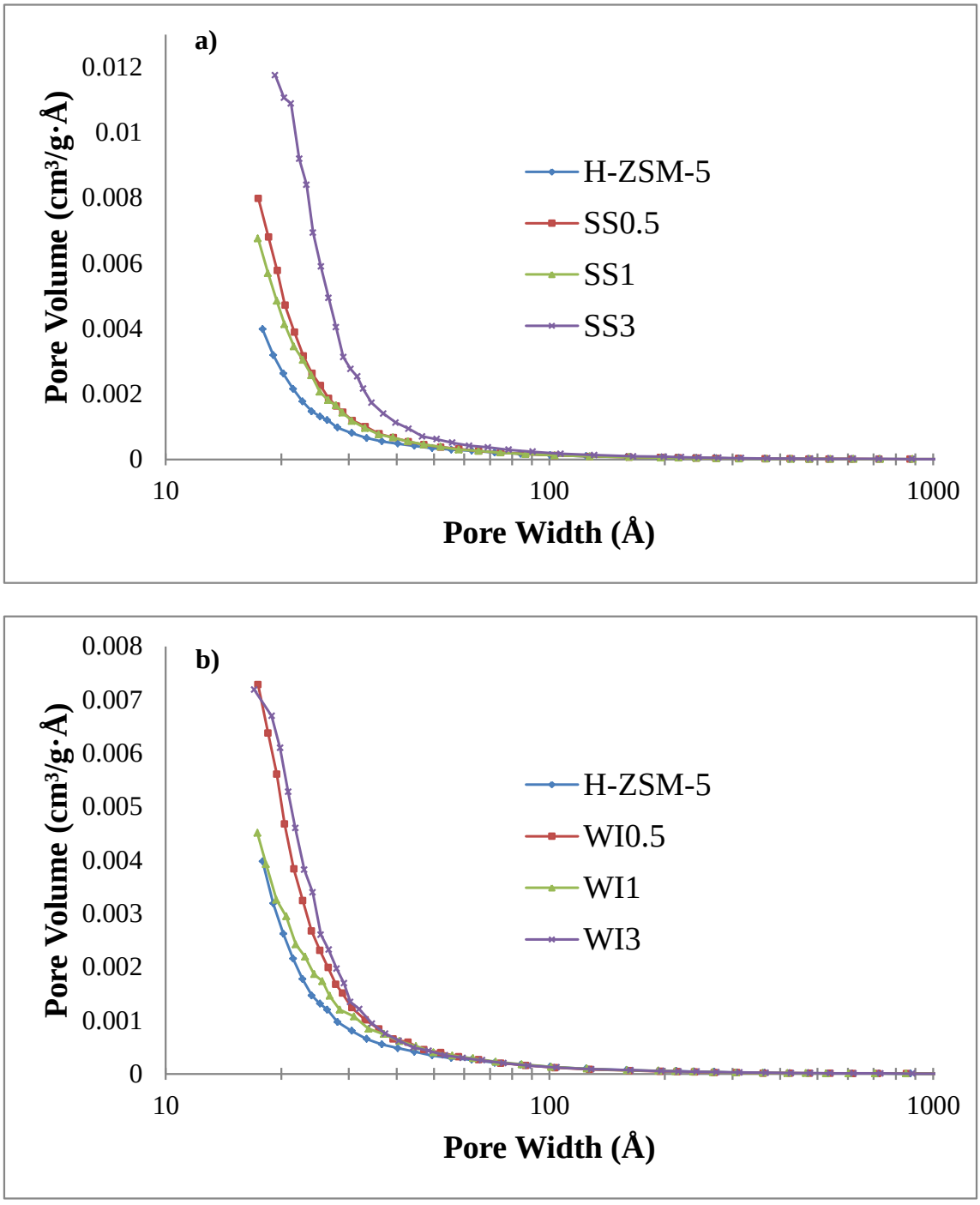

Figure 3.18 Pore size distribution of H-ZSM-5 and (a) SS and (b) WI catalysts using the BJH model on the adsorption branch.

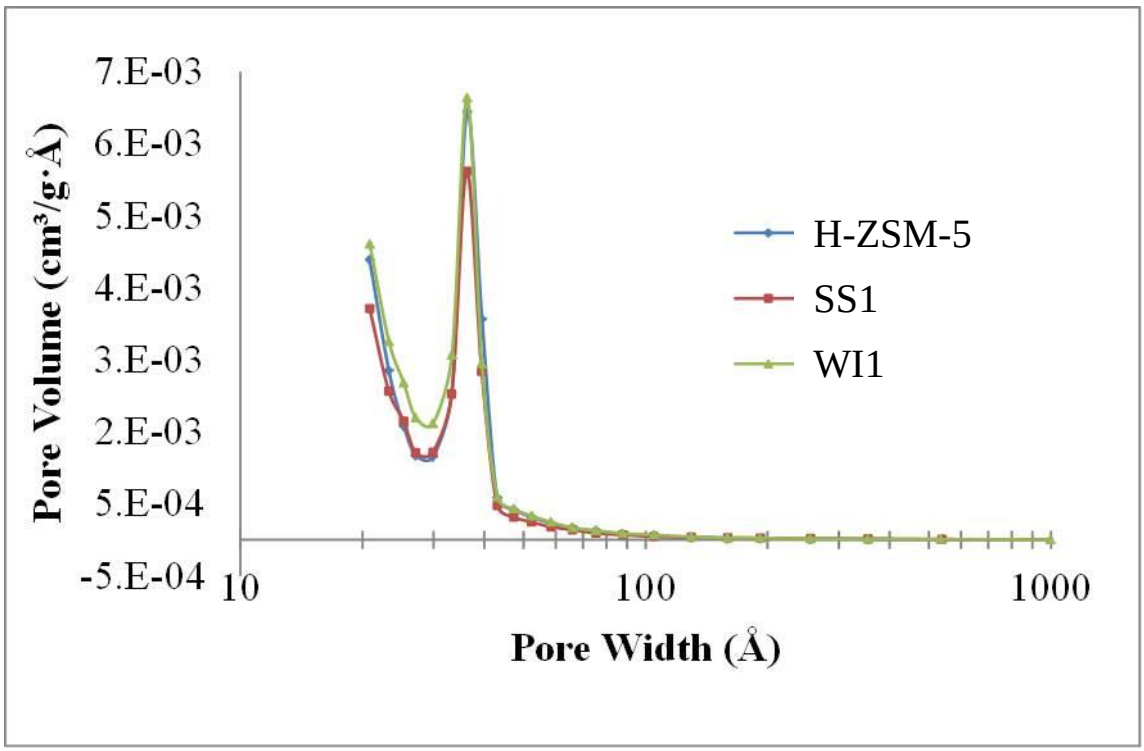

Figure 3.19 Pore size distribution of H-ZSM-5, SS1, and WI1 using the BJH model on the desorption branch.

A comparison of the pore size distributions of H-ZSM-5, obtained using the BJH model from the adsorption and desorption branch (Figure 3.20), shows very little difference between the two distributions. Excluding the artifact, likely generated from the model, the main difference between the two plots is that the pore volume obtained from the BJH desorption model is higher than from the BJH adsorption model when approaching the micropore range. However, it is important to notice that the model has used more data points in the adsorption than the desorption branch. Thus, the BJH model for the adsorption branch is more reliable.

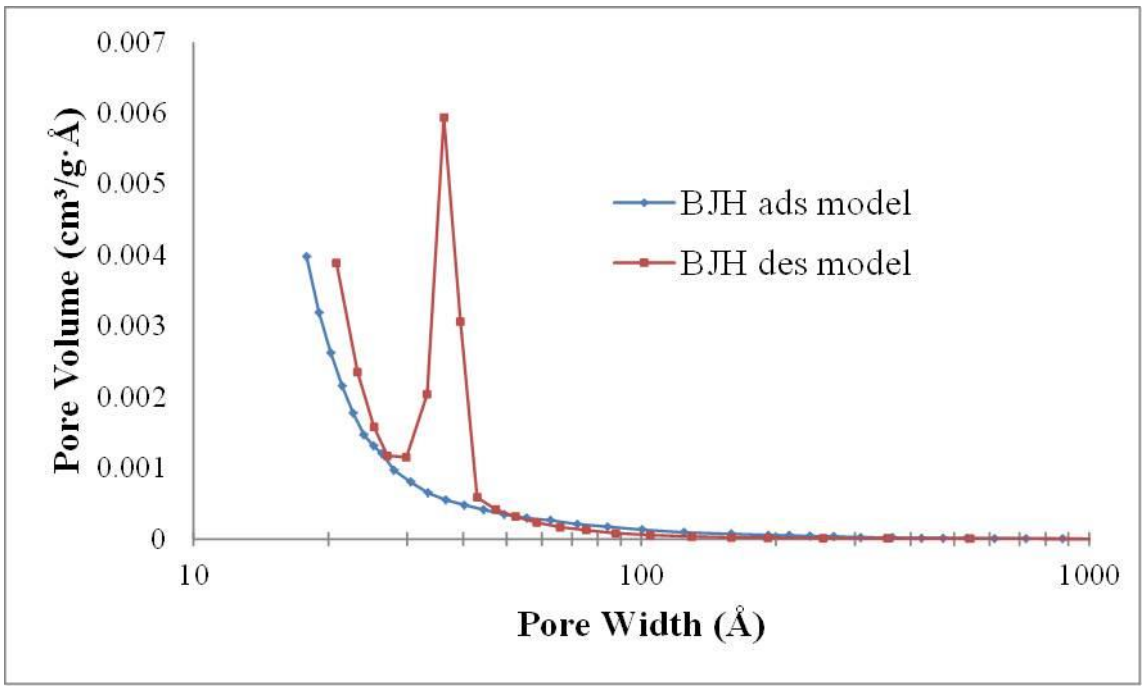

Figure 3.20 Comparison of the pore size distributions of the H-ZSM-5 zeolite (no Ni) using the BJH model on the adsorption and desorption branches.

Figure 3.21a and Figure 3.21b directly compare the pore size distributions of the SS and WI catalysts, respectively. For the WI catalysts, a decrease is observed in the artifact peak at 3.6 nm when the Ni loading increases, while for the SS catalysts, this is not seen. However, the artifact peak, appearing in the pore size distribution from the BJH desorption plots, suggests that only the pore size distribution obtained from the BJH adsorption branch should be used in the analysis of results.

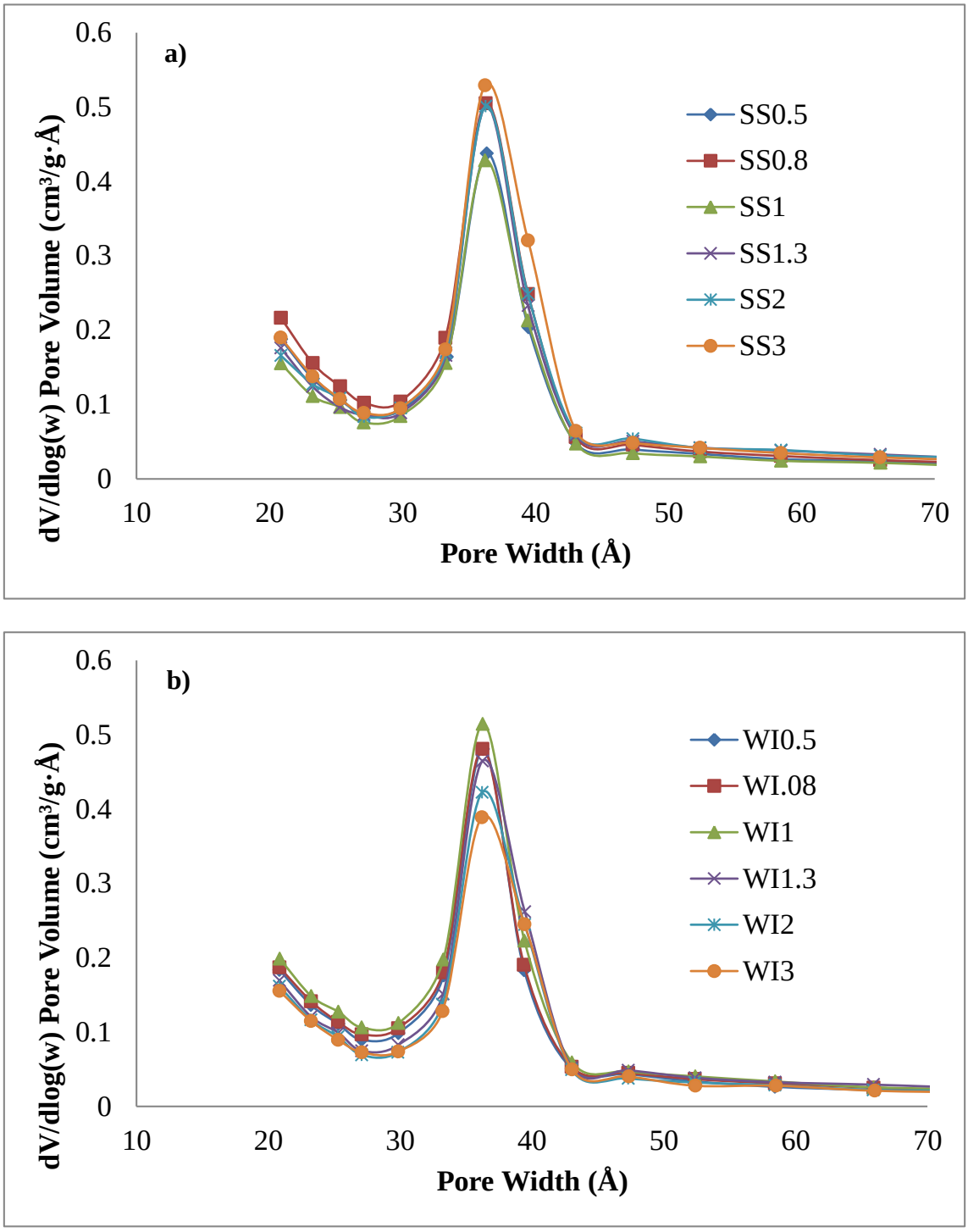

Figure 3.21 Pore size distribution of the a) SS and b) WI catalysts using the BJH model for the analysis of the N_2 desorption branches.

3.3.5.3 Low Pressure CO_2 Adsorption Analysis Using BET and Langmuir Adsorption Models

The specific surface area of the support and the catalysts was also obtained by BET and Langmuir theory using CO_2 adsorption isotherms (Table 3.8). The pre-treatment performed consisted of heating the sample to 150 °C overnight in an Ar atmosphere. Results shown in Table 3.8 indicate that the surface area in the micropore range decreases as the Ni loading increases. This effect is more pronounced for the WI catalysts than for the SS catalysts. This result reaffirms that Ni can more readily penetrate the micropores of the zeolite when the catalysts are prepared by the WI method than by the SS method.

Table 3.8 BET and Langmuir Specific Surface Area of H-ZSM-5, SS and WI catalysts.

Sample	BET Specific Surface Area (m^2/g cat)	Langmuir Specific Surface Area (m^2/g cat)
H-ZSM-5	270	279
SS0.5	273	282
SS1	271	279
SS3	254	263
WI0.5	265	274
WI1	254	263
WI3	233	240

Figure 3.22 is a display of the CO_2 adsorption isotherm for the H-ZSM-5, SS, and WI materials. Note that the shape of the isotherms for all of the samples is typical of a Type I isotherm (Langmuir isotherm), which is characteristic for samples containing micropores. As presented in the previous section, the thermal decomposition of the Ni salt likely lowers the surface area; therefore, less CO_2 adsorption is seen in catalysts having a higher Ni content. This effect is observed for both catalysts. However, the isotherm for the WI catalysts shows less CO_2

being adsorbed than for the SS catalysts when the Ni loading increases. This contradicts what was demonstrated from the N_2 adsorption isotherms, where the surface area decrease is more notable in the SS catalysts than in the WI catalysts. However, it can still be concluded (as discussed in Section 3.3.2.2) that larger Ni particles remain in the pores in the meso- and macrorange for catalysts prepared by the SS method.

The DFT model was also examined to obtain information about the pore size distribution of the Ni-zeolite catalysts (Figure 3.23). Little information could be obtained from this plot, since just a group of random peaks from 7 to 9 Å in size was observed for all of the samples. Also, a peak at 10.2 Å generated for one point in the plot is seen for some of the catalysts. The plots do not provide any information about pores larger than 11.5 Å in diameter and thus no correlation can be made between these results and the results obtained from the BJH model in the previous section. This may be because the ZSM-5 zeolite has a slightly elliptical pore shape (0.57 x 0.61 nm) (Weitkamp, 2000), while for the DFT analysis, slit-shaped pores were used. Similar results were obtained for the geological samples in Chapter 4. However, in that case, this was attributed to CO_2 swelling of the samples (Section 4.4.2.3.2), since for the geological samples, the isotherm shapes are not Type I.

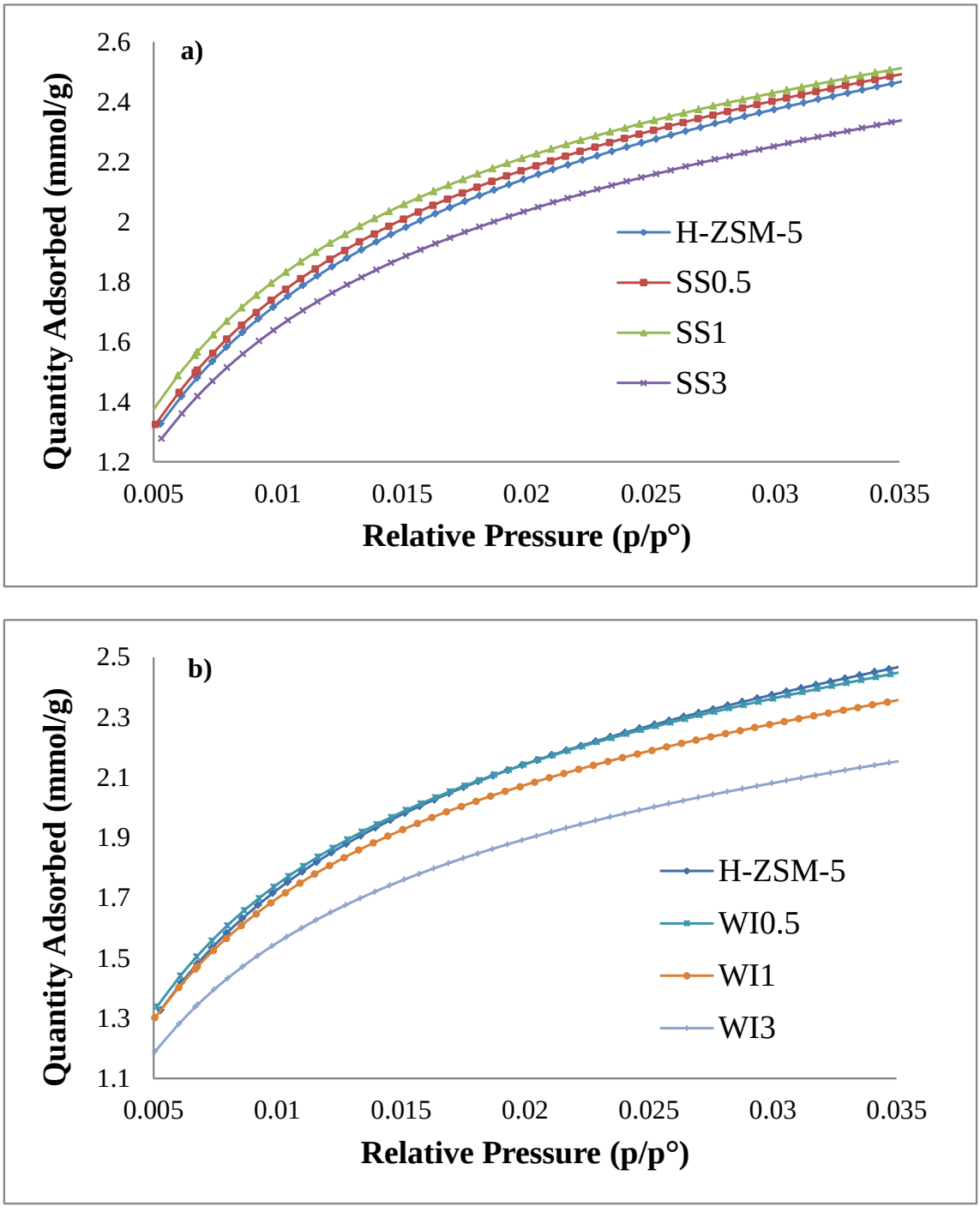

Figure 3.22 Low pressure CO_2 adsorption isotherm of H-ZSM-5 and the (a) SS and (b) WI catalysts.

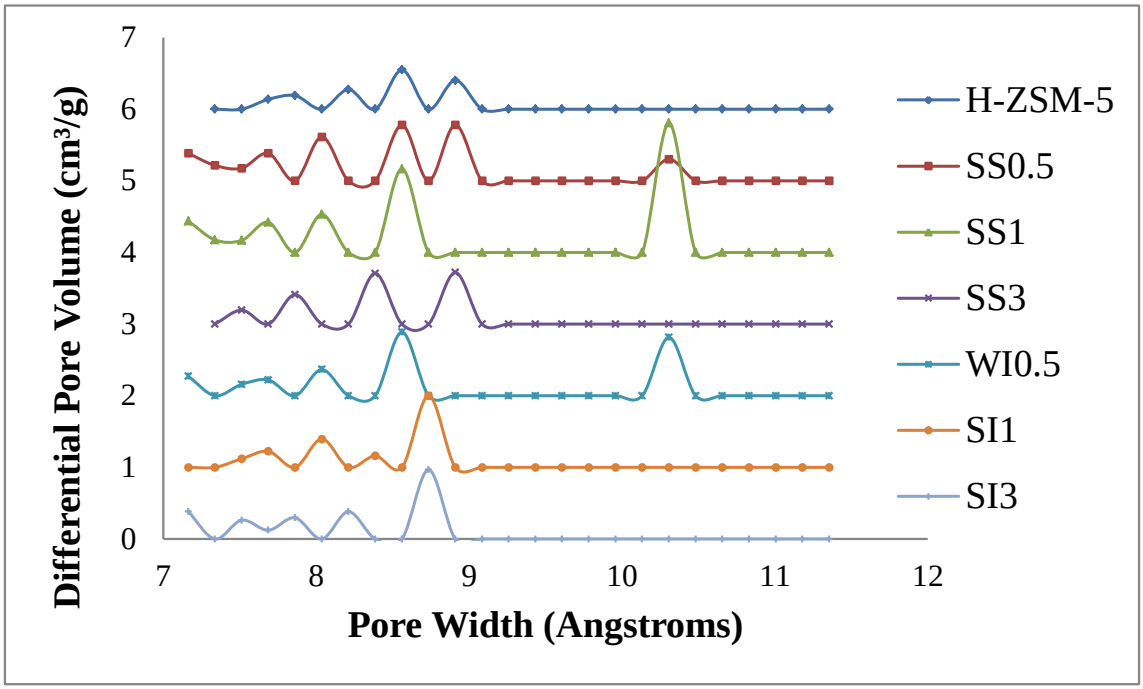

Figure 3.23 Pore size distribution of the H-ZSM-5, SS and WI catalysts using DFT model for analysis of CO_2 adsorption isotherm.

3.4 Summary

All of the results obtained from the various characterization techniques used in this chapter to determine how the NiO is distributed on the H-ZSM-5 support showed quite good agreement. From the integration of the results, it can be concluded that NiO is present as nanoparticles of different sizes, ranging from < 0.5 nm to ~ 10 nm. However, as NiO was determined by XRD to have crystal domains smaller than 8 nm, the largest NiO particles (> 10 nm in size) must be present in only small quantities. For the catalysts prepared by SS, the NiO particles are larger than for catalysts prepared by WI, since the SS catalysts are easier to reduce at lower temperatures. The NiO that can only be reduced at higher temperatures is stabilized by interactions with the Bronsted acid sites of the support, consistent with the DRIFTS results. This

suggests that the WI catalysts will ultimately be preferred, since the closer the metal phase is to the acid site, the better for the hydrocracking reaction. Larger NiO particles do block some of the pores in the meso- and microrange, thus reducing the zeolite surface area. Therefore, not all of the Ni is participating in the hydrocracking reaction. This is also supported by the TPR results, since not all of the NiO reduces at 400 °C, which is the temperature of reduction used during catalyst pre-treatment.

A comparison between the results obtained in this chapter and those reported in previous studies (as discussed in Section 1.1.2) is made below:

- Catalysts, such as those studied in this thesis work, can be made to have very different properties simply by changing the metal incorporation method (Molero H. et al., 2009) or even just by changing one step in the synthesis methodology (Hoang D. L. et al., 2004; Okal J. et al., 2009). This is due mainly to changes in the metal distribution and particle size on the support.
- Interactions between Ni and zeolite supports have been reported previously by different groups. For example, Melo et al. (2008) showed that there is more than one type of oxide species present when transition metals are incorporated into Ga-ZSM-5 zeolites (see Section 1.1.2.2). They observed that Pt^{2+} and $Pt^{+\delta}$ (detected by XPS) require quite high temperatures to be reduced due to their strong interactions with the Ga sites of the zeolite. Also, Hoang et al. (1994) found the same behaviour with Ni on a ZSM-5 zeolite when the catalysts were studied by CO-IR, observing that this was due to strong interactions of the metal with the Al sites of the support (see Section 1.1.1.1). As seen in this thesis, we also found that there are several types of interactions between NiO and the support (as shown by TPR) and also that there is a strong interaction between the metallic state (Ni), after catalyst reduction, and the Al sites of the support (as demonstrated using DRIFTS).

- The results obtained from the BET and BJH analyses showed that the specific surface area of the catalysts decreases as the Ni content increases. This effect was also observed by Gonzalez H. et al. (2004), Okal J. et al. (2009), and Molero H. et al. (2009), who attributed this to the blockage of pores by the relatively large incorporated NiO (or later Ni) particles.
- Metal nanoparticles of a range of sizes have been detected by using several different characterization techniques, e.g., Rietveld analysis of the XRD patterns (Okal J. et al., 2009), TEM (Okal J. et al., 2009), and H_2 chemisorption (Hoang D. L. et al., 1994; Poncelet G. et al., 2005). However, the methodology presented in this thesis (Simulated XRD, Section 3.3.2.2) offers a simple and rapid approach to determining the metal particle size.
- Comparisons between the outcome of using different incorporation methods for these types of catalysts are very few in the literature. In this thesis, we concluded that catalysts prepared by WI showed better dispersion than SS-derived materials (as shown primarily by XRD and TPR), and this has also been observed by Hernandez (2012) in the hydrocracking of toluene reaction. Also, Molero et al. (2009) mentioned that there was a significant variation in the performance of the catalysts in the hydrocracking of toluene, specifically in terms of the selectivity (C2 - C4), with WI being better than SS. Recently, Vitale et al. (2013) showed a comparison between WI and a novel metal incorporation method, which involves a one-step synthesis. This new method showed better metal distribution, acid properties, and performance toward the hydrogenation of toluene than WI. However, this method has not yet been catalytically tested using any Ni loadings other than 1 wt. %.

Chapter Four: **Analysis of Core Plugs from Tight Gas/Shale Reservoir**

4.1 Importance

In recent years, tight gas/shales have gained prominence as unconventional fuel sources because they offer an environmentally-friendly (natural gas) alternative to conventional oil. Consequently, their exploitation is desirable although little is known about gas storage and transport in these reservoirs. Previous studies have shown that some gas shales may contain a significant amount of organic matter (kerogen), wherein the gas is trapped in three different modes: compressed in the pores, adsorbed on the internal surface area, and dissolved in organic matter. The controls on gas storage and transport through the organic matter require additional research. Further, because routine methods used for conventional reservoir characterization are inapplicable (Bustin et al., 2008; Rushing et al., 2008; Sondergeld et al., 2010), new techniques for obtaining reservoir properties for unconventional reservoirs need to be explored and developed. In previous studies, our research group has evaluated tight gas samples from Western Canada using various techniques (Clarkson et al., 2012a). The current study attempts to provide additional insight by applying techniques that are not routinely applied to unconventional reservoirs, including X-ray Photo-electron Spectroscopy (XPS) and Auger Electron Spectroscopy (AES).

4.2 Introduction

In this chapter, non-routine characterization techniques, XPS and AES (explained in Chapter Two), are applied to tight gas samples from Western Canada and shales from different reservoirs in North America. The results will be discussed and compared with results obtained from

traditional techniques for the purpose of validation and to provide additional insight. Low pressure adsorption N_2 and CO_2 analysis, which is also not considered a routine method for unconventional reservoir analysis, has also been performed in order to obtain information about the pore size distribution and shape.

4.3 Experimental Methods

4.3.1 Description of the Samples

The tight gas core plug samples used in this work were cut from a whole core taken from a tight gas reservoir in Western Canada. The whole core was cut in oil-based mud using aluminum sleeve coring equipment. A total of 10 whole core samples, having a cylindrical shape (diameter = 1 in, and length = less than 1 in), were selected for this study. Sample depths in the reservoir are shown in Table 4.1.

Table 4.1 Whole Core Tight Gas Samples Used for Analysis.

Sample name	**S1**	**S2**	**S3**	**S4**	**S5**	**S6**	**S7**	**S8**	**S9**	**S10**
Depth (m)	3724.9	3727.0	3730.2	3733.7	3734.2	3736.9	3740.8	3743.8	3743.9	3749.7

Although some experiments presented in this thesis were previously reported (Clarkson et al., 2012a) for core samples in the as received condition, the current analyses with XPS and AES required only a small amount of sample (powder). The samples were prepared following the advice of Dr. T. Furstenhaupt (Manager of the Microscopy and Imaging Facility at the University of Calgary) by scraping the samples using a steel blade, thus creating small particles

(powder). This procedure was employed for X-ray Photoelectron Spectroscopy (XPS) and Auger Electron Spectroscopy (AES) analyses.

Another set of samples from different North America shale reservoirs (see Table 4.2) were also studied in this work. Some analyses were performed on these shales in a previous study (Clarkson et al., 2013). In this thesis, AES and XPS were also applied for these shales and additional low-pressure adsorption work performed. Shale samples were obtained in powder form from core plugs, with the particles being between 0.5 and 1.0 mm in diameter.

Table 4.2 Shale Samples Codification.

Formation	**Age**	**Code**
Barnett	Mississippian	B
Duvernay	Late Devonian	D
Haynesville	Late Jurassic	H
Marcellus	Middle Devonian	M
Muskwa-Cordova	Late Devonian	P
Milk River	Late Cretaceous	R
Muskwa	Late Devonian	U
Woodford	Late Devonian	W

4.3.2 Routine Methods

Routine analysis including scanning electron microscopy (SEM), X-ray diffraction (XRD) and Rock-Eval pyrolysis were performed in independent laboratories. For the tight gas samples, only 3 samples were selected for SEM, XRD and Rock-Eval Pyrolysis analysis. XRD results were analyzed by the software Jade® (version 8) and mineralogical analysis from XRDs has accomplished by Rietveld analysis (Rietveld, 1967). Rock-Eval pyrolysis was performed in a

Rock-Eval 6/TOC turbo instrument by using default parameters supported by Lloyd Snowdon (personal communication, Institute of Sedimentary and Petroleum Geology in the Geological Survey of Canada, AB, Canada). Details about the methodology in this technique were given elsewhere (Clarkson et al. 2012a). For the shale samples, XRD was performed with a normal focus Cobalt X-ray tube used in a Siemens Diffractometer D8 at 40 mA and 40 kV, while the mineralogical composition was obtained from Rietveld analysis.

4.3.3 Non-routine Methods

4.3.3.1 Auger Electron Spectroscopy (AES)

Auger spectra were collected on a Phi 690 scanning Auger NanoProbe system (Catalyst Surface Science Laboratory, Department of Chemical and Petroleum Engineering, University of Calgary), using a multi-channel detector with a cylindrical mirror analyzer and a field emission electron gun at 10 kV and 1 nA. The procedure followed was the same as for SEM (Section 2.2.1).

4.3.3.2 X-Ray Photoelectron Spectroscopy (XPS)

XPS spectra were collected, using a monochromatic Al source (1486.60 eV), on a PHI VersaProbe 5000 (Catalyst Surface Science Laboratory, Department of Chemical and Petroleum Engineering, University of Calgary) with a 25 W X-ray beam (~100 μm diameter). Charge compensation was achieved with low energy Ar+ ions and an electron flood gun. The XPS data were processed using MultiPack® software (Physical Electronics).

4.3.3.3 Low Pressure N_2 and CO_2 Gas Sorption Analysis

Tight gas core plugs samples were analyzed by low pressure N_2 adsorption using a Micromeritics ASAP 2010®. Samples were initially degased at 110 °C for ~ 17 h while the experiment was carried out at -196 °C. Time for analysis took longer than usual due to samples being core plugs; therefore, between 26 – 52 h were needed in order to equilibrate the pressure. The experiment took approximately 15 h per sample. Pore size distribution was studied by BJH (Gregg et al., 1982) and DFT (Do et al., 2003). The pore geometry in the DFT model employed was slit-pore for N_2 at 77 -196 °C.

Shale samples were studied by low pressure, N_2 and CO_2, adsorption analyses on a Micromeritics Tristar 3000 Analyzer (Department of Chemical and Petroleum Engineering at the University of Calgary). In this case, powder from core plugs was degassed at 60 ºC overnight in Ar (as previous studies recommend (i.e. Sondergeld et al., 2010). N_2 adsorption and desorption isotherms were collected at 77 K and analyzed using BET, Langmuir, BJH, and DFT methods. CO_2 adsorption isotherms were collected at 0 ºC, while specific surface area was determined by using BET, Langmuir, DFT, Dubinin-Astakhov, and Dubinin-Radushkevich methods.

4.4 Results and Discussion

4.4.1 Routine Methods

4.4.1.1 Surface Morphology by Electron Microscopy

With the SEM image of the samples S2 and S3 (Figure 4.1), the morphological structure of the samples is revealed. Grain sizes can be observed to vary in size from approximately a few hundred nanometers to a few micrometers. Fractures are also seen in the micrograph; these micro-fractures are believed to be generated by the pressure release of the sample after extraction

and are oriented along grain boundaries (Clarkson et al. 2012). Figure 4.2 shows another region of the sample S3 where a dolomite crystal is surrounded by stress-release fractures. Some fractures have micrometer-size apertures suggesting that these pores were enhanced during the coring process. Figure 4.3 is the backscattered electron image of the sample S8, where different grain sizes can be observed. There appear to be two distributions of grains in Figure 4.3: small grains that are between 5 – 10 μm and others that are between 20 – 50 μm. Fractures and pore space are also seen in this image, being in the order of 5 μm. No kerogen content observed in these SEM images; this result was expected as Rock-Eval pyrolysis results (see Section 4.4.1.3) indicated that the kerogen content for these samples is small.

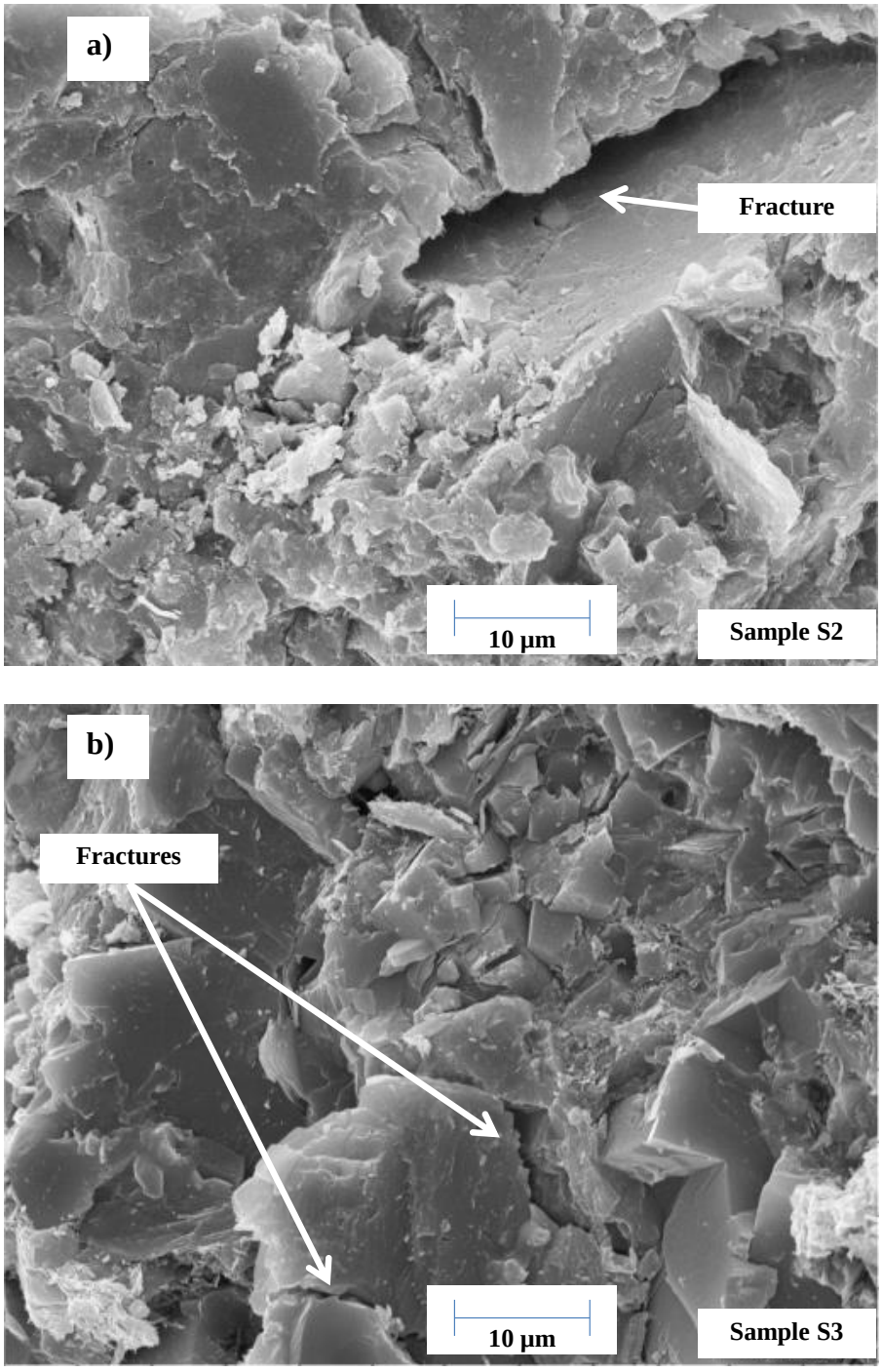

Figure 4.1 SEM images of sample S2 and S3 showing morphological structure. Scale bar 10 µm. (Modified from Clarkson et al., 2012a).

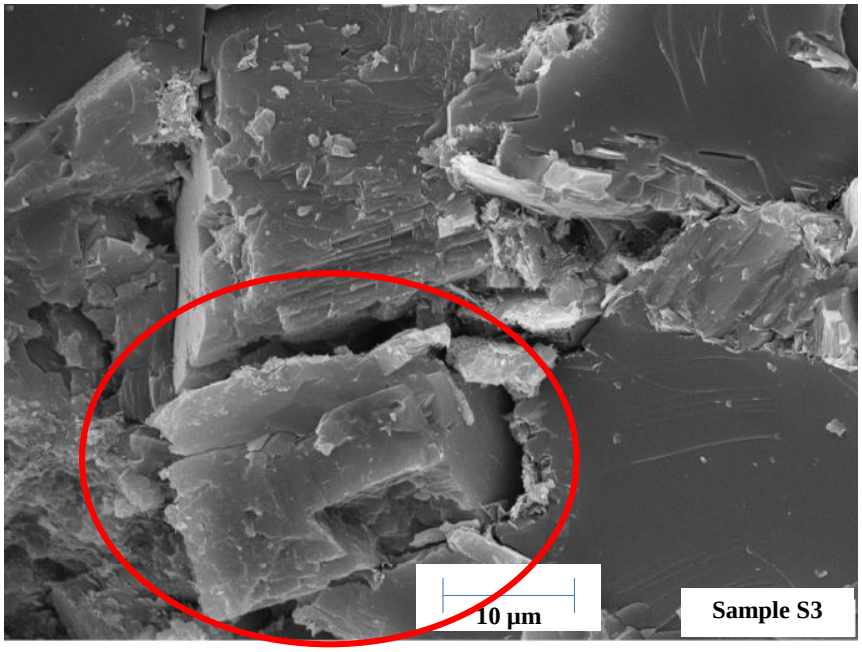

Figure 4.2 SEM image of sample S8 showing morphological structure. Scale bar 10 µm. (Modified from Clarkson et al., 2012a).

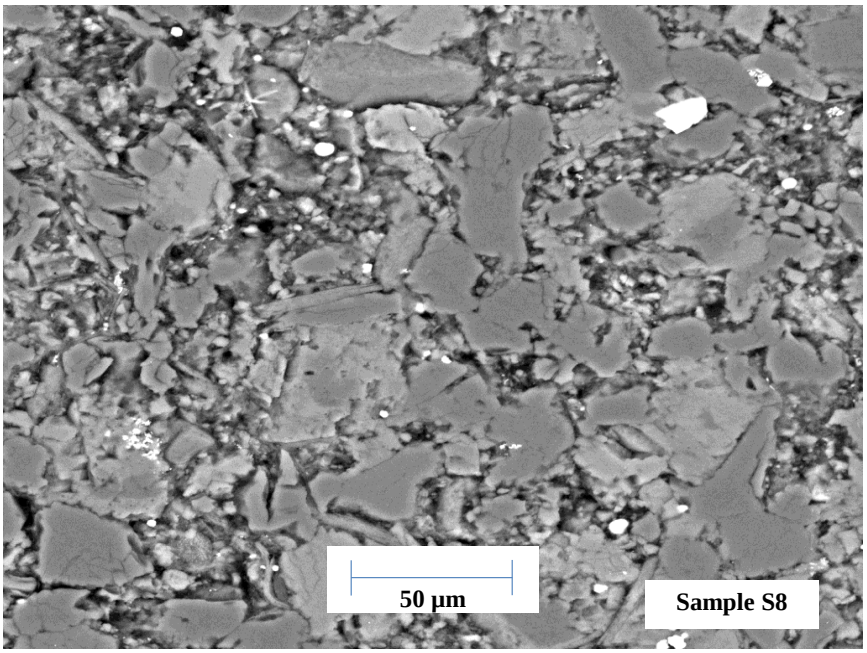

Figure 4.3 Back scattered electron image of sample S8. Scale bar 50 µm. (Adapted from Clarkson et al., 2012a).

4.4.1.2 Mineral Composition by XRD

XRD was performed on the tight gas samples as received (Figure 4.4). The major components are quartz, dolomite, illite, plagioclase, feldspar, with minor amounts of calcite and pyrite. The samples appear to have similar mineral compositions; however, there are two samples, S3 and S5, which have a low content of quartz, feldspar, and plagioclase while having high content of dolomite compared to the others. Note that sample S3 has no illite and S5 has high calcite content. These differences are taken into account in order to correlate the XPS results discussed in Section 4.4.2.2.1.

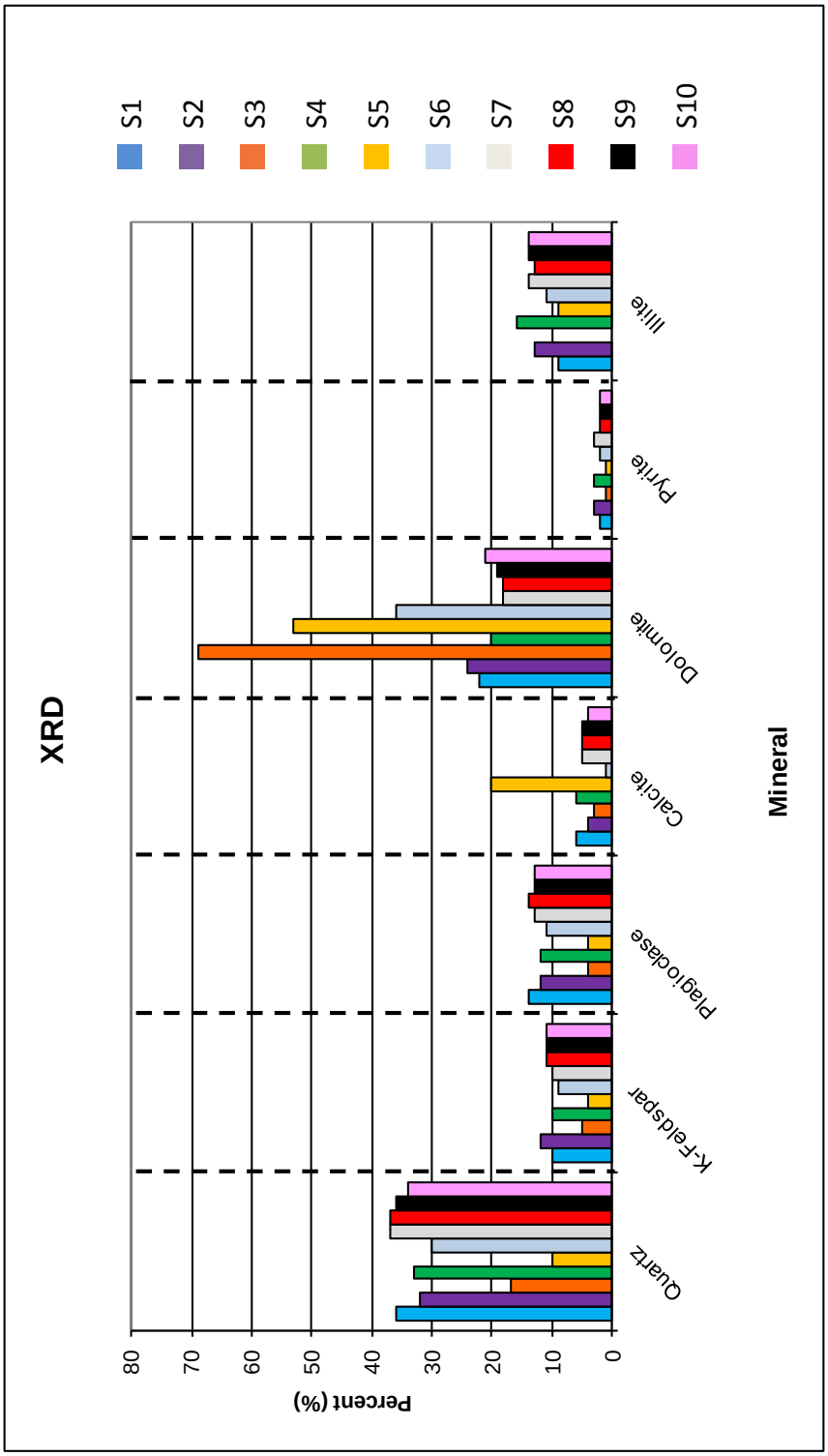

Figure 4.4 Comparison of mineralogical composition of the tight gas samples based on XRD analysis. (Adapted from Clarkson et al., 2012a).

For the shale samples, XRD analysis shows a wide variation in mineral composition among the samples taken from various shales in North America (see Figure 4.5). The predominant minerals are quartz, calcite, muscovite, and illite with minor amounts of dolomite, pyrite, and albite. Samples B (Barnett), P (Muskwa 2) and U (Muskwa) show higher quartz content while the lowest quartz content is present in sample M (Marcellus). Sample M, however, has the highest calcite content while samples B and U have the lowest calcite content. Samples H (Haynesville) and W (Woodford) have the highest muscovite content while samples B, M, P, and U have the lowest content. Finally, dolomite content is significant in samples H, M, and W while for samples B, P, and U it is almost absent.

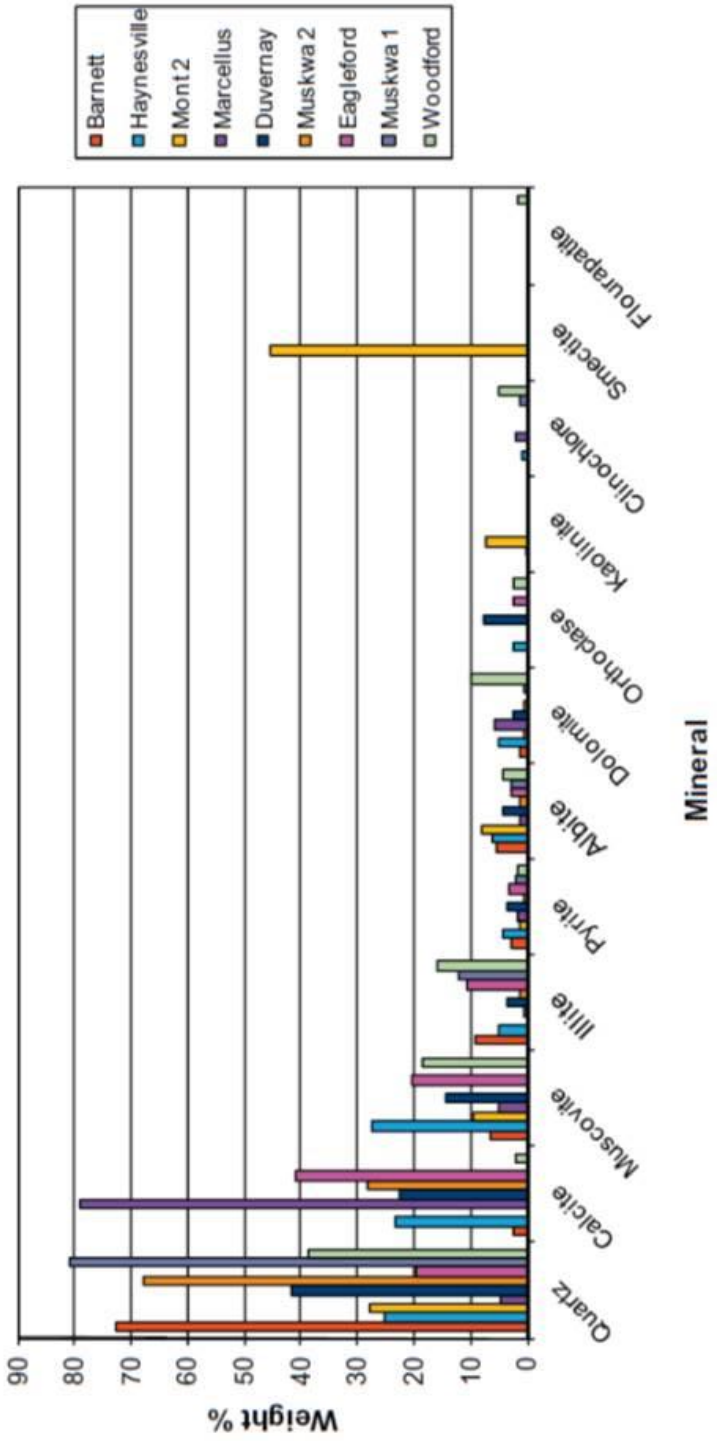

Figure 4.5 Comparison of mineralogical composition of the shale samples based on XRD analysis. Another nomenclature is used in this work (see Table 4.2) (Adapted from Clarkson et al., 2013).

4.4.1.3 Total Organic Content

Rock-Eval pyrolysis was performed on the samples in order to obtain information about their total organic carbon (TOC). Tight gas samples showed a low range of TOC (see Table 4.3 and Figure 4.6); samples S2 and S3 have the highest and lowest TOC content (0.63 and 2.50 wt. %), respectively. Most of the TOC is inert carbon (pyro-bitumen, kerogen, and residual) (Clarkson et al. 2012a).

Table 4.3 TOC obtained from Rock-Eval pyrolysis data for the tight gas samples.

Sample	S1	S2	S3	S4	S5	S6	S7	S8	S9	S10
TOC (wt. %)	2.27	2.5	0.63	2.1	0.95	0.87	1.86	1.37	1.07	1.85

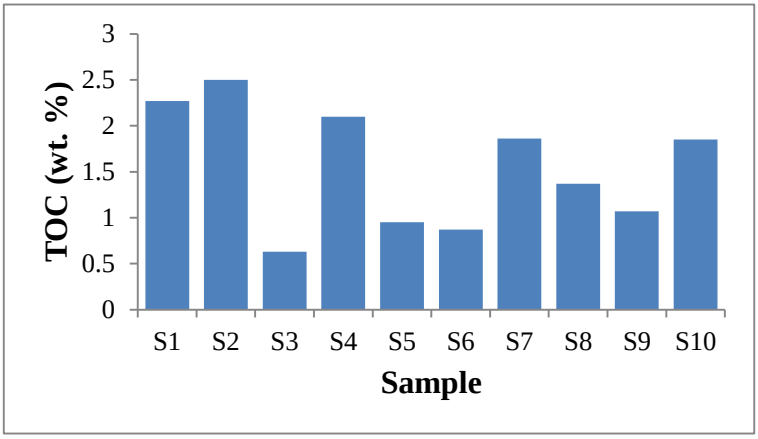

Figure 4.6 TOC of the tight gas samples. (Adapted from Clarkson et al., 2012a).

For the shale samples, TOC content was higher than for the tight gas samples (Table 4.4 and Figure 4.7). Samples B and R have the highest and lowest TOC content (4.11 and 1.28 wt. %), respectively.

Table 4.4 TOC obtained from Rock-Eval pyrolysis data for the shale samples.

Sample	B	D	H	M	P	R	U	W
TOC (wt. %)	4.11	3.84	3.94	1.57	NA	1.28	2.95	2.77

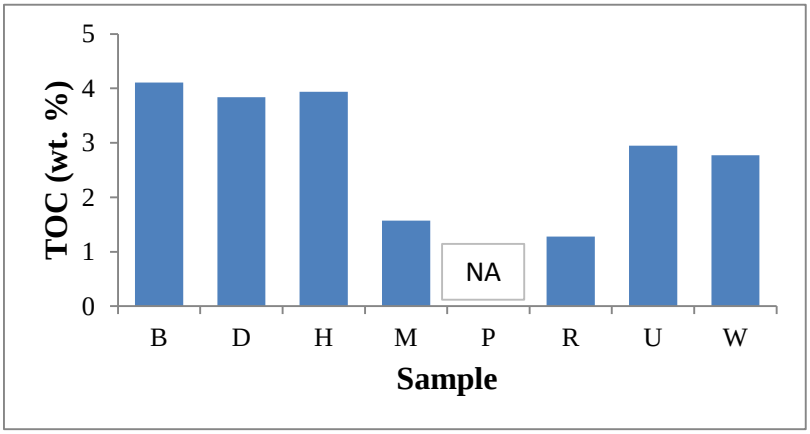

Figure 4.7 TOC of the shale samples. (Adapted from Clarkson et al., 2013).

4.4.2 Non-Routine Methods

4.4.2.1 Elemental Composition of Shale Samples Using Auger Electron Spectroscopy (AES)

AES spectra were collected from different regions of sample S2 (see Fig. 4.8a) as it was the sample having the most kerogen content (see Table 4.3) with the highest specific surface area (see Table 4.11). In order to analyze an AES spectrum, the lowest points of the derivative spectrum are assigned as the kinetic energies for each element; thus, signals at different energy values correspond to each element that is present in the sample (Figure 4.8b). Different locations such as laminations, small particles and inter-particle areas were chosen for this analysis.

In the first set of experiments, a large magnitude, broad peak located in the 500 eV region. This region is critical because it is where AES kinetic energies of the elements to be studied are

located as shown in Table 4.5. Therefore, the analysis could not be performed due to the charge effect masking the signal.

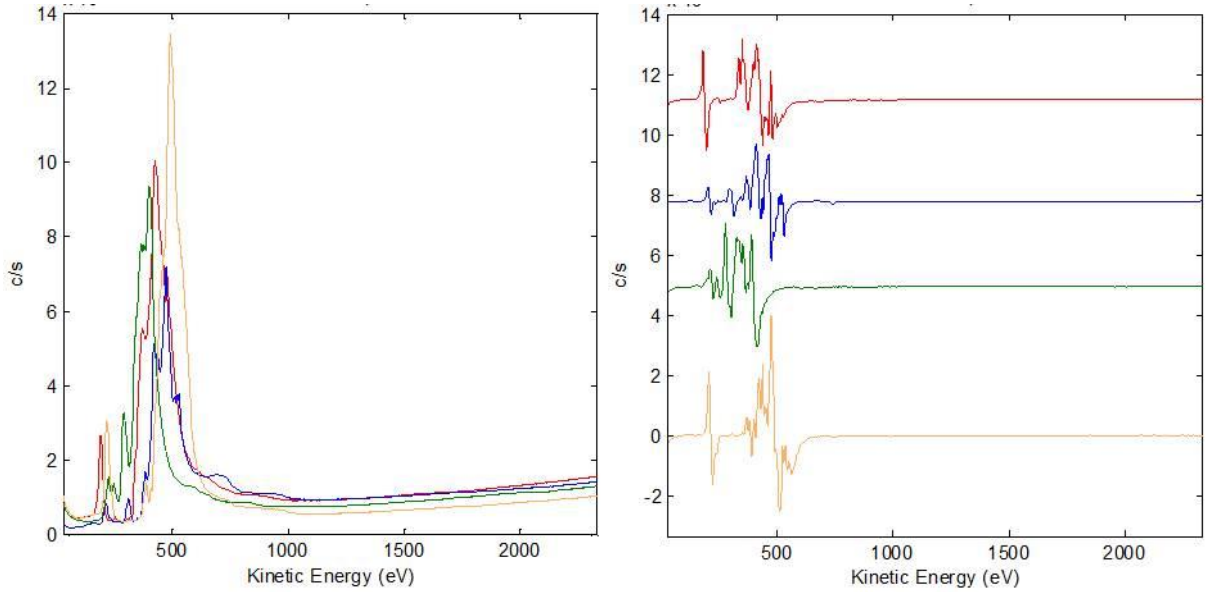

Figure 4.8 AES spectra of 4 points of sample S2: (a), and the derivative of the spectra (b).

Table 4.5 AES kinetic energies of some elements. Energies are ordered top to bottom from the most intense possible peak to the less intense.

Element	**C**	**N**	**O**	**Na**	**Mg**	**Al**	**Si**	**S**	**K**	**Ca**	**Fe**	**In**
AES Kinect Energy (eV)	275 245	389 373 358	510 489 473	996 957 928 1042	1188 1143 1109 1254	1396 1381 1345 1487	96 1621 1563 1739	153 2119	252 276 221 2979	291 322 387	705 654 600 565 519	405 346 300

A similar observation was made when the conditions of the AES electron gun were changed to a lower current value as seen in Figure 4.9a. Also, the short range of the derivative

spectra plots (Figure 4.9b-d) are not adequate to perform a good characterization of the sample since peaks at other positions appear (mostly generated by charge effect and noise) giving no correct information.

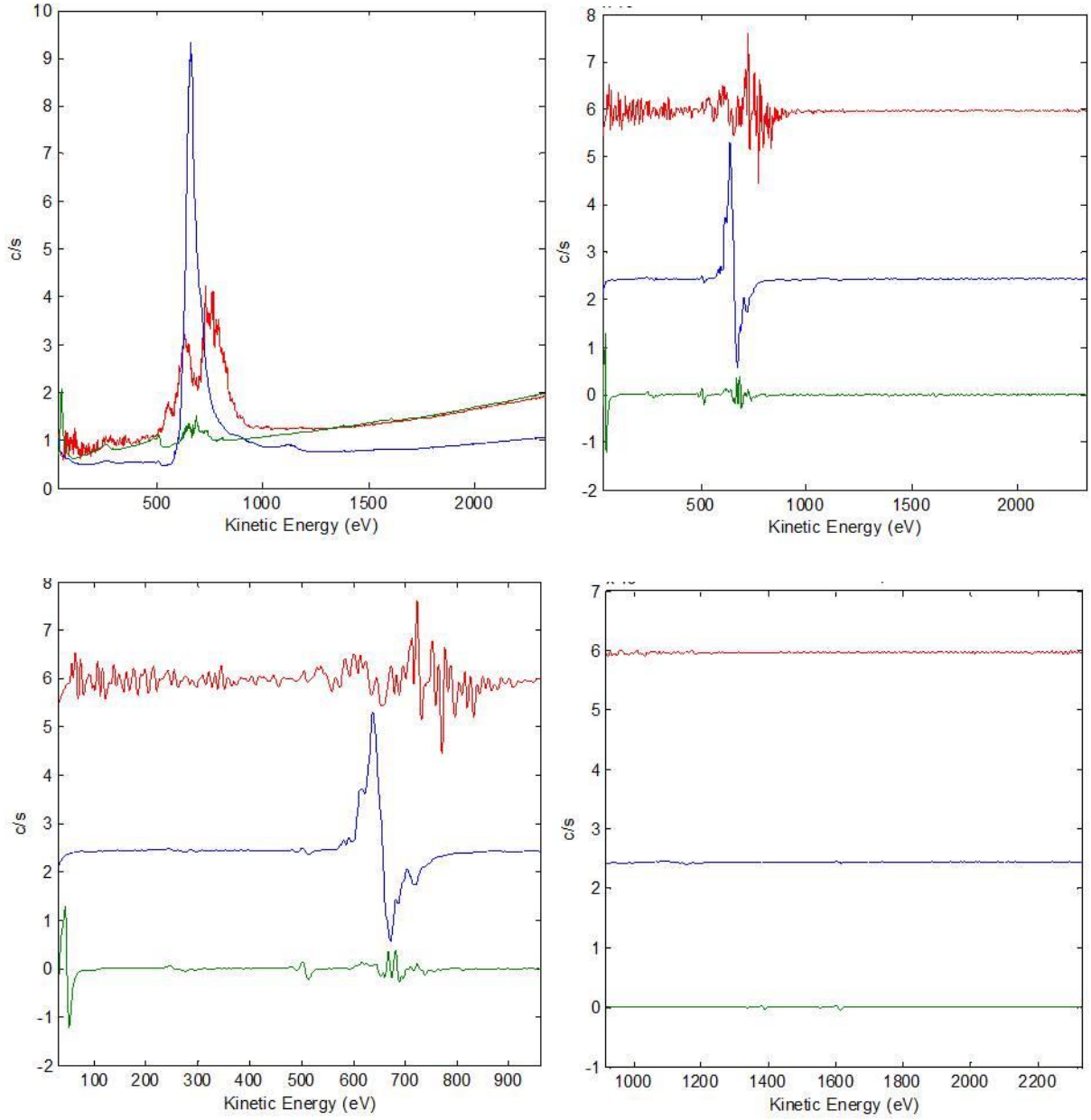

Figure 4.9 AES spectra of 3 points of sample S2: (a), the derivative of the spectra (b), and shorter ranges of the derivative of the spectra (c and d).

As explained in the "Theory of the Techniques Used" section, AES works by excitation-relaxation of atoms in the sample and release of the Auger electron. However, if the sample is non-conductor (as the samples studied here), the charge effect can appear and affect the measurements. The charge effect is generally observed in non-conductor samples, because these materials lack the capability to recover electrons from the adjacent metal parts of the instrument. The lost charge that is produced when liberating electrons (Secondary and Auger) during relaxation generates positive charge that is accumulated in the sample. This positive charge produces at the same time an electric field that modifies the electron trajectory before reaching the analyzer/collector. Therefore, the results obtained from AES are not very accurate since the information measured with the apparatus is not reliable.

Due to the problems experienced in the first experiments, the experimental procedure was modified to reduce the charge effect. The modified procedure followed the suggestions of Dr Molero (supervisor of the XPS and AES in the Chemical and Petroleum Department, University of Calgary) as follows:

- Thinner adhesive carbon tape was used to improve the conductivity between the holder and the sample.
- Shale particles were stuck in the indium foil to increase the contact points between the indium and the sample; therefore, the conductivity was increased.
- A tilted holder was used to increase the angle of the sample to the normal of the electron beam from 45º to 75 º. As noted in the AES manual, increasing this angle reduces the charge effect.

Using this modified procedure, the results improved considerably. Good signal/noise ratio spectrums were achieved, providing the opportunity to perform depth profiling in sample

shale P (Figure 4.10a). For depth profiling, the Ar+ ion gun was set at 3 nm/min in order to determine how the elements vary in the surface of the sample while sputtering. A change in the morphology is observed after removal of 300 nm from the sample (Figure 4.10b), demonstrating that the ion beam sputters equally on the entire surface. Seven study zones were selected to follow the signals of the elements present in the sample in order to obtain information from different morphological structures seen in the micrograph at different depths (see Figure 4.10a). Zone 1, that started as a grain of 500 nm in diameter attached to a bigger grain of 3 μm in diameter, was reduced to a smaller piece of approximately 100 nm in diameter after sputtering 300 nm (Fig. Figure 4.10b). Zone 2 does not seem to change after sputtering. Zone 3 shows a fuzzy agglomeration of small grains, which, after sputtering, is seen more clearly; this fuzzy section of the image could be due to charge effect generated by carbon covering the small grains. Zone 4 shows an agglomeration of smaller grains of around 200 nm in diameter. Zone 5 appears to be an isolated particle with a different morphological structure compared to the other grains. Zone 6 was another agglomeration of small particles as in Zone 4. Finally, Zone 7 shows a structure formed of laminations, one upon another.

Figure 4.11 shows the depth profile of shale P in the zones 1 and 3. Carbon present in the sample is removed after 25-35 nm, indicating that this is a fine layer rich in carbon covering the surface; this behaviour is seen in all the seven zones. In a comparison of the seven zones, only zones 1 and 4 showed to have carbon at greater depth in the sample. This second peak is about twice the size of the first carbon peak.

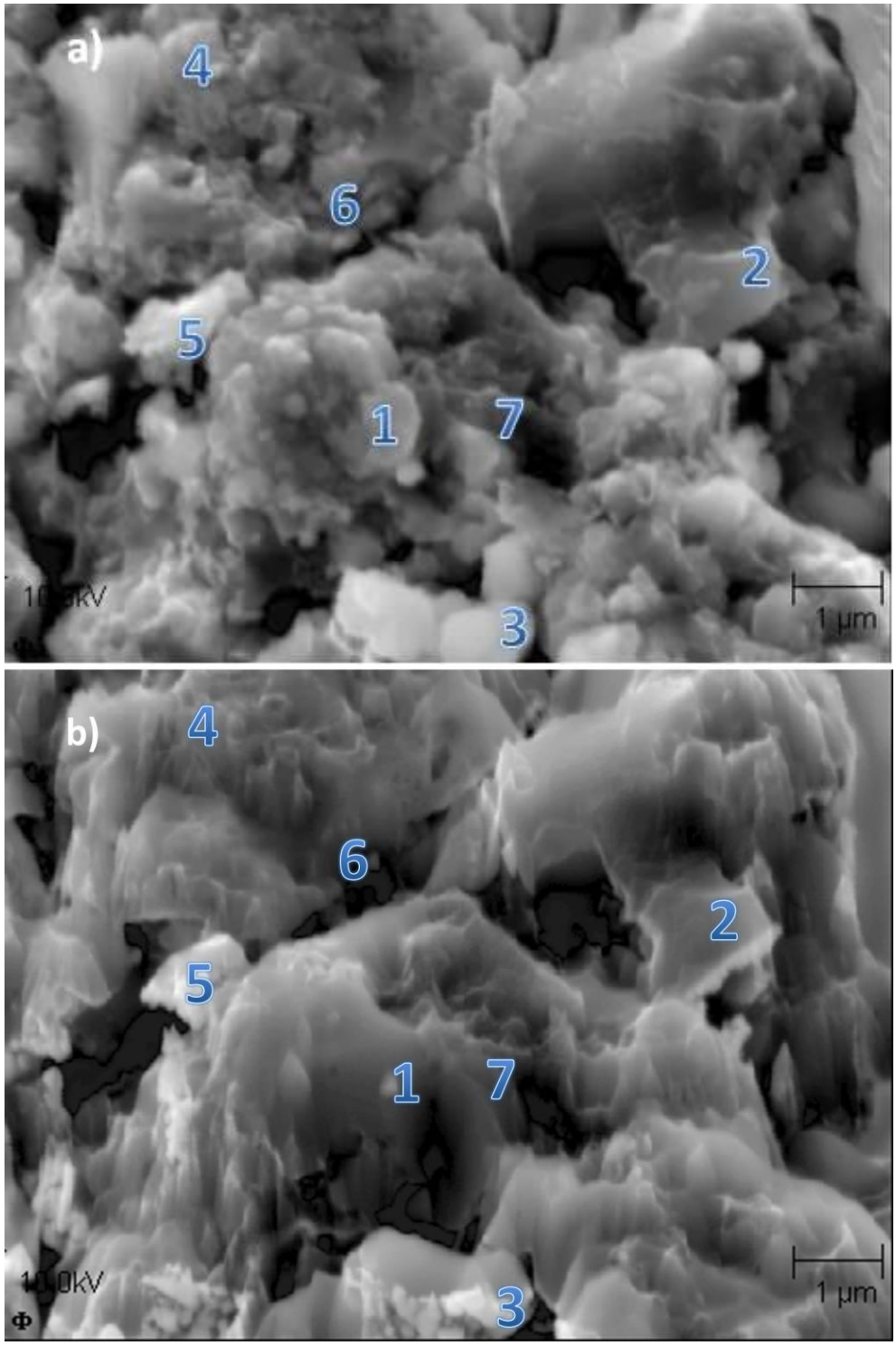

Figure 4.10 SEM image of the shale P at 10,000 X a) before and b) after sputtering; numbers indicate the study regions during sputtering.

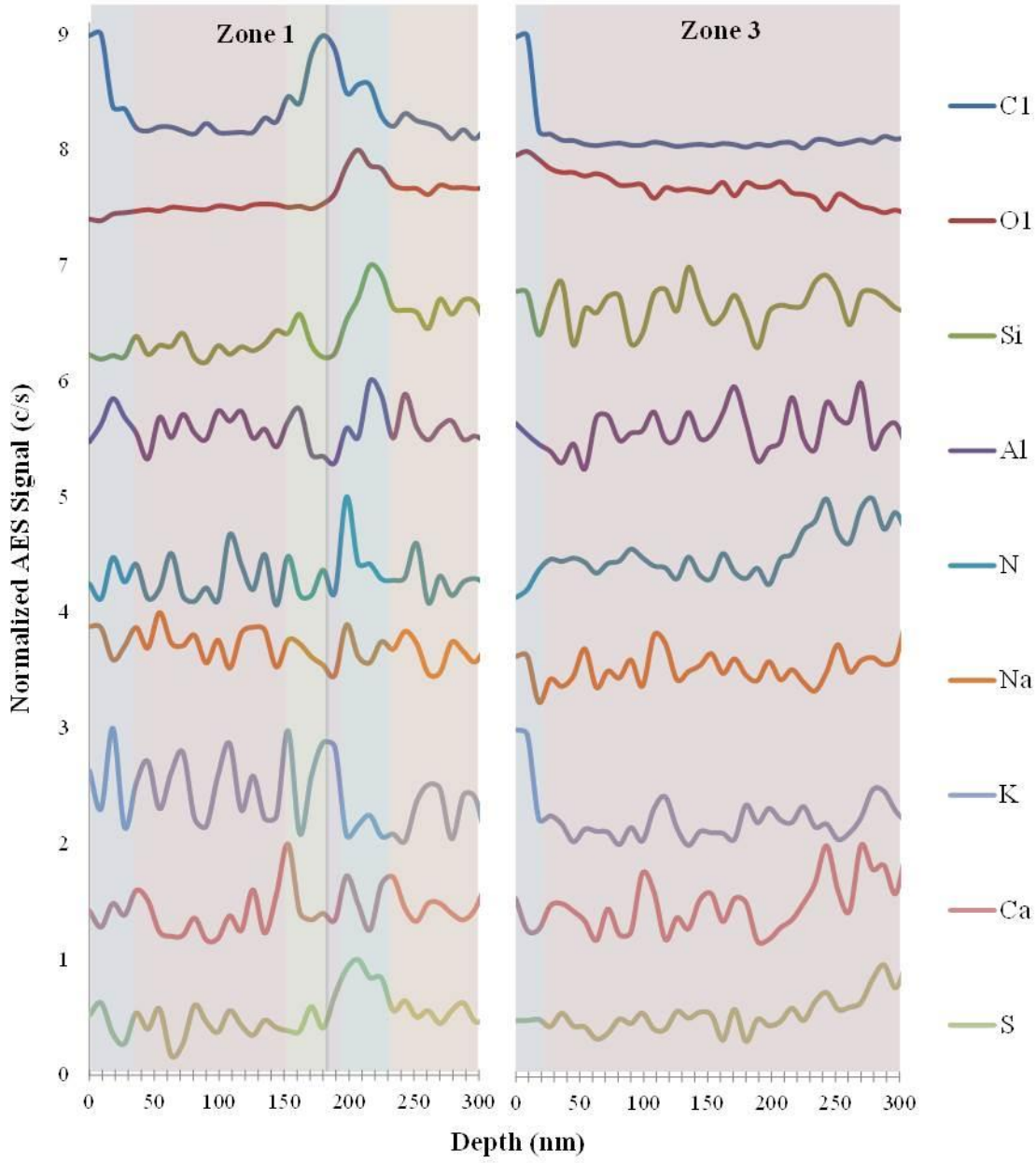

Figure 4.11 AES depth profile of shale P in zones 1 and 3 (Figure 4.10a). Sputter range: 300 nm and sputter rate 3 nm/min.

This observation leads to the following tentative interpretation: after removing the first carbon-rich layer, a lamination of the sample, about 60 nm in size (as seen in Figure 4.11 in the carbon signal), is found due to the recovery in the carbon signal and decrease in the Si and Al

signals is observed. Then, a second carbon-rich layer of about 60 nm is detected (150 nm depth). From this C signal reappearing, two interpretations may be made:

- The carbon layer is thicker (60 nm) than first layer removed (30 nm). C is located in an intergranular space (porous space).
- There are two carbon layers of ~ 30 nm, very similar to the first layer removed. These two C layers are located on the surface of the first lamination and a second that is beneath the first one. There may also be a porous space between the C layers which cannot be detected by AES depth profile because this tool does not recognize empty spaces in samples, such as a pore.

Figure 4.12 illustrates the interpreted geometry for the lamination and the C layers in the sample. Slit-shape pores were chosen for this interpretation as Section 4.4.2.4.1 and previous authors (Shanley et al., 2004; Clarkson et al. 2012b) suggest this type of geometry.

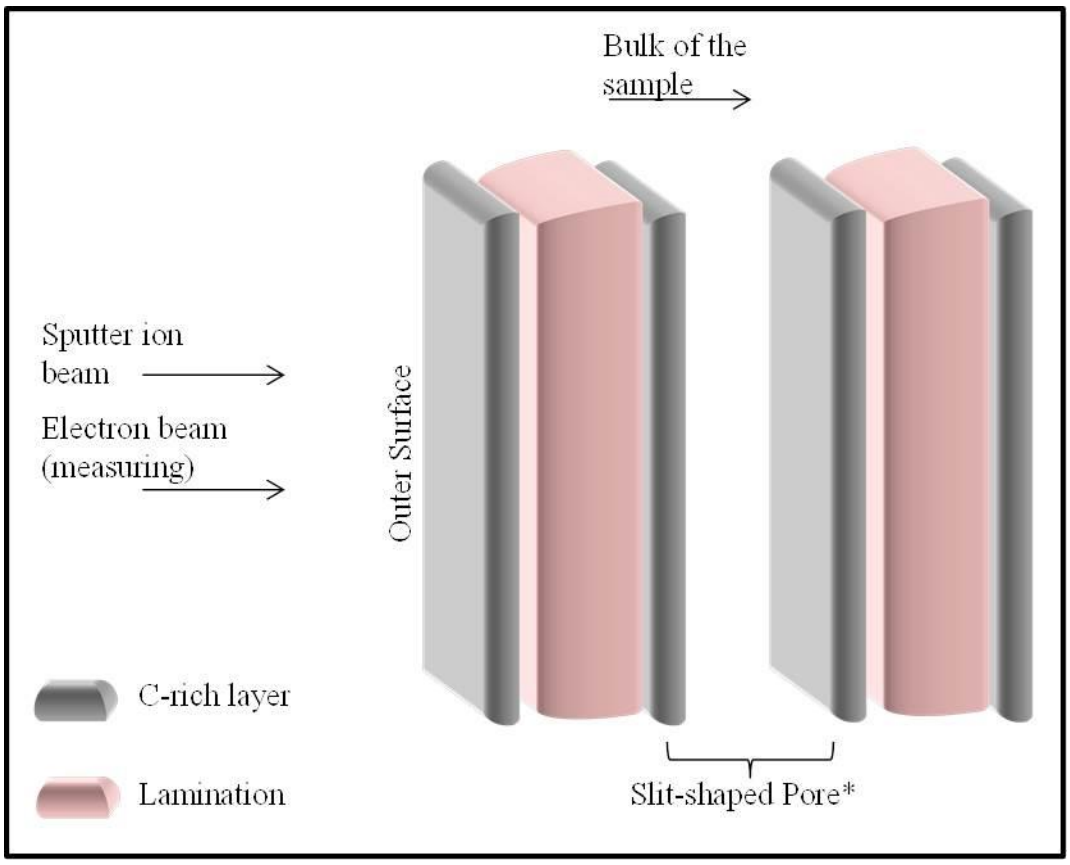

Figure 4.12 Scheme of the outer surface structure for shale P. * slit-shaped is considered the geometry of the pore for this samples as is discussed in Section 4.4.2.4.1.

The elemental composition of the grain/lamination in zone 1 (from 40 to 150 nm depth), is mostly O, Al, and Si; however, a decrease in the signal of potassium when the third carbon-rich layer appears suggest that potassium is another element present in the lamination. As seen in Section 4.4.1.2 and from XRD results (Clarkson et al., 2013), there could be three possible minerals: either Illite, k-feldspar or Clinochlore $(Mg,Fe^{2+})Al((OH)_8/AlSi_3O_{10})$; however, the Mg and Fe signals were not followed during AES spectrum collection, so identification of Clinochlore cannot be confirmed.

4.4.2.2 Elemental Composition by X-ray Photoelectron Spectroscopy

4.4.2.2.1 Tight Gas Samples

Table 4.6 shows the atomic percent of each element present in the tight gas samples. These values were quantified using the total area under the XPS spectra signal for each element. Note that C, O, Al, Si, K, Ca, and Fe are present in each sample, while the remaining elements (Na, and Mg) and heteroatoms (N and S) were found in some of them.

Table 4.6 XPS elemental quantification of tight gas samples.

Element (at. %)	**S1**	**S2**	**S3**	**S4**	**S5**	**S6**	**S7**	**S8**	**S9**	**S10**
C 1s	47.91	24.87	28.81	20.1	25.4	34.73	26.31	59.47	58.32	59.83
N 1s	0	2.05	1.29	2.02	0	0	1.26	0	0	0
O 1s	35.76	49.47	50.99	52.75	53.65	45.63	49.06	28.26	30.67	29.99
Na 1s	1.01	0.79	0.71	0.82	0.9	1.21	0.39	0	0	0
Mg 1s	0.57	0.55	0.85	0.48	0.72	0.7	0.43	0	0	0
Al 2p	2.85	4.74	2.17	5.1	2.86	3.61	4.92	1.94	2.36	2.25
Si 2p	7.88	11.88	6.33	12.63	6.44	8.99	12.55	8.16	6.44	5.56
S 2p	0.25	0.39	0.28	0.29	0.28	0.57	0.34	0.2	0	0
K 2p	1.07	1.92	0.69	2.28	1.01	1.26	2.14	0.87	0.79	1.02
Ca 2p	1.84	2.47	6.56	2.66	7.4	2.69	2.03	0.87	1.11	1.26
Fe 2p	0.87	0.86	1.32	0.88	1.34	0.6	0.58	0.23	0.32	0.1

A better visualization of the elemental at. % in the tight gas samples is given in Figure 4.13. XPS quantification of elements such as Si, Al, and Ca provides a close match to the results obtained from XRD (see Section 4.4.1.2, Figure 4.4). Elements are studied separately for comparison of XRD and XPS.

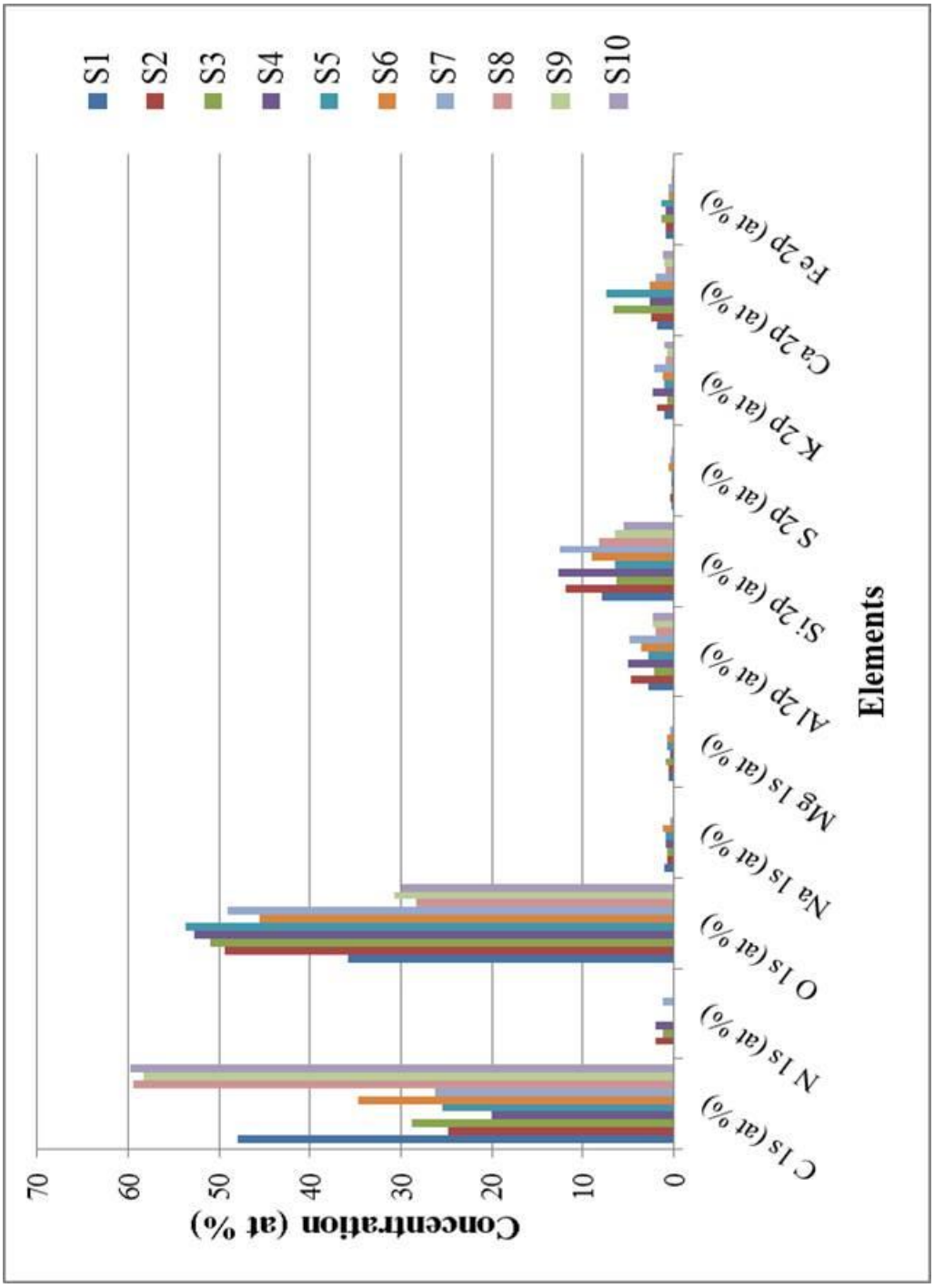

Figure 4.13 XPS elemental analysis of the tight gas samples.

Silicon can be found in some minerals such as quartz (SiO_2) and plagioclase ($NaAlSi_3O_8$ – $CaAl_2Si_2O_8$). Samples S3 and S5 have the lowest content of quartz and plagioclase according

to XRD analysis (Section 4.4.1.2); XPS quantification similarly suggests that these samples have the lowest silicon content compared to the others (Table 4.6). The XPS results appear robust because the study area is large enough (1 mm x 1 mm) to capture many grains of those minerals. However, the amount of sample used for XPS is very low compared to a bulk characterization technique, such as XRD. Thus, there may be a bias that may affect the results obtained from XPS, since all the representative grain may not have been selected for the analysis.

Aluminium, which is present in illite ($(K,H_3O)(Al,Mg,Fe)_2(Si,Al)_4O[(OH)_2,(H_2O)$), is being detected in the XPS for samples S2, S4, and S7. According to the XRD results, these same samples have a high illite content.

Calcium is an element that also demonstrates good agreement between the XRD and XPS results. From XRD, samples S3, S5 and S6 have high dolomite ($(Ca,Mg)(CO_3)_2$) content; as quantified by XPS, these samples have the highest concentration of calcium. This specific match supports one of the main conclusions in previous work (Clarkson et al., 2012b); samples S3 and S5 have larger pore sizes compared to the other samples due to the lack of organic matter and richness of carbonates.

Moreover, samples S1, S8, S9, and S10 have the lowest content of dolomite and calcite ($CaCO_3$) according to XRD, both minerals containing carbonates (inorganic carbon); also, XPS for these samples yielded minor amounts or a total absence of calcium, magnesium, and inorganic carbon (discussed later in this Section). The signal at 289.9 eV (XPS position for CO_3) was not considered in the curve fitting due to the noise present in the spectra, but because the other four signals for carbon reasonably fitted (as seen further in Section 4.4.2.3.1, Figure 4.16), the carbon associated with carbonate could be estimated by subtracting from the total carbon content detected.

Additionally, heteroatoms (O, S, and N) could be found by XPS. However, identification of species for sulphur and nitrogen was not possible to achieve because of the low signal/noise ratio in the spectra, due in turn to the low content of these elements in the samples - this is similar to what was discussed in the previous paragraph about carbonates. Oxygen was quantified by XPS and separated into organic oxygen (oxygen bonded to carbon) and inorganic oxygen (oxygen forming carbonate, which is ionic bonded to metals) following the calculation performed by other researchers (Kelemen et al., 2007). Total organic and inorganic oxygen concentrations are given in Figure 4.14 showing that smaller values of inorganic oxygen is presented in samples S1, S8, S9, and S10. These results are not completely consistent with the TOC obtained from Rock-Eval pyrolysis (Table 4.3); however, XPS was expected to show more C quantities as C is mostly located on the surface of the samples.

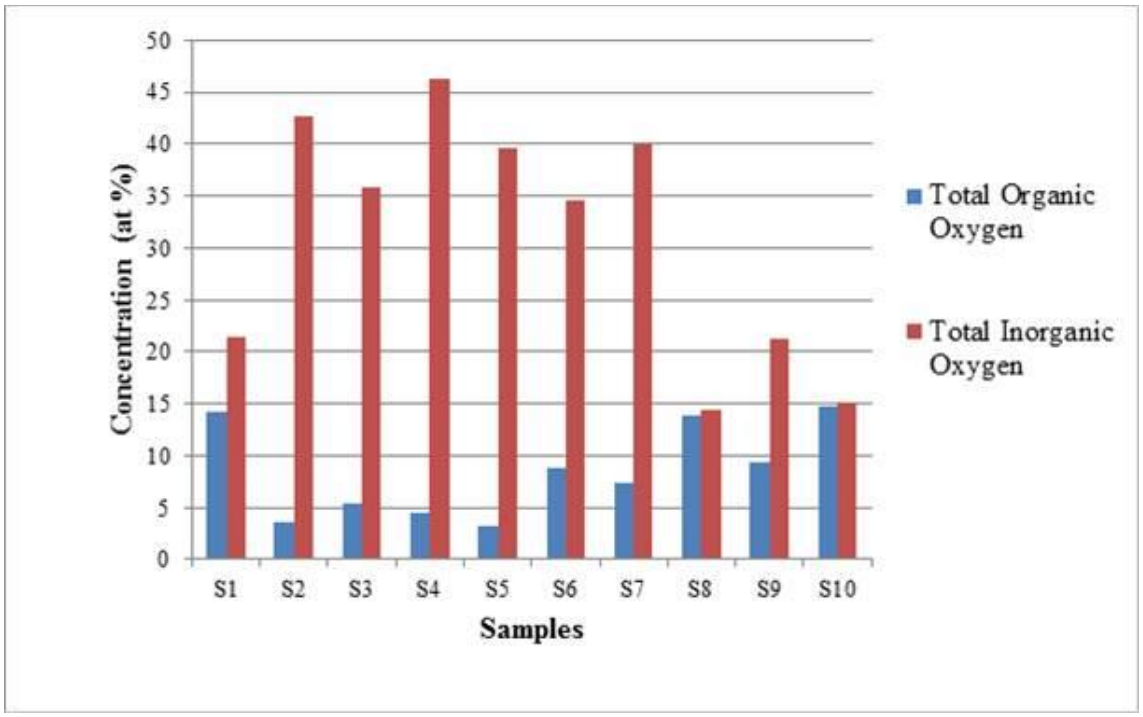

Figure 4.14 XPS quantification of total organic and inorganic oxygen.

4.4.2.2.2 Shale Samples

Table 4.7 shows the atomic percent of each element present in the shale samples. Note that C, O, Si, Ca, and Fe are present in each sample, while the remaining elements Na, Mg, Al, and C were found in some of them as well as N. Sulphur was not detected in any of the shale samples analyzed by XPS. A better visualization of the elemental at % in the tight gas samples is given in Figure 4.15. XPS quantification of elements such as Si and Ca closely matches with the results obtained from XRD (Clarkson et al., 2013).

Table 4.7 XPS elemental quantification of shale samples.

Element (at. %)	**Shale B**	**Shale D**	**Shale H**	**Shale M**	**Shale P**	**Shale R**	**Shale U**	**Shale W**
C 1s	23.18	48.47	26.71	26.3	48.35	6.53	15.11	19.26
N 1s	2.44	0	3.13	2.25	10.54	0.01	0.02	0
O 1s	51.51	35.45	47.86	44.63	28.61	61.88	55	53.2
Na 1s	2.21	1.93	0	0.01	0	2.9	2.11	1.53
Mg 1s	0.61	1.39	0	0.83	0.01	1.61	1.49	0
Al 2p	5.73	3.14	6.81	2.98	0	7.74	7.36	7.54
Si 2p	12.06	7.12	7.64	6.04	9.79	16.92	15.78	16.04
K 2p	0.96	0.58	0.8	0.59	0	0.92	1.33	1.11
Ca 2p	1.06	1.47	6.61	7.18	2.11	0.89	0.92	0.9
Fe 2p	0.25	0.44	0.44	0.63	0.58	0.59	0.41	0.41

Si is commonly found in quartz and plagioclase. From the XPS results, shales B and U have the highest Si content, which is consistent with the XRD results presented in Figure 4.5 (Clarkson et al., 2013). .Ca content from XPS is highest for shale M, which also has the highest

content of calcite as determined by XRD. Finally, XPS also gives the highest values of Al and K for the two shale samples U and W, consistent with XRD results.

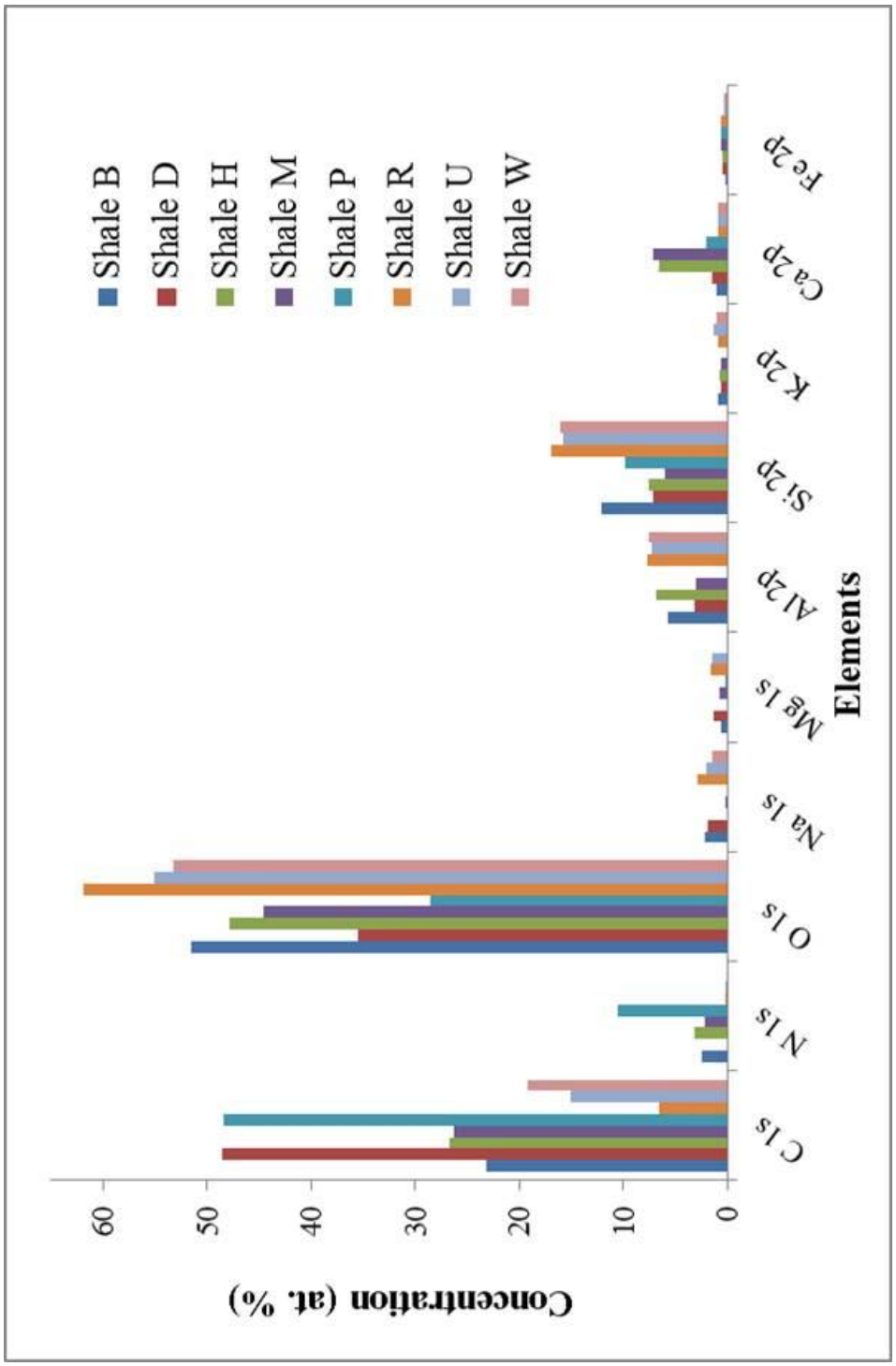

Figure 4.15 XPS elemental analysis of the shale samples.

4.4.2.3 Total Carbon and Organic Carbon by XPS

4.4.2.3.1 Tight Gas Samples

Fig. 4.16 shows the curve fitting of samples S2 and S3 using XPS. From the different binding energies and curve fitting performed in MultiPack®, the percentage of different carbon species for each sample can be estimated. The carbon species found in the XPS spectra were determined by the following peak positions: 284.8 eV for carbon bound to carbon by a single bond, which represents both aliphatic and aromatic carbon (C-C); 286.3 eV for carbon bound to oxygen by a single bond, such as C-O or C-OH; 287.5 eV for carbon bound to oxygen by two carbon bonds (C=O); 289.0 eV for carbon bound to oxygen by three bonds (O-C=O), and finally 289.9 eV for carbonate (CO_3) (Kelemen et al., 2007). The amount of different carbon species is also given in Table 4.8.

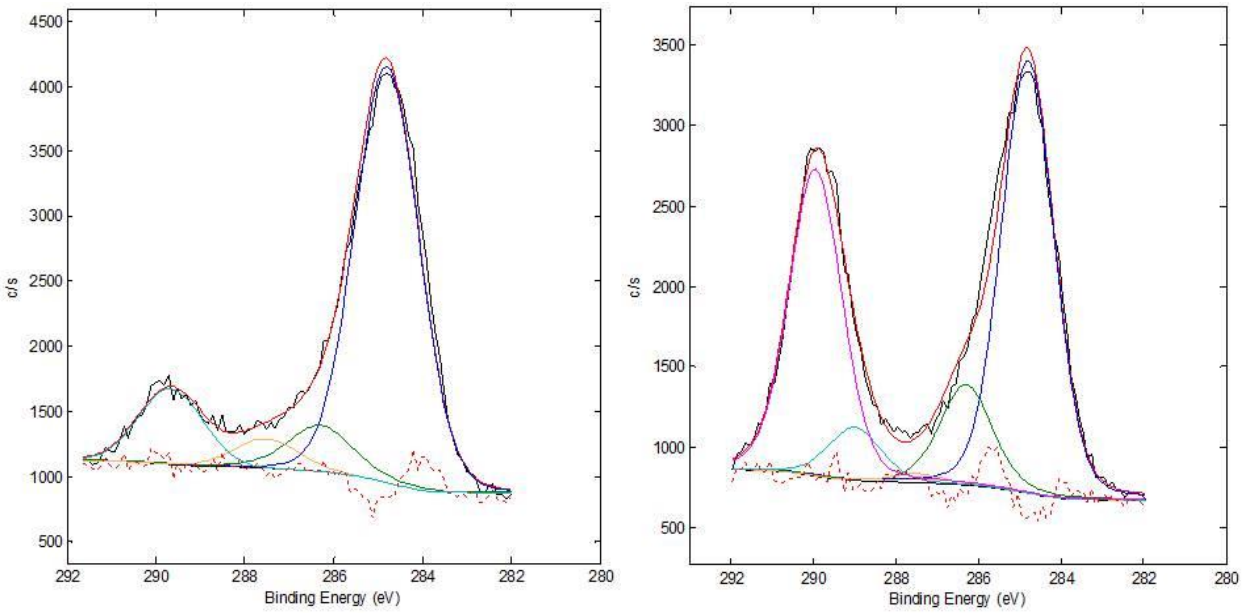

Figure 4.16 XPS curve fitting of the carbon signal for samples S2 (a) and S3 (b).

Table 4.8 XPS quantification of the carbon species.

Carbon Specie (Binding Energy)	**S1**	**S2**	**S3**	**S4**	**S5**	**S6**	**S7**	**S8**	**S9**	**S10**
C-C (284.8 eV)	33.66	18.16	13.58	13.61	11.38	23.72	17.31	45.64	48.89	44.99
CO_3 (290.9 eV)	0.00	3.15	9.88	2.03	10.70	2.15	1.66	0.00	0.00	0.00
C-O (286.3 eV)	9.28	2.32	3.35	2.92	2.24	6.29	4.93	9.28	4.81	9.32
C=O (287.5 eV)	0.79	1.24	0.30	0.59	0.77	0.61	1.44	0.00	1.51	0.62
O-C=O (289.0 eV)	4.17	0.00	1.70	0.94	0.31	1.95	0.96	4.54	3.11	4.90

The carbon content quantification obtained from XPS cannot be compared directly with the results obtained from Rock-Eval Pyrolysis (Figure 4.7) because XPS gives results in at % and Rock-Eval Pyrolysis gives results in wt. %. After conversion of the XPS values to wt. %, we find however that the highest value of TOC obtained from Rock-Eval Pyrolysis (2.33 wt. % for sample S2) is much smaller than the lowest value of organic carbon obtained from XPS (9.40 wt. % in sample S5) (see Table 4.9). Organic Carbon values obtained from the two different techniques are not close and no similarities are seen in the trend through the samples. It is important to highlight that XPS is a characterization technique for surfaces as explained in Section 2.1, while Rock-Eval Pyrolysis is a bulk technique; therefore the values of carbon content found by those two techniques are not necessarily expected to be the same.

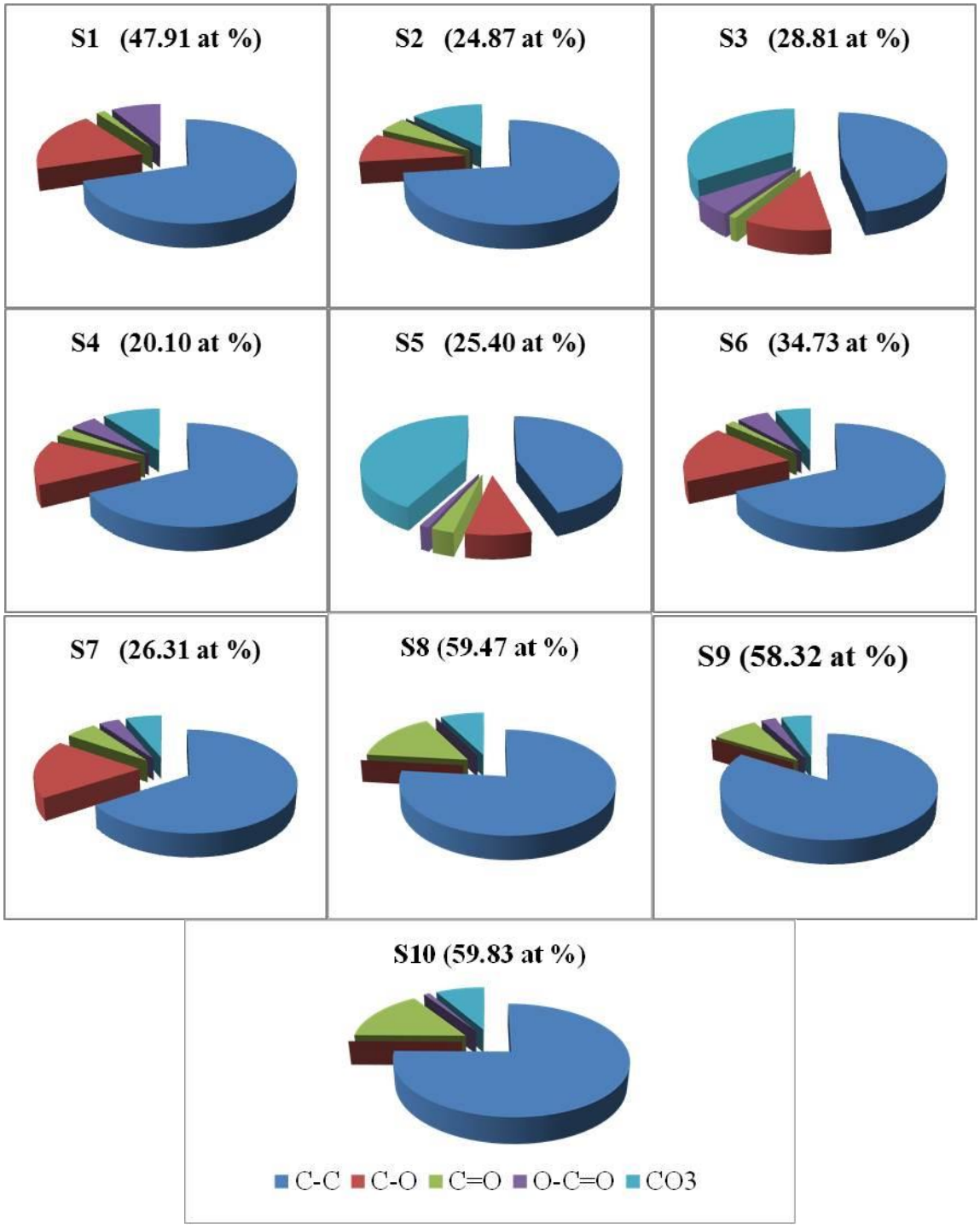

Figure 4.17 XPS quantification of the different carbon species in the tight gas samples (the number beside sample name is the total atomic % of C present in each sample).

Table 4.9 Comparison of Rock-Eval Pyrolysis and XPS carbon content.

Sample	Rock-Eval Pyrolysis	XPS	
	TOC (wt. %)	Organic Carbon (wt. %)	Inorganic Carbon (wt. %)
S1	2.27	34.77	0
S2	2.33	14.13	2.05
S3	0.63	12.46	6.50
S4	2.1	11.48	1.29
S5	0.95	9.40	6.83
S6	0.87	22.36	1.47
S7	1.86	16.17	1.09
S8	1.37	46.51	0
S9	1.07	45.82	0
S10	1.85	47.56	0

4.4.2.3.2 Shale Samples

In order to calculate the carbon species in the shale samples, the same methodology employed in the previous section (4.4.2.3.1) was used. Table 4.10 provides the different species of carbon contained in the shale samples, which is better visualized in the charts of Figure 4.18. Note that the C content varies strongly among the shale samples; moreover, the species of C vary substantially. This is likely due to the fact that the shale samples come from a number of different shale plays with different depositional and diagenetic history. Another aspect to be highlighted is the fact that shale P does not show CO_3 content indicating that the Ca and Mg

contents found previously (Section 4.4.2.2.2), must be associated with minerals other than calcite or dolomite. The results are consistent with XRD (Figure 4.5).

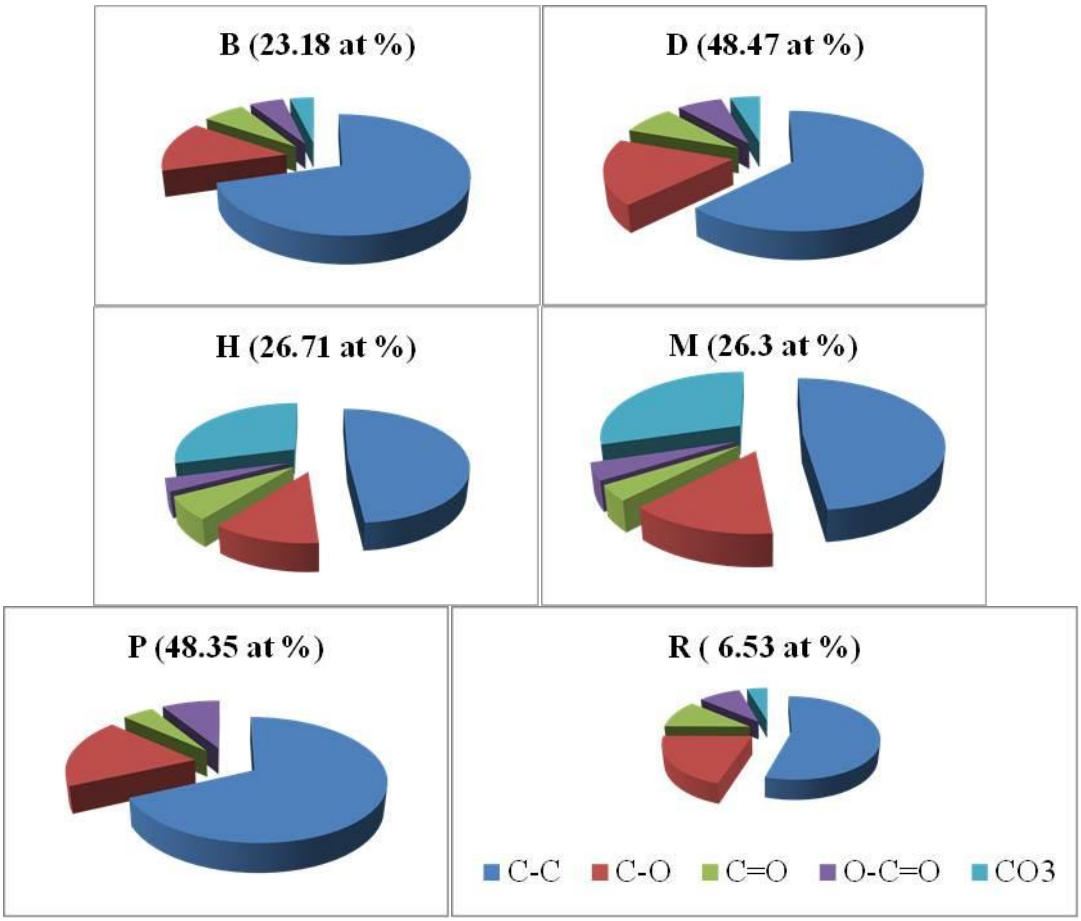

Figure 4.18 XPS quantification of the different carbon species on the shales B, D, H, M, P, and R (the number beside sample name is the total atomic % of C present in each sample).

Table 4.10 XPS quantification of the carbon species.

Carbon Specie (Binding Energy)	Shale A	Shale B	Shale C	Shale H	Shale M	Shale P
C-C (284.8 eV)	62.51	70.46	54.8	48.68	48.22	68.05
CO_3 (290.9 eV)	18.03	14.11	20.29	12.05	14.04	18.6
C-O (286.3 eV)	8.1	6.52	11.07	6.59	3.8	4.71
C=O (287.5 eV)	6.84	5.22	9.31	3.61	4.22	8.64
O-C=O (289.0 eV)	4.52	3.68	4.5	29.08	29.73	0

4.4.2.4 Pore Size Distribution by Low Pressure Gas Sorption

4.4.2.4.1 Low Pressure N_2 Adsorption

The specific surface area of the tight gas and shale samples is presented in Table 4.11. In order to remove impurities adsorbed on the samples, a pre-treatment was performed, consisting of heating the tight gas and shale samples to 110 and 60 °C in an Ar atmosphere overnight, respectively. Note that, this analysis was performed in the tight gas core plugs as received and in the powdered shale samples. The average specific surface area for the tight gas samples obtained from BET is 4.92 m^2/g, with the highest and lowest surface areas being for sample S2 (7.28 m^2/g) and S3 (1.78 m^2/g), respectively. For the shale samples, the average specific surface area obtained from BET is 10.1 m^2/g, with the highest and lowest values being for sample P (14.67 m^2/g) and M (0.5 m^2/g), respectively. Note that sample M has a small surface area, but its pore volume is not as low as the tight gas samples which have more specific surface area. Another point to highlight is that the specific surface area given by BET is close to the values obtained from the BJH-ads model while Langmuir specific surface area is higher than the other models.

The results of gas sorption analysis of the tight gas samples have been discussed previously in other work (Clarkson et al. 2012a), as well as the geological study (Clarkson et al. 2012b). In this section, the experiments performed on the shale samples, following the same characterization methodology as for the tight gas samples (Clarkson et al., 2012a), is discussed.

Table 4.11 – BET, Langmuir, and BJH-ads Specific Surface Area and BJH-ads Pore Volume of the Tight Gas and Shale samples.

Sample	Specific Surface Area (m^2/g) (BET)	Langmuir Specific Surface Area (m^2/g)	Specific Surface Area (m^2/g) (BJH ads)	Pore Volume (cm^3/g) (BJH ads)
S1	5.61	7.87	5.67	0.012
S2	7.38	10.21	6.35	0.012
S3	1.78	2.47	1.86	0.006
S4	6.85	9.47	6.89	0.015
S5	2.47	3.52	2.41	0.006
S6	4.12	5.75	4.37	0.012
S7	5.52	7.79	5.84	0.014
S8	4.62	6.46	4.90	0.012
S9	4.59	8.16	5.28	0.013
S10	6.25	8.75	6.39	0.013
Shale B	10.85	14.08	9.23	0.054
Shale D	10.73	16.39	9.91	0.035
Shale M	0.58	1.04	0.88	0.024
Shale P	14.67	20.37	8.95	0.118
Shale R	13.68	24.98	13.16	0.076

Figure 4.19 shows the raw isotherm data for the shales B, D, M, P, and R with the hysteresis showing mesopores in the structure (the isotherms of the tight gas samples were

presented in Clarkson et al., 2012a). The absence of microporosity is apparent since no type I isotherm is observed at low relative pressure for any of the shale samples.

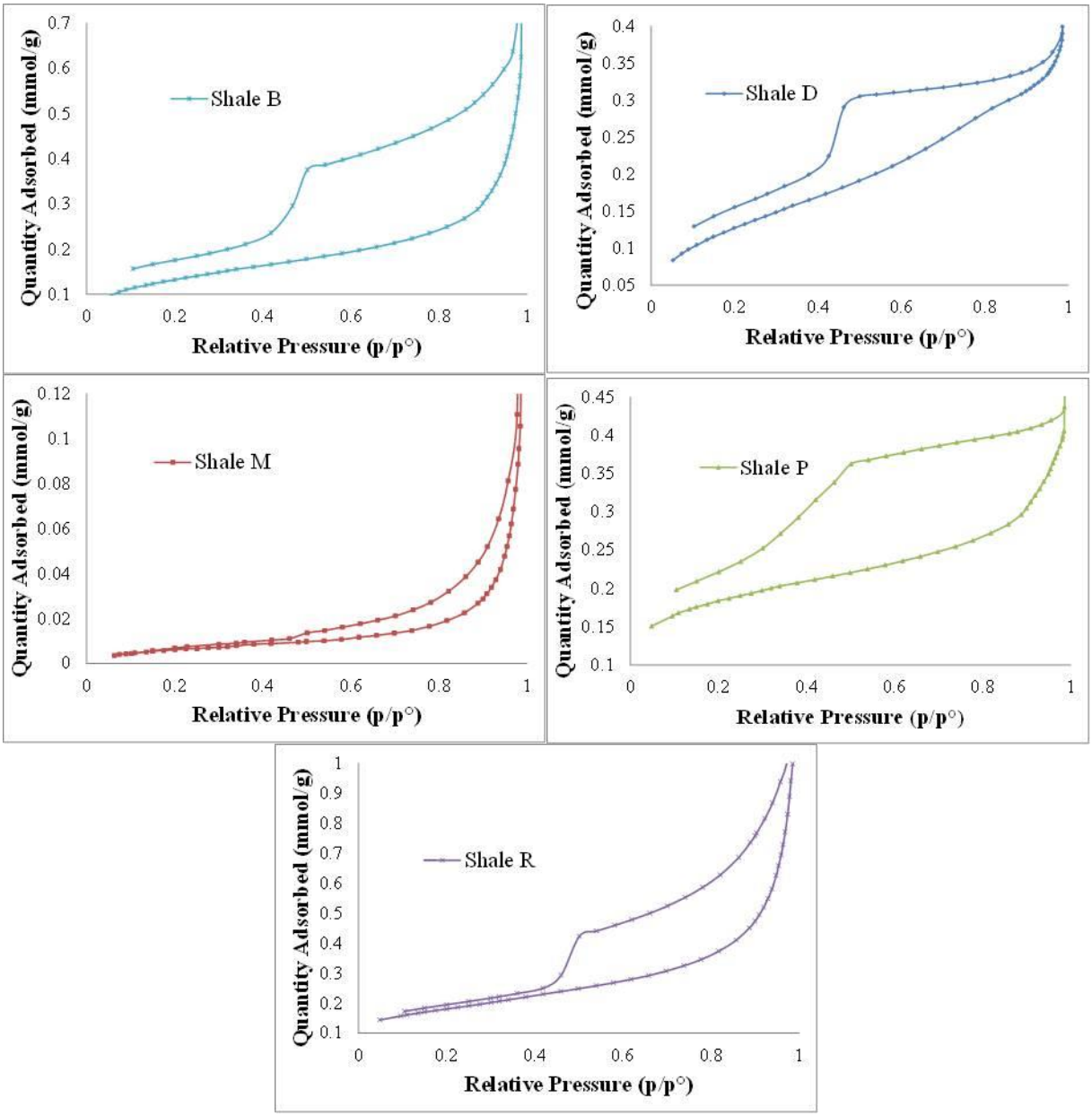

Figure 4.19 Low pressure N_2 adsorption isotherm of shales B, D, M, P, and R.

Shale M is most similar to the tight gas samples in terms of pore shape as inferred from isotherm shape. Shale M also has a similar surface area to the tight gas samples. The other shale

samples, while being similar to each other in terms of pore structure, appear different from the tight gas samples.

Pore shape of samples can be determined according to the classification of the physisorption isotherms and the hysteresis loops shape of isotherms (Sing et al., 1985). Table 4.12 shows the pore geometry of the shale samples determined by the isotherm loop shape comparing the raw data to the types of hysteresis loops shapes.

Table 4.12 Pore shape of shale samples from comparison with the hysteresis loops shape.

Sample	Type of Hysteresis Loops	Pore Shape Associated
Shale B	H2	Ink bottle
Shale D	H2	Ink bottle
Shale M	H3	Slit-shaped
Shale P	H2 – H3	Ink bottle and slit-shaped at the same time
Shale R	H2	Ink bottle

Shale samples B, D, and R seem to match the "ink bottle" model associated with the isotherm shape as discussed in section 2.4.1, while sample M is clearly a type H3 associated to slit-shape pores as reported previously (Clarkson et al., 2012a). However, shale sample P is a combination of isotherms type H2 and H3; therefore, the two types of pore geometry (ink bottle and slit-shape) may exist in the sample.

Pore size distributions for Shales B, D, M, P, and R, obtained using BJH Theory and the adsorption branch of the isotherm, are given Figure 4.20. The mesopore range evident from the isotherms is shown. Most shales show an increase while approaching the micropore range (< 2 nm) and a decreasing in the macropore range (>60 nm). Shale R appears to have a peak near 3 nm. Shale M has a relatively small pore volume, which is consistent with the small surface area

reported in Table 4.11. Note that, dV/dw plots were used in this study since dV/dlogw magnifies the y-axis value by a factor of 10, which is not necessary, as only the nano pore sizes are of interest (Clarkson et al., 2012).

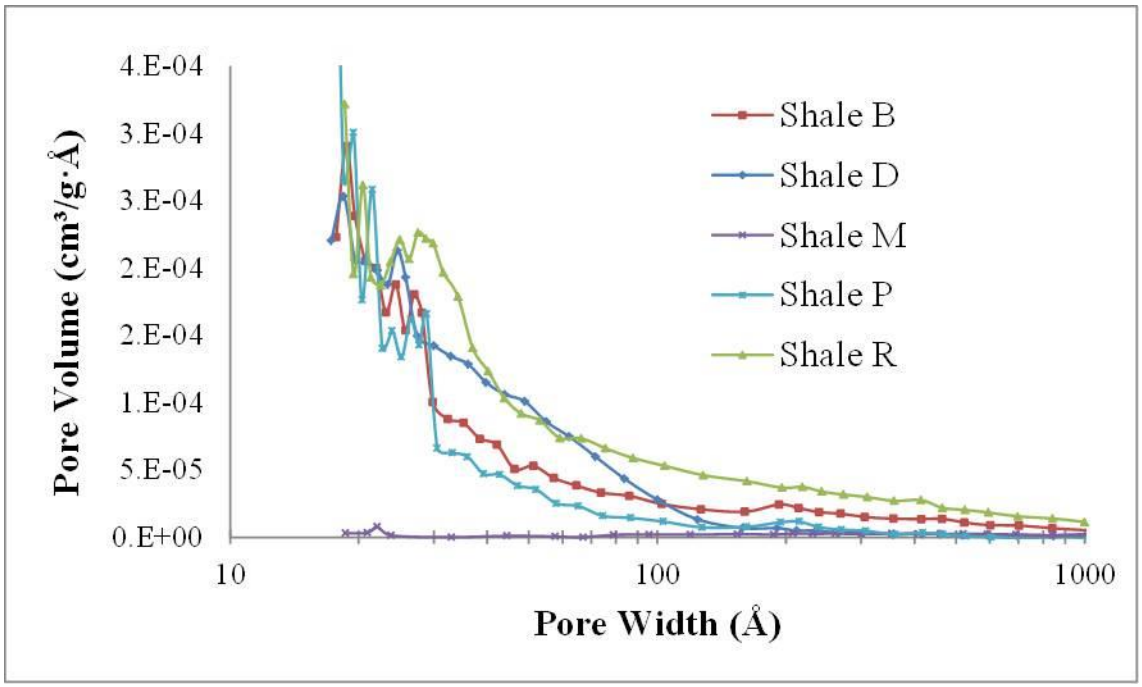

Figure 4.20 Pore size distribution of shales B, D, M, P, and R using the BJH model on the adsorption branch.

Figure 4.21 shows the pore size distribution of the Shales B, D, M, P, and R obtained by from the desorption branch of the isotherm using BJH Theory. These PSDs differ from those obtained from the adsorption branch as there is an apparent peak between 3 and 4 nm for all shales except M and P. However, as discussed in the previous chapter, this peak is associated with an "artifact" of the BJH model (Groen et al., 2003). Shales M and P do not show this false peak, possibly due to partial or total absence "ink bottle" pore shape which is the only difference that these two shale samples have shown compared to the other shale samples.

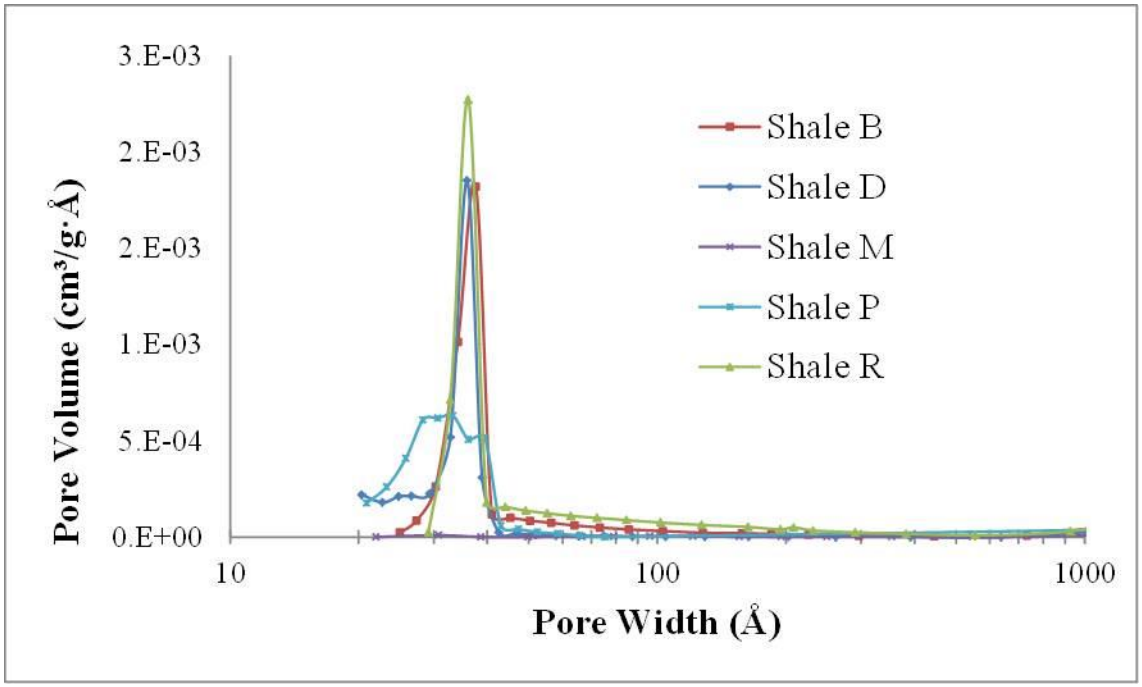

Figure 4.21 Pore size distribution of shales B, D, M, P, and R using the BJH model for the desorption branch.

Figure 4.22 provides the pore size distribution of the Shales B, D, M, P, and R obtained using the DFT "N_2 @ 77 °K on Carbon, Slit Pores" model. Shales D and P appear to have porosity in the lower mesopore range, while shales R and B appear to develop porosity in the larger mesopore range. We note that the PSDs may not be accurate because of the assumption of slit-shaped pores when they appear to be "ink bottle" type from the hysteresis loops. Figure 4.23 shows a comparison between BJH-ads and DFT pore size distribution for shale D, with some differences likely due to the assumption of pore shape used in the models.

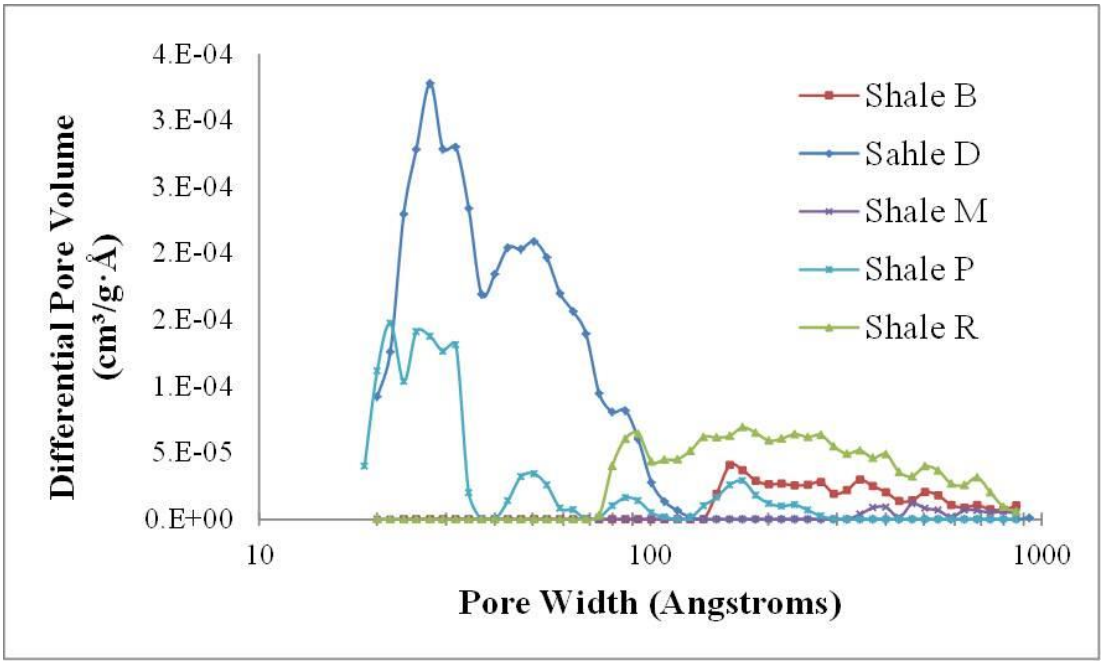

Figure 4.22 Pore size distribution of shales B, D, M, P, and R using DFT model for the adsorption branch.

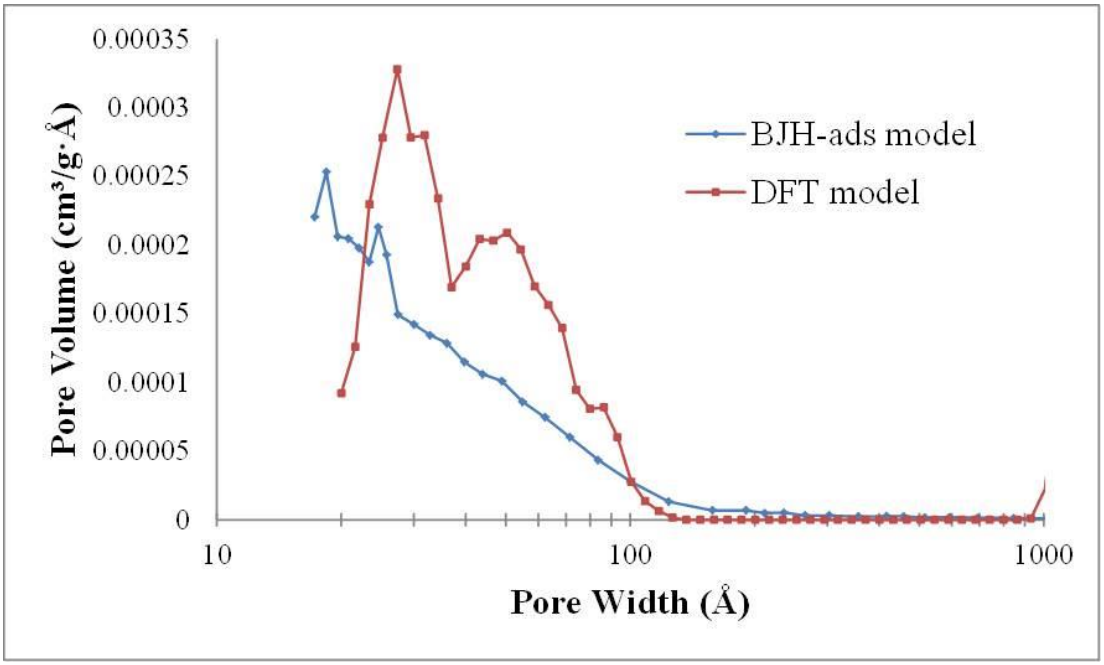

Figure 4.23 Comparison of the pore size distribution of shales D obtained from BJH and DFT model from N_2 adsorption isotherm.

4.4.2.4.2 Low Pressure CO_2 Adsorption

The specific surface area of the shale samples was also obtained by BET, Langmuir, Dubinin-Astakhov, Dubinin-Radushkevich, and DFT models using low pressure CO_2 adsorption (see Table 4.13). The pre-treatment performed in the samples consisted of heating the sample to 60 °C overnight in an Ar atmosphere. Results show that surface area in the micropore range for the samples is about the same as was found in the mesopore range when low pressure N_2 adsorption was performed. All models except Dubinin-Astakhov appear to be in agreement.

Table 4.13 Specific Surface Area of shales B, D, M, P, and R calculated by BET, Langmuir, Dubinin-Astakhov, Dubinin-Radushkevich, and DFT models.

Sample	BET Specific Surface Area (m^2/g)	Langmuir Specific Surface Area (m^2/g)	Dubinin-Astakhov Specific Surface Area (m^2/g)	Dubinin-Radushkevich Specific Surface Area (m^2/g)	DFT Specific Surface Area (m^2/g)
Shale B	16.62	18.81	56.47	16.16	16.00
Shale D	14.56	16.93	90.61	16.45	13.89
Shale H	11.71	13.05	45.86	12.36	12.39
Shale P	7.37	7.64	22.69	14.38	14.84
Shale R	16.55	16.49	102.09	36.13	22.63

Figure 4.24 shows the CO_2 adsorption isotherms for shales B, D, H, and P. Note that the shape of the isotherms is different for each sample. Shale B shows a little knee at low relative pressure (< 0.05 p/p°), then it shows a straight line; shale D shows a straight line from the initial relative pressure; shale H shows a very little knee at relative pressures < 0.05, and shale P is the has the most significant knee on the isotherm at low partial pressures, similar to the type I isotherm (Langmuir) for materials having micropores. Note that, all the plots illustrate an

increase in slope above a relative pressure > 0.02, indicating that samples are adsorbing more CO_2.

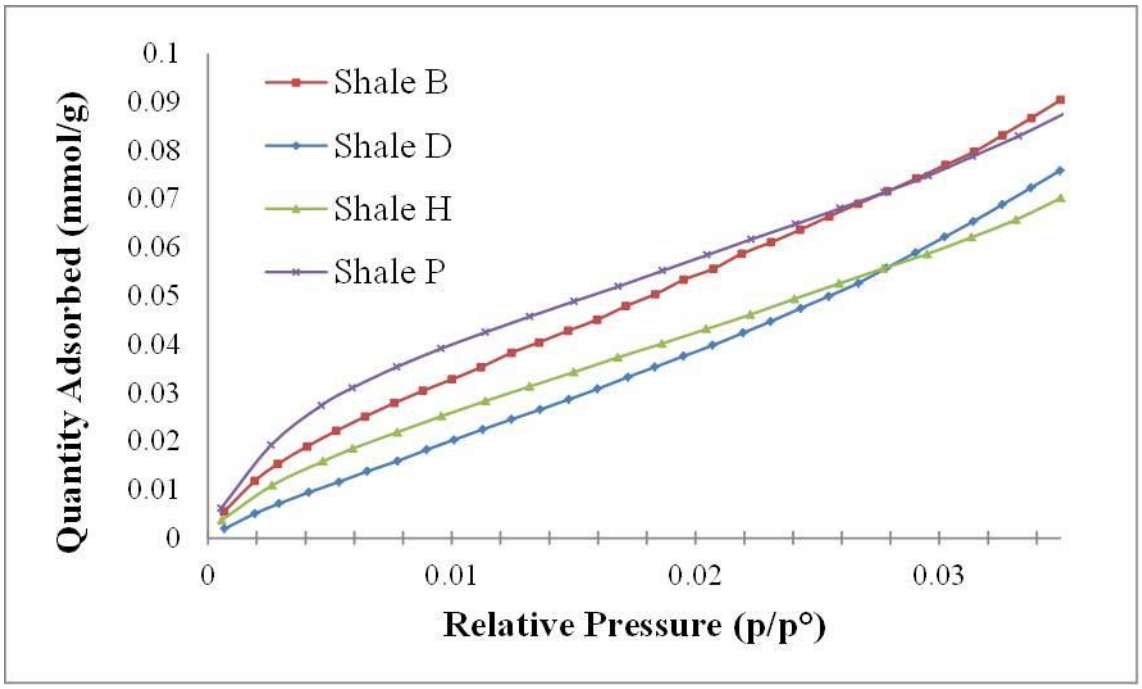

Figure 4.24 Low pressure CO_2 adsorption isotherm of shales B, D, H, and P.

This issue of straight line isotherms has been discussed in the literature previously for CO_2 adsorption on coal (Yi et al., 2009; Ozdemir et al., 2002). The argument is that coal swells due to the presence of CO_2; thus, some micropores that are closed to inert gases, such as Ar, could be accessible to CO_2. If the effect of swelling is large enough in a sample, there could exist two types of CO_2 sorption. The first type of sorption is the CO_2 being dissolved in the coal, which is explained by Henry's law; the second type of sorption of CO_2 is the typical Langmuir effect that take place in open micropores. It is important to highlight that this two types of species can exchange rapidly. As seen in the XPS and AES results explained above, shale samples studied here contain a large amount of carbon in form of kerogen (organic matter). The

presence of straight line CO_2 isotherms for these samples indicates that CO_2 is being dissolved in the kerogen or bitumen of the samples; thus, Henry's law can explain the shape of the isotherms.

Finally, the DFT model was used to obtain information about the pore size distribution of the samples (Figure 4.25). As discussed in the previous chapter (Section 3.3.4.3), not much information was obtained from this plot since random peaks from 5 to 8 Å was observed in all the samples. The plots do not give information for pores larger than 8 Å. It is therefore not possible to compare these results and the results obtained from the BJH model in the previous section. The apparent lack of agreement between N_2- and CO_2-derived pore size distributions may be due to the mechanism of CO_2 sorption just discussed – the apparent dissolution of CO_2 in kerogen (or bitumen) may be leading to a false pore size distribution.

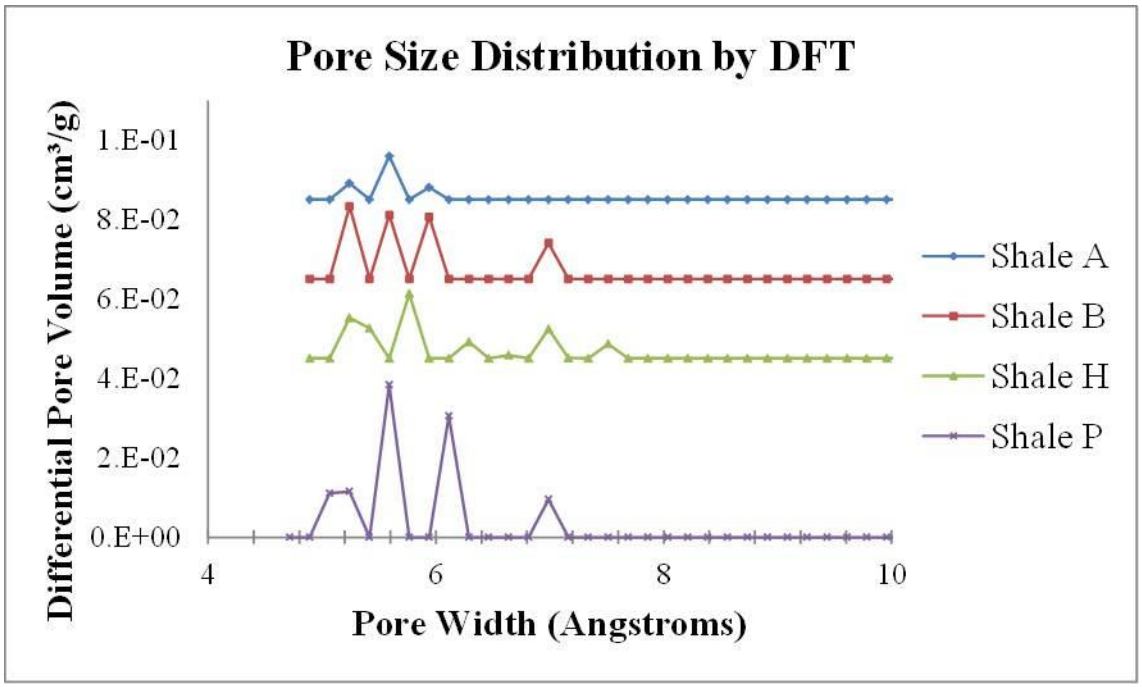

Figure 4.25 Pore size distribution of shales B, D, H, and P using DFT model from CO_2 adsorption isotherm.

4.5 Summary

- Routine characterization techniques were used to establish the principal characteristics of the samples: morphological structure, mineralogical analysis, and TOC content were obtained from SEM, XRD, and Rock-Eval pyrolysis, respectively. These results combined together were used to further validate results obtained with non-routine characterization techniques.
- AES shows that when using optimal experimental conditions (removing charge effect), good results can be obtained. It shows by depth profiling that the Muskwa-Cordova shale sample has a thin layer of carbon (~ 30 nm thick) covering the grains.
- XPS showed that the chemical composition of the samples is similar to those obtained from XRD; even though, these techniques are for surface and bulk analysis, respectively. Carbon species were separated and quantified in organic and inorganic carbon, also giving a good match with the XRD results for dolomite.
- Low pressure N_2 adsorption analysis of tight gas samples revealed a wide pore size distribution from the macro-range to the meso-range and two different models (BJH and DFT) were used to quantify the pore size distributions. The pore shape in the tight gas samples are, as presented elsewhere (Clarkson et al., 2012a), are interpreted to be slit-shaped pores. Most of the shale samples on the other hand appear to have either ink-bottle pores or a mixture of ink-bottle and slit-shaped pores.
- Finally, low pressure CO_2 adsorption analysis performed on the shale samples did not give reliable results because a significant amount of sorption appears to be due to dissolution of CO_2 in organic matter of the samples described by Henry's Law.

Chapter Five: **Summary and Future Work**

5.1 Summary

5.1.1 Ni-containing H-ZSM-5 Catalysts

Ni/H-ZSM-5 zeolite catalysts, used for the hydrocracking of a model compound, toluene, were prepared using two different methods (SS and WI) and with different Ni loadings. The primary goal was to determine how and where the NiO particles (NiO is converted to Ni when exposed to the hydrocracking conditions) are located on the zeolitic support, while a secondary goal was to determine whether SS and WI lead to different Ni characteristics. A range of characterization techniques were used to study these catalysts, including XRD, TPR, DRIFTS, and low pressure gas sorption analysis. The integration of the results obtained from all if these techniques has led to the following main conclusions:

- SEM images indicated that the SS and WI catalysts are very similar morphologically. Once the H-ZSM-5 precursor was synthesized, the mechanical mixing and high temperatures used for calcination do not modify the morphological properties of the support. Also, no agglomerations or new particles were seen on the support after Ni incorporation. The EDS results confirmed the presence of Ni in the catalysts and suggested that the NiO particles were incorporated in a very dispersed way, regardless of the incorporation method used.
- NiO particles are dispersed on the support, since no agglomerates were detected by XRD analysis. However, XRD was able to detect NiO on H-ZSM-5 only at relatively high Ni contents (> 5 wt. %) , based on the crystalline phases of the [1,1,1] and [2,0,0] planes. By using slow XRD experiments and comparing with simulated XRD patterns, we were able to confirm that

NiO particles are present in the catalysts and that they have a crystal domain size of < 8 and < 4 nm for catalysts prepared by SS and WI, respectively.

- The TPR profiles for the SS catalysts showed a characteristic peak for NiO at 380 °C, with a second peak (and possibly more) appearing for Ni contents > 1 wt %. This shows that NiO particles have a multimodal size distribution, while for the WI catalysts, these also showed a multimodal size distribution of the NiO particles, but independent of the Ni content. The small peaks seen at high reduction temperatures may also indicate the presence of NiO particles trapped in sealed pores and/or NiO particles interacting with the zeolite support.
- Results obtained from DRIFTS indicated that the NiO particles that interact with the support are being attached to the Bronsted acid sites, since a progressive reduction in the intensity of the IR signal for these sites is observed as the Ni loading increased. This effect is desirable, since the metal phase and the acid sites are both required to carry out the hydrocracking reaction.
- Low pressure N_2 adsorption analysis showed that the presence of large NiO particles may be the cause of pore blockage of the support, since the surface area decreased as the Ni loading increased, regardless the preparation method employed, as verified by two data analysis methods (BJH and DFT).
- Low pressure CO_2 adsorption analysis showed that the specific surface area of the Ni/zeolite catalysts decreases when the Ni content increased. This effect was more prominent in the catalysts prepared by WI than by SS. This is an indication that NiO is located primarily in the micropore than the meso- macro-pore structure when using WI rather than SS.

By integrating all of these results, the main conclusion is that NiO particles are located on the support in a multimodal size distribution, with the smallest particles interacting with the

Bronsted acid sites of the zeolite. Large NiO particles having crystal domains < 8 nm in size may be blocking some of the pores of the support, while smaller NiO particles are found to block the micropores in the WI catalysts more than in the SS catalysts. However, the efficiency of both of these catalysts towards the hydrocracking of toluene is still high, likely due to the fact that the metal phase is sufficiently close to the acidic zeolite sites for both the SS and WI materials.

5.1.2 Naturally occurring Tight Gas/Shale Core Plugs

For the naturally occurring tight gas/shale samples, non-routine characterization techniques, some of which were also used in the Ni/zeolite study, were used in order to determine their chemical composition, organic matter content, and nanoporous structure. The characterization techniques used were XPS, AES, and low pressure gas sorption.

- AES was performed for the tight gas samples; however, too much charging occurred for these samples. The charge effect generated a very large peak in the range of energy where most of the elements relevant to the tight gas samples should appear in the AES spectrum. However, for the shale Sample P, AES did produce a reasonable spectrum. Depth profiling of Sample P showed that the carbon content varies as thin layers (3 nm) were removed from the surface. A carbon film, ca. 30 nm in thickness, was determined to be covering the grains.
- For the tight gas samples, the elemental composition obtained with XPS showed a good match compared with the mineralogical composition obtained from XRD. This match confirms that XPS is a useful technique for chemical composition characterization of these types of samples. Additionally, both organic and inorganic oxygen were determined by XPS, with the theoretical values for organic oxygen giving a good match to those measured experimentally.

XPS analysis of the shale samples also showed a good match with the mineralogical composition obtained with XRD.

- The carbon content was also determined by XPS, as this technique can separate organic carbon from inorganic carbon. The carbon content varied among the tight gas samples as well as in the shale samples. However, the values of organic carbon obtained from XPS were always higher than the ones obtained from Rock-Eval pyrolysis, showing that the majority of the carbon content may be at the surface of the sample (pore walls or inter-granular). Thus, most of the organic carbon is present on the surface of the sample, as is also shown by AES.
- From low pressure N_2 adsorption, it was demonstrated that tight gas samples have an average specific surface area ~ 5 m^2/g while shale samples have higher values. Only shale sample M has a very low specific surface area (< 1 m^2/g). From the shape of the hysteresis loop, tight gas shale samples are inferred to have mainly slit-shape pores; some may have "ink-bottle" shapes as well. Pore size distributions obtained from BJH and DFT models are similar, showing that the majority of the pores are in the lower meso-range (< 20 nm), rather than in the high meso- (> 40 nm) and macro-range.
- Low pressure CO_2 adsorption demonstrated that shale samples have a higher specific surface area in the micropore range than in the mesopore range, as demonstrated by BET, Langmuir, and DFT isotherm analysis. The linear shape of the isotherm indicates CO_2 maybe dissolving within the organic matter of the samples.

5.2 Future Work

5.2.1 Ni-containing H-ZSM-5 Catalysts

There are many possible extensions of this work, as suggested below:

- Other Ni salt precursors could be studied in order to determine whether the nature of the Ni salt to NiO decomposition process may alter the characteristics of the Ni nanoparticles. Additionally, other incorporation methods could generate different dispersions of NiO in the H-ZSM-5.
- Other characteristics of the Ni present in the catalysts could be determined by using other characterization techniques, such as H_2 chemisorption and inductively couple plasma spectroscopy (ICP) to determine the number of active sites (dispersion) of the metal phase and a better quantification of the Ni present in the catalysts, respectively. With these results in hand, an estimation of how much Ni is participating in the catalytic reaction could be obtained.
- TEM studies should be carried out to determine precisely where the Ni nanoparticles are located in the pores of both of the Ni-loaded zeolite catalysts.

5.2.2 Naturally occurring Tight Gas/Shale Core Plugs

Other studies that could help to further characterize the nanoporous structure of these samples include:

- XPS depth profiling over a smaller area could give information about the carbon on the surface of the shale samples. Additionally, if there is kerogen present in the samples, it may be distinguishable using XPS.
- Depth profiling with SEM imaging should be carried out at the same time in order to determine what types of minerals/components are present in the area examined. Gradually increasing the magnification of analysis would generate a better visualization of specific structures.

- TEM imaging could be performed to establish the sample microstructure and to determine what type of minerals/organic matter/structure are present.
- The gas sorption apparatus software should be improved in order to determine the pore size distribution of the tight gas and shale samples, since the model employed (DFT) for the CO_2 isotherms did not provide the needed information about the micropore structure.

References

Alvarez-Ayuso E., Garcia-Sanchez A., Querol X. (2003) "*Purification of metal electroplating waste waters using zeolites*" Water Res. 37 4855.

Arcoya A., Seoane X. L. (1990) "*Effect of protonation on hydroconversion of n-dodecane over Ni/ZSM-5 catalysts*" React. Kinet. Catal. Lett. 41 181.

Badrinarayanan S., Hegde R. I., Balaskrishnan I., Kulkarni S. B., Ratnasamy P. (1981) "*XPS study of nickel in NiHZSM5 catalysts*" J. Catal. 71 439.

Balkrishnan, I., Rao B. S., Hegde S. G., Kotasthane A. N., Kulkarni S. B., Ratnaswamy P. (1982) *"Catalytic activity and selectivity in the conversion of methanol to light olefins" J. Mol. Catal. 17 261.*

Bustin, R.M., Bustin, A.M.M., Cui, X., Ross, D.J.K., Murthy Pathi, V.S. (2008) "*Impact of Shale Properties on Pore Structure and Storage Characteristics*" SPE paper 119892.

Cerenasa Research (2013) "*Market Study: Propylene*". Retrieved from http://www.ceresana.com/en/market-studies/chemicals/propylene/ (Apr 2013).

Chang F. W., Kuo M. S., Tsay M. T., Hsieh M. C. (2003) *"Hydrogenation of CO_2 over nickel catalysts on rice husk ash-alumina prepared by incipient wetness impregnation"* Appl. Catal., A 247 309.

Chen N. Y., Garwood W. E., Dwyer F. G. (1989) "*Shape Selective Catalysis in Industrial Applications*". Marcel Dekker, NewYork, Basel, 203.

Clarkson C. R., Bustin R. M. (1999) "*The effect of pore structure and gas pressure upon the transport properties of coal: a laboratory and modeling study. 1. Isotherms and pore volume distributions*" Fuel 78 1333.

Clarkson C. R., Wood J. M., Burgis S. E., Aquino S. D., Freeman M. (2012a) "*Nanopore-Structure Analysis and Permeability Predictions for a Tight Gas Siltstone Reservoir by Use of Low-Pressure Adsorption and Mercury-Intrusion Techniques*" SPE Reserv. Eval. Eng. 15 648.

Clarkson C. R., Freeman M., He L., Agamalian M., Melnichenko Y. B., Mastalerz M., Bustin R. M., Radliński A. P., Blach T. P. (2012b) "*Characterization of tight gas reservoir pore structure using USANS/SANS and gas adsorption analysis*" Fuel 95 371.

Clarkson C. R., Solano N., Bustin R. M., Bustin A. M. M., Chalmers G. R. L., He L., Melnichenko Y. B., Radliński A. P., Blach T. P. (2013) "*Pore structure characterization of North American shale gas reservoirs using USANS/SANS, gas adsorption, and mercury intrusion*" Fuel 103 606.

Comisky, J.T., Newsham, K.E., Rushing, J.A., and Blasingame, T.A. (2007) "*A Comparative Study of Capillary-Pressure-Based Empirical Models for Estimating Absolute Permeability in Tight Gas Sands*" SPE paper 110050.

Cullity B. D., Stock S. R., (2001) *"Elements of X-ray Diffraction"* 3rd Ed. Upper Saddle River, N.Y.: Prentice Hall c2001.

Curtis M. E., Ambrose R.J., Sondergeld C. H., Rai S. C. (2011). *"Transmission and Scanning Electron Microscopy Investigation of Pore Connectivity of Gas Shales on the Nanoscale "* North American Unconventional Gas Conference and Exhibition, 14-16 June 2011, The Woodlands, Texas, USA. SPE: 144391.

De Jonge H., Mittelmeijer-Hazeleger M. C. (1996) *"Adsorption of CO_2 and N_2 on Soil Organic Matter: Nature of Porosity, Surface Area, and Diffusion Mechanisms"* Environ. Sci. Technol. 30 408.

Do, D. D, and Do, H. D. (2003) *"Pore Characterization of Carbonaceous Materials by DFT and GCMC Simulations: A Review"* Adsorpt. Sci. Technol. 21 389

Dwyer F. G. (1981) in Moser W. R. (Ed.), "*Catalysis of Organic Reactions*" Marcel Dekker, New York, Basel, 39.

Firoozi M., Baghalha M., Asadi M. (2009) *"The effect of micro and nano particle sizes of H-ZSM-5 on the selectivity of MTP reaction"* Catal. Commun. 10 1582.

Freel J., Galwey A. K. (1968) "*Hydrocarbon cracking reactions on nickel*" J. Catal. 10 277.

Garrido J., Linares-Solano, A., Martin-Martinez, J. M., Molina-Sabio, M., Rodriguez-Reinoso, F., Torregrosa, R. (1987) *"Use of nitrogen vs. carbon dioxide in the characterization of activated carbons"* Langmuir 3 76.

Gregg S. J., Sing K. S. W. (1982) "*Adsorption, surface area, and porosity*" 2nd ed. New York: Academic Press.

Giannetto G., Montes A., and Rodriguez G. (2000). "*Zeolitas*". 2nd Edition, Caracas, Venezuela. 151-154.

Gonzalez H., Ramirez J., Zarate R. , Cortez T. (2001) *"Hydroconversion of a Model Mixture and Fluid Catalytic Cracking Gasoline for Octane Enhancement. Main Reaction Pathways over Monofunctional HZSM5(x)-Alumina Catalysts"* Ind. Eng. Chem. Res. 40 1103.

Gonzalez H., Ramirez J., Gutierrez-Alejandre A., Castillo P., Cortez T., Zarate R. (2004) *"Selective hydroconversion of a model mixture and hydrotreated FCC gasoline for octane enhancement"* Catal. Today 98 181.

Hernandez E. (2012) *" Ni Based Catalyst for Hydrocracking of Light Aromatics and Middle Distillates to Light Paraffins*" MEng thesis. University of Calgary.

Hoang D. L., Berndt H., Miessner H., Schreier E., Vijlter J. (1994) "*Nickel modified H-ZSM-5 catalysts*" Appl. Catal. A 114 295.

Holditch S.A. (2003) "*The Increasing Role of Unconventional Reservoirs in the Future of the Oil and Gas Business*" SPE President Publications.

Holditch S.A. (2006) "*Tight Gas Sands*" SPE Paper 103356. Distinguished Author Series, J Pet Tech.

Holditch S. A. (2010) *"Global Unconventional Gas—It Is There, But Is It Profitable?"* J.Petrol. Technol. 62 42.

Hurst N. W., Gentry S. J., Jones A. (1982) *"Temperature Programmed Reduction"* Catal. Rev. Sci. Eng. 24 233.

Janssen A. H., Koster A. J., de Jong K. P. (2002) *"On the Shape of the Mesopores in Zeolite Y: A Three-Dimensional Transmission Electron Microscopy Study Combined with Texture Analysis"* J. Phys. Chem. B 106 11905.

Karge H. G., Zhang Y., Beyer H. K. (1992) *"Preparation of bifunctional catalysts by solid-state ion exchange in zeolites"* Catal. Lett. 12 147.

Kelemen S. R., Afeworki M., Gorbaty M. L., Sansone M., Kwiatek P. J., Walters C. C., Freund H., Siskin M. (2007) *"Direct Characterization of Kerogen by X-ray and Solid-State ^{13}C Nuclear Magnetic Resonance Methods"* Energ. Fuel. 21 1548.

Kentgens A. P. M., Scholle K. F. M. G. J., Veeman W. S. (1983) *"Effect of hydration on the local symmetry around aluminum in ZSM-5 zeolites studied by aluminum-27 nuclear magnetic resonance"* J. Phys. Chem. 87 4357.

Klingmann R., Josl J., TraaY. , Gläser R., Weitkamp J. (2005) "*Hydrogenative regeneration of a Pt/La-Y zeolite catalyst deactivated in the isobutane/n-butene alkylation*" Appl. Catal. A: Gen. 281 215.

Kubelkova L., Novakova J., Jaeger N. J., Schulz-Ekloff G. (1993) "Characterization of nickel species at Ni/γ-Al203 and Ni/faujasite catalysts by carbon monoxide adsorption" Appl. Catal. A 95 101.

Kumar N., Byggningsbacka R., Lindfors L-E. (1997) *"Aromatization ofn-butane over Ni-ZSM-5 and Cu-ZSM-5 zeolite catalysts prepared by using Ni and Cu impregnated silica, fiber"* React. Kinet. Catal. Lett. 61 297.

Lamond T. G., Marsh H. (1964) *"The surface properties of carbon-II the effect of capillary condensation at low relative pressures upon the determination of surface area"* Carbon 1 281.

Le Page J. F., Cosyns J., Courty P., Freund E., Franck J. P., Jacquin Y., Jugun B., Marcilly C., Martino G., Miguel J., Montarnal R., Sugier A., Van Landeghan H. (1967) *"Catalyse de contact: Conception, preparation et mise en oeuvre des catalyseurs industriels"* Ed. Technip, Paris p. 365

Lee D., Cho S., Kim G-J., Lee I-K. (2007) "*Efficient and Selective Hydrogenation of Carboxylic Acid Catalyzed by Ni or Pd on ZSM-5"* J. Ind. Eng. Chem. 13 1067.

Lugstein A., Jentys A., Vinek H. (1997) *"n -Heptane cracking on H- and Ni-containing zeolites"* J. Chem. Soc. Faraday Trans. 93 1837.

Lugstein A., Jentys A., Vinek H. (1999) *"Hydroisomerization and cracking of n-octane and C_8 isomers on Ni-containing zeolites"* App. Catal. 176 119.

Maggs F. A. P. (1952) *"Anomalous Adsorption of Nitrogen at 90° K"* Nature 196 793.

Mahmoud M. H. (2006) *"Surface Modification of Silica Gel for Selective Extraction of Metal Ions",* Encyclopaedia of Chromatography, 2nd Ed. Boynton Beach, FL.: Marcel Dekker.

Maia A. J., Louis B., Lam Y. L., Pereira M. M. (2010) *"Ni-ZSM-5 catalysts: Detailed characterization of metal sites for proper catalyst design"* J. Catal. 269 103.

Malet P., Caballero A. (1988) *"The selection of experimental conditions in temperature-programmed reduction experiments"* J. Chem. Soc., Faraday Trans. 84 2369.

Malherbe R. R., Wendelbo R. (2003) *"Study of Fourier transform infrared-temperature-programmed desorption of benzene, toluene and ethylbenzene from H-ZSM-5 and H-Beta zeolites"* Thermochim. Acta 400 165.

Masalska A. (2005) *"Ni-loaded catalyst containing ZSM-5 zeolite for toluene hydrogenation"* Appl. Catal. A, 294 260.

Maunier F. C. (2010) *"The design and testing of kinetically-appropriate operando spectroscopic cells for investigating heterogeneous catalytic reactions"* Chem. Soc. Rev. 39 4602.

McCoy M., Reisch M., Tullo A. H. (2006) *"Facts & Figures Of The Chemical Industry"* Chem. Eng. News 84 35.

McCusker L. B., Von Dreele R. B., Cox D. E., Louer D., Scardie P. (1999) *"Rietveld Refinement Guidelines"* J. Appl. Cryst. 32 36.

Mediavilla M., Morales H, Melo L., Sifontes A. B., Albornoz A., Llanos A., Moronta D., Solano R., Brito J. L. (2010) *"Microwave-assisted polyol synthesis of Pt/H-ZSM5 catalysts"* Micropor. Mesopor. Mat. 131 342.

Melo L., Díaz Y., Mediavilla M., Llanos A., Albornoz A., Brito J. L. (2008) *"Preparation and characterization of bifunctional catalysts of the Pd, Pt/H[Ga]MFI types"* Catal. Today 133–135 99.

Molero H., Galarraga C., Feng F., Hernández E., Birss V., Pereira P. (2009) *"High Performance Ni Based Catalyst for Toluene Hydrocracking"* Catal. Lett. 132 402.

Molero H., Hernandez E., Vitale G., **Aquino S.,** Birss V. I., Pereira-Almao P. (2012) "*Effect of Ni loading in a high performance toluene hydrocracking catalyst*", Appl. Catal A (Minor Rev. Manuscript ID: APCATA-D-12-00266).

Molina R., Centeno M. A., Poncelet G. (1999) *"α-Alumina-Supported Nickel Catalysts Prepared with Nickel Acetylacetonate. 1. Adsorption in the Liquid Phase"* J. Phys. Chem. B 103 6036.

Naber J. E., de Jong K. P., Stork W. H. J., Kuipers H. P. C. E., Post M. F. M., in: Weitkamp J., Karge H. G., Pfeifer H., Hölderich W. (1994) (Eds.), *"Zeolites and Related Microporous Materials: State of the Art"* (1994), Studies in Surface Science and Catalysis, Elsevier, Amsterdam, 84 2197, Part C.

Niemantsverdriet J. W. (2000). "*Spectroscopy in Catalysis: An Introduction*" Wiley-VCH, Weinheim, Germany. 9-12.

Okal J., Zawadzki M., (2009) *"Catalytic combustion of butane on Ru/γ-Al_2O_3 catalysts"* Appl. Catal. B: Environ. 89 22.

Ozdemir E., Schroeder K., Morsi B. I. (2002) *"Adsorption Capacity of Carbon Dioxide on Argonne Premium Coals"* Fuel Chemistry Division Preprints 47 10.

Paal Z. (1988) "*Hydrogen Effects in Catalysis"* Dekker, New York, 1988, 449.

Poncelet G., Centeno M. A., Molina R. (2005) *"Characterization of reduced α-alumina-supported nickel catalysts by spectroscopic and chemisorption measurements"* Appl. Catal. A-Gen 288 232.

Rabl S., Haas A., Santi D., Flego C., Ferrari M., Calemma V., Weitkamp J. (2011) *"Ring opening of cis-decalin on bifunctional Ir/- and Pt/La-X zeolite catalysts"* Appl. Catal. A Gen. 400 131.

Raichle A., Ramin M., Singer D., Hunger M., Traa Y., Weitkamp J. (2001) *"Influence of the aluminum content of zeolite H-ZSM-5 on the conversion of methylcyclohexane into a high-quality synthetic steamcracker feedstock"* Catal. Commun. 2 69.

Ramnani S. P., Sabharwal S., Kumar J. V., Prasad Reddy K. H., Rama Rao K. S., Sai Prasad P. S. (2008) *"Advantage of radiolysis over impregnation method for the synthesis of SiO_2 supported nano-Ag catalyst for direct decomposition of N_2O"* Catal. Commun. 9 756.

Ravikovitch P. I., Neimark A. V. (2001) *"Characterization of nanoporous materials from adsorption and desorption isotherms"* Colloid Surface A 187–188 11.

Reddy J. K., Koyama K. M. T., Miyaji A., Baba T. (2012) *"Effect of morphology and particle size of ZSM-5 on catalytic performance for ethylene conversion and heptane cracking"* J. Catal. 289 53.

Ren S., Qiu J., Wang C., Xu B., Fan Y., Chen Y. (2007) *"Influence of Nickel Salt Precursors on the Hydrogenation Activity of Ni/γ-Al2O3 Catalyst"* Chin. J. Catal. 28 651.

Rietveld H. M. (1967) "*Line profiles of neutron powder-diffraction peaks for structure refinement*" Acta Cryst 22: 151-2

Rode C. V., Arai M., Shirai M., Nishiyama Y. (1997) *"Gas-phase hydrogenation of nitriles by nickel on various supports"* Appl. Catal., A 148 405.

Rodriguez-Reinoso, F., Lopez-Gonzalez, J. D., Berenguer, C. (1982) *"Activated carbons from almond shells—I: Preparation and characterization by nitrogen adsorption"* Carbon 20 513.

Rogner H. H. (1997) *"An Assessment of World Hydrocarbon Resources"* Annu. Rev. Energy Environ 22 262.

Ruchenstein E., Pulvermacher B. (1973) *"Growth kinetics and the size distributions of supported metal crystallites"* J. Catal. 29 224.

Saadi A., Merabti R., Rassoul Z., Bettahar M. M. (2006) *"Benzaldehyde hydrogenation over supported nickel catalysts"* J. Mol. Catal. A: Chem. 253 79

Satyanarayana C. V. V., Chakrabarty D. K. (1990) *"Transformation of C8 aromatics on platinum, palladium and nickel supported on ZSM-5"* Appl.Catal. 66 1.

Sauvage E., Germain A., Figueras F. (1995) Book of Abstract, Europacat II, 794.

Scherzer J. (1991) *"Designing FCC catalysts with high-silica Y zeolites"* Appl. Catal. 75 1.

Selvin R., Hsu H. L., Her T. M. (2008) *"Acylation of anisole with acetic anhydride using ZSM-5 catalysts: Effect of ZSM-5 particle size in the nanoscale range"* Catal. Commun. 10 169.

Sie S. T. (1997) in: G. Ertl G., H. Kno¨zinger H., J. Weitkamp J. (Eds.) "*Handbook of Heterogeneous Catalysis*" Wiley–VCH, Weinheim, 4 1998.

Sing K. S. W., Everett D. H., Haul R. A. W., Moscou L., Pierotti R. A., Rouquerol J., Siemieniewska T. (1985) *"Reporting physisorption data for gas/solid systems with special reference to the determination of surface area and porosity"* Pure Appl. Chem. 57 (4) 603.

Sondergeld, C. H., Ambrose, R. J., Rai, C. S., and Moncrieff, J. (2010a) "*Micro-Structural Studies of Gas Shales*" SPE paper 131771.

Sondergeld, C. H., Newsham, K. E., Comisky, J. T., Rice, M. C., and Rai, C. S. (2010b) "*Petrophysical Considerations in Evaluating and Producing Shale Gas Reservoirs*" SPE paper 131768.

Tanaka K., Nagasawa M., Kasuga Y., Sakamura H., Takuma Y., Iwatani K. (1999) *"Highly selective hydrogenation of 2-chloro-5-cyanopyridine with an improved sponge nickel catalyst"* Tetrahedron Lett., 40 5885.

Tao D., Wei F. (2004) *"New procedure towards size-homogeneous and well-dispersed nickel oxide nanoparticles of 30 nm"* Mater. Lett. 58 3226

Tascon J. (2012) *"Novel Carbon Adsorbents"* Elsevier, 1st Ed. Oxford, UK, 38.

Van Koningsveld H., Jansen J. C., Van Bekkum H. (1990) *"The monoclinic framework structure of zeolite H-ZSM-5. Comparison with the orthorhombic framework of as-synthesized ZSM-5"* Zeolites 10 235.

Vedrine J. C., AurouqA., Dejaifve P., Ducarme V., Hoseer H., Zhou S. (1982) *"Catalytic and physical properties of phosphorus-modified ZSM-5 zeolite"* J. Catal. 73 147.

Verna H. R. (2007). "*Atomic and Nuclear Analytical Methods*". Springer Berlin, New York, USA. 213-218.

Vitale G., Molero H., Hernández E., Aquino S., Birss V., Pereira-Almao P. (2013) *"One-pot preparation and characterization of bifunctional Ni-containing ZSM-5 catalysts*" Appl. Catal. A-Gen 452 75.

Vij D. R. (2006). "*Handbook of Applied Solid State Spectroscopy*". Springer Science, New York, USA. 451-458.

Vosmericov A. V., Zaikovskii V. I., Korobitsyna L. L., Echevskii G. V., Kozlv V. V. Barbashin Ya. E., Zhuravkov S. P. (2009) *"Nonoxidative conversion of methane into aromatic hydrocarbons on Ni-Mo/ZSM-5 catalysts"* Kinet. Catal. 50 725.

Webb P. A., Orr C. (1997). *"Analytical Methods in Fine Particle Technology"* Micromeritics Instruments Co. Norcross, GA, USA. 53-93.

Weitkamp J., Jacobs P. A., Martens J. A. (1983) *"Isomerization and hydrocracking of C_9 through C_{16} n-alkanes on Pt/HZSM-5 zeolite"* Appl. Catal. 8 123.

Weitkamp J., Jacobs P. A., Ernst S. (1984) *"Shape Selective Isomerization and Hydrocracking of Naphthenes Over Pt/Hzsm-5 Zeolite"* Stud. Surf. Sci. Catal. 18 279.

Weitkamp J., Maixner S. (1987) *"Isobutane/butene alkylation on a LaNaY zeolite. Characterization of carbonaceous deposits by CP/MAS ^{13}C n.m.r. spectroscopy"* Zeolites 7 6.

Weitkamp J, Ernst A, Bock T, Kromminga T, Kiss A, Kleinschmit P (1996), *"Modified molecular sieves by means of solid ion exchange"* US Patent # 5,529,964.

Weitkamp J. (2000) *"Zeolites and catalysis"* Solid State Ionics 131 175.

Wichterlova B., Beran S., Kubelkova L., Novakova J., Smieskova A., Sebik R., in Karge H. G. and Weitkamp J. (1989) *"Zeolites as Catalysts, Sorbents and Detergent Builders"* (Studies in Surface Science and Catalysis, Vol. 46). Elsevier, Amsterdam, 347.

Williams D., and Barry C. (2009). "*Transmission Electron Microscopy: A Textbook for Materials Science*". Springer Science, New York, USA. 3-9.

Xiao J., Wei J. (1992) *"Diffusion mechanism of hydrocarbons in zeolites—II. Analysis of experimental observations"* J. Chem. Eng. Sci. 47 1143

Yi J., Yücel Akkutlu I., Özgen Karacan C., Clarkson C.R. (2009) *"Gas sorption and transport in coals: A poroelastic medium approach"* Int. J. Coal Geol. 77 137.

Yuan H-X., Xia Q-H., Zhan H-J. Lu Z-H., Su K-X. (2006) *"Catalytic oxidation of cyclohexane to cyclohexanone and cyclohexanol by oxygen in a solvent-free system over metal-containing ZSM-5 catalysts"* Appl. Catal. A, 304 178.

Zaera F., Gleason N. R., Klingenberg B., Ali A. H. (1999) *"Partial oxidation of hydrocarbons on nickel: from surface science mechanistic studies to catalysis"* J. Mol. Catal. A: Chem. 146 13.